REPORT DOCUMENTATION PAGE	*Form Approved* **OMB No. 0704-0188**

Public reporting burden for this collection of information is estimated to average 1 hour per response, including the time for reviewing instructions, searching data sources, gathering and maintaining the data needed, and completing and reviewing the collection of information. Send comments regarding this burden estimate or any other aspect of this collection of information, including suggestions for reducing this burden to Washington Headquarters Service, Directorate for Information Operations and Reports, 1215 Jefferson Davis Highway, Suite 1204, Arlington, VA 22202-4302, and to the Office of Management and Budget, Paperwork Reduction Project (0704-0188) Washington, DC 20503.
PLEASE DO NOT RETURN YOUR FORM TO THE ABOVE ADDRESS.

1. REPORT DATE *(DD-MM-YYYY)* 15-05-2015	**2. REPORT TYPE** Final Report	**3. DATES COVERED** *(From - To)* July 2011 - Sept 2014

4. TITLE AND SUBTITLE Cyber Enabled Direct Digital Manufacturing	**5a. CONTRACT NUMBER** N00014-11-1-0668 **5b. GRANT NUMBER** 71K70-FDP2012 **5c. PROGRAM ELEMENT NUMBER**
6. AUTHOR(S) Abdalla R. Nassar Edward W. Reutzel	**5d. PROJECT NUMBER** ARL-18848 **5e. TASK NUMBER** 01 **5f. WORK UNIT NUMBER**
7. PERFORMING ORGANIZATION NAME(S) AND ADDRESS(ES) The Pennsylvania State University Applied Research Labotatory Office of Sponsored Programs 110 Technology Center Building University Park, PA 16802-7000	**8. PERFORMING ORGANIZATION REPORT NUMBER** n/a
9. SPONSORING/MONITORING AGENCY NAME(S) AND ADDRESS(ES) Office of Naval Research 875 North Randolph Street Arlington, VA 22203-1995	**10. SPONSOR/MONITOR'S ACRONYM(S)** ONR **11. SPONSORING/MONITORING AGENCY REPORT NUMBER** n/a

12. DISTRIBUTION AVAILABILITY STATEMENT
Distribution Statement A - Approved for Public Release

13. SUPPLEMENTARY NOTES

14. ABSTRACT
Developments related to interfacing, sensing, and control of cyber-physical systems that occurred under the Office of Naval Research "Cyber Enabled Direct Digital Manufacturing" program, award N00014-11-1-0668 are discussed. Achievements include the development of a digital thread concept for AM. This concept advanced efforts towards a universal schema for communicating data relevant to AM processes. Taking advantage of the developed schema, direct interfacing of build-plan with finite element simulations was enabled. Additionally, sensing strategies were demonstrated, including optical emission spectroscopy for defect detection, and powder flow monitoring for flow anomaly detection. Real-time control of build plan was also demonstrated and found to significantly impact microstructure and mechanical properties of the deposited Ti-6Al-4V components. A final notable achievement is the invention of a novel method for deposition of directed-energy-deposited high-overhanging structures.

15. SUBJECT TERMS
additive manufacturing, directed energy deposition, sensing, control, open protocol

16. SECURITY CLASSIFICATION OF:			**17. LIMITATION OF ABSTRACT**	**18. NUMBER OF PAGES**	**19a. NAME OF RESPONSIBLE PERSON**
a. REPORT	**b. ABSTRACT**	**c. THIS PAGE**	SAR	113	Edward W. Reutzel
U	U	U			**19b. TELEPONE NUMBER** *(Include area code)* 814-863-9891

Standard Form 298 (Rev. 8-98)
Prescribed by ANSI-Std Z39-18

20150710088

Applied Research Laboratory
Pennsylvania State University

Final Report:

Cyber Enabled
Direct Digital Manufacturing

Submitted to:

Office of Naval Research

for
Award No. N00014-11-1-0668

Authors:
Abdalla R. Nassar
Edward W. Reutzel

ARL Letter Report
15 May 2015

REPORT DOCUMENTATION PAGE

Form Approved
OMB No. 0704-0188

Public reporting burden for this collection of information is estimated to average 1 hour per response, including the time for reviewing instructions, searching data sources, gathering and maintaining the data needed, and completing and reviewing the collection of information. Send comments regarding this burden estimate or any other aspect of this collection of information, including suggestions for reducing this burden to Washington Headquarters Service, Directorate for Information Operations and Reports, 1215 Jefferson Davis Highway, Suite 1204, Arlington, VA 22202-4302, and to the Office of Management and Budget, Paperwork Reduction Project (0704-0188) Washington, DC 20503.

PLEASE DO NOT RETURN YOUR FORM TO THE ABOVE ADDRESS.

1. REPORT DATE *(DD-MM-YYYY)* 15-05-2015	**2. REPORT TYPE** Final Report	**3. DATES COVERED** *(From - To)* July 2011 - Sept 2014

4. TITLE AND SUBTITLE Cyber Enabled Direct Digital Manufacturing	**5a. CONTRACT NUMBER** N00014-11-1-0668
	5b. GRANT NUMBER 71K70-FDP2012
	5c. PROGRAM ELEMENT NUMBER
6. AUTHOR(S) Abdalla R. Nassar Edward W. Reutzel	**5d. PROJECT NUMBER** ARL-18848
	5e. TASK NUMBER 01
	5f. WORK UNIT NUMBER
7. PERFORMING ORGANIZATION NAME(S) AND ADDRESS(ES) The Pennsylvania State University Applied Research Labotatory Office of Sponsored Programs 110 Technology Center Building University Park, PA 16802-7000	**8. PERFORMING ORGANIZATION REPORT NUMBER** n/a
9. SPONSORING/MONITORING AGENCY NAME(S) AND ADDRESS(ES) Office of Naval Research 875 North Randolph Street Arlington, VA 22203-1995	**10. SPONSOR/MONITOR'S ACRONYM(S)** ONR
	11. SPONSORING/MONITORING AGENCY REPORT NUMBER n/a

12. DISTRIBUTION AVAILABILITY STATEMENT
Distribution Statement A - Approved for Public Release

13. SUPPLEMENTARY NOTES

14. ABSTRACT

Developments related to interfacing, sensing, and control of cyber-physical systems that occurred under the Office of Naval Research "Cyber Enabled Direct Digital Manufacturing" program, award N00014-11-1-0668 are discussed. Achievements include the development of a digital thread concept for AM. This concept advanced efforts towards a universal schema for communicating data relevant to AM processes. Taking advantage of the developed schema, direct interfacing of build-plan with finite element simulations was enabled. Additionally, sensing strategies were demonstrated, including optical emission spectroscopy for defect detection, and powder flow monitoring for flow anomaly detection. Real-time control of build plan was also demonstrated and found to significantly impact microstructure and mechanical properties of the deposited Ti-6Al-4V components. A final notable achievement is the invention of a novel method for deposition of directed-energy-deposited high-overhanging structures.

15. SUBJECT TERMS
additive manufacturing, directed energy deposition, sensing, control, open protocol

16. SECURITY CLASSIFICATION OF:			**17. LIMITATION OF ABSTRACT** SAR	**18. NUMBER OF PAGES** 113	**19a. NAME OF RESPONSIBLE PERSON** Edward W. Reutzel
a. REPORT U	**b. ABSTRACT** U	**c. THIS PAGE** U			**19b. TELEPONE NUMBER *(Include area code)*** 814-863-9891

Executive Summary

Under award N00014-11-1-0668, “Cyber Enabled Direct Digital Manufacturing,” significant process was made in the areas of cyber-systems interfacing, communication construct development, and process monitoring for Additive Manufacturing. Developments were documented and disseminated in the forms of more than seven conference presentations, seven peer-reviewed publications (including four journal articles), and one provisional patent. This program, conducted from July 2011 thru September 2014, was initially led by Dr. Shawn Kelly and was transitioned to Dr. Edward Reutzel in January 2012. Dr. Abdalla Nassar was a significant and noteworthy contributor to project efforts.

Primary outcomes of the program include:

1. Development and demonstration of a digital thread for directed-energy additive manufacturing.
2. Development and demonstration of open communication schemas for directed-energy deposition processes.
3. Improved understanding of impact of direct digital deposition on thermal build-up and resultant stress and distortion for Ti6Al4V, and support for improved modeling and simulation strategies.
4. Direct, automated linking of simulation and sensor data with part build up.
5. Demonstration of real-time control of path plan along with synchronized, multi-sensor data acquisition.
6. Preliminary development of a defect detection technique for directed-energy deposition based on optical emission spectroscopy.
7. Invention of a method for deposition of overhanging structures using directed-energy deposition.

Acknowledgements

We acknowledge Mr. Edward A. Good (engineering assistant ARL Penn State) for assistance in preparing metallographic samples, Mr. Todd Spurgeon (undergraduate Virginia Tech) for contributions to the path planning work, Dr. Jay Keist (faculty ARL Penn State) for contributions to assessment of microstructures, Dr. Pan Michaleris (faculty PSU Dept of Mech Engr) for contributions to path extraction algorithm development, Dr. Jarred Heigel (former graduate student PSU Dept of Mech Engr) for contributions to understanding of directed energy depositoin, Dr. Shawn Kelly (formerly faculty ARL Penn State) and Dr. Todd Palmer (faculty ARL Penn State) for early leadership.

Funding for this work was provided by the Office of Naval Research, under Contract No. N00014-11-1-0668. Any opinions, findings and conclusions or recommendations expressed in this publication are those of the authors and do not necessarily reflect the views of the Office of Naval Research.

Certification

The contractor, The Pennsylvania State University, hereby certifies that, to the best of its knowledge and belief, the technical data delivered herewith is complete, accurate, and complies with all requirements of the contract.

Contents

Executive Summary i

Acknowledgements ii

Certification ii

Contents iii

Figures iv

Background 1

Developments under the CeMS Program 1

- A Digital Thread for Additive Manufacturing 1
- Applications of the Thread 2
- Closed-loop control of build plan 3
- Powder flow monitoring 4
- Optical emission spectroscopy for defect detection 5
- Deposition of overhanging structures by pulsed, voxel-wise buildup 6

Summary 7

References 8

Appendix 1 – Publications, Presentations, and Patents A1-1

Appendix 2 – A proposed digital thread for additive manufacturing A2-1

Appendix 3 – A survey of sensing and control systems for machine and process monitoring of directed energy, metal-based additive manufacturing A3-1

Appendix 4 – Intra-layer closed-loop control of build plan during directed energy additive manufacturing of Ti–6Al–4V A4-1

Appendix 5 – Sensing defects during directed-energy additive manufacturing of metal parts using optical emissions spectroscopy A5-1

Appendix 6 – Additive Manufacturing of Ti-6Al-4V Using a Pulsed Laser Beam A6-1

Appendix 7 – Thermo-mechanical model development and validation of directed energy deposition additive manufacturing of Ti–6Al–4V A7-1

Appendix 8 – Patent Application: Method for manufacturing overhanging materials by pulsed, voxel-wise buildup A8-1

Figures

Figure 1: Software to link additive manufacturing systems to FEM simulations. 2
Figure 2: Infrastructure for near-real-time sensing and control of directed-energy AM process................ 3
Figure 3: Microstructural changes resulting from interruptions due to powder flow disruptions 4
Figure 4: Illustration of in-process powder flow monitor for directed-energy deposition 5
Figure 5: Lack of fusion defects linked to optical emissions spectra. 6

Background

Interest in use of Additive Manufacturing (AM) techniques for metal-based components has exploded in recent years, fueled by AM's promise to cost-effectively build and repair complex designs directly from CAD, to make parts that are no producible by conventional fabrication techniques, and to repair high value items that have been removed from service due to corrosion, wear, or other damage. AM applications of particular interest to the Navy and DoD aerospace community include fabrication and repair of integrally-bladed rotors (also known as blisks), various other engine components, rib-web structures for aircraft sub-structures, vertical launch system tubes, and main and auxiliary seawater valves. The list of potential applications will grow.

The novel capabilities offered by AM, however, come at an expense. Manufacturing of even simple components via AM is complex, typically requiring hundreds or thousands of individual laser depositions. Quality assurance for such a complex process requires sophisticated data management approaches along with the development of in-process sensors and controls.

Developments under the CeMS Program

Under the Navy CeMS program (ONR BAA 11-003) program, the primary needs and open questions related to the development of a cyber-physical system for AM were assessed. A need to link component build plans and processing conditions with physics-based simulations was identified as critical for the improved understanding of the physical processes, as well as for model validation, build-plan optimization, and verification of part quality. The tight integration of real-time sensing, computation, and control into AM systems was also identified as a critical requirement to further process understanding, validation, and control.

In this section, the basic developments related to integrating simulations with build conditions, and with real-time sensing, computation, and control, will be briefly described. Appendix 1 lists papers and presentations supported by this work, Appendix 2-6 provides copies of published manuscripts related to the developments described here, and Appendix 7 contains the patent application covering deposition of overhanging structures that was supported with this funding.

A Digital Thread for Additive Manufacturing

One of the difficulties in simulation and control of AM processes, as well as in developing fundamental understanding, is access to processing conditions and build plans. Because many AM machine manufacturers use proprietary, binary file formats, it is difficult or impossible for operators and modelers to determine how a part was actually produced. Without essential process parameters, such as beam power and processing speed, along with vectors and timing of contours and hatches, modelers have to estimate inputs into their models and experimentalists are sometimes left to wonder "what went wrong" during part builds. Many modelers have come to rely on hand-coding of individual contours and hatches—not practical for any complex build. To overcome these limitations, the authors have developed and published an open-access AMSF file format (Nassar and Reutzel, 2013) to enable automatic specification and extraction of processing parameters for a variety of metals-based AM processes.

Further details regarding the development of a digital thread for AM can be found in Appendix 2.

Applications of the Thread

Using the established AMSF file format, the authors have developed and demonstrated two approaches for direct integration of AM processes with numerical simulation:

1) development and demonstration of software for path-planning and parameter selection for Optomec LENS Directed Energy Deposition machines; and,
2) development and demonstration of software for reverse engineering build plans and processing parameters from Optomec LENS machine code.

Both approaches are illustrated in figure 1. In collaboration with Penn State's Dr. Pan Michaleris, and through leveraging of his activities supported by DARPA's Open Manufacturing Program, NSF, and others, the authors have used these tools to demonstrate the value of direct interfacing between the build plan and FEA thermal simulation (Reutzel et al, 2012). Such interaction has enabled thermo-mechanical simulations of complex AM geometries[1].

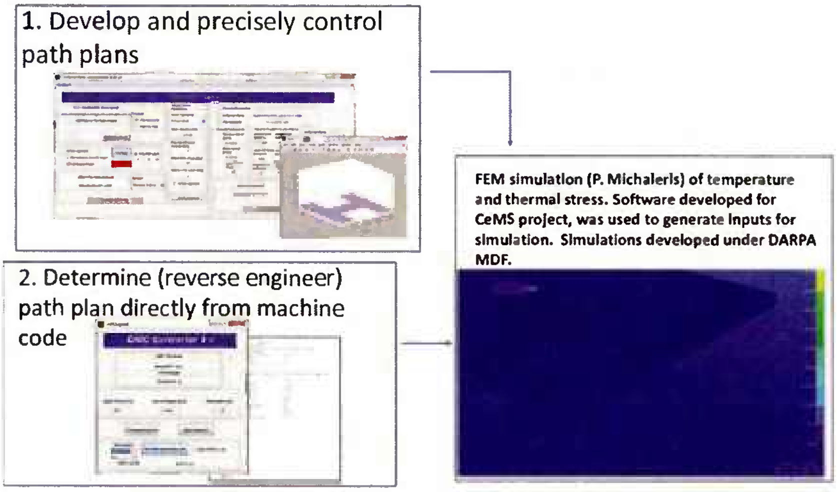
1. Develop and precisely control path plans
2. Determine (reverse engineer) path plan directly from machine code

FEM simulation (P. Michaleris) of temperature and thermal stress. Software developed for CeMS project, was used to generate inputs for simulation. Simulations developed under DARPA MDF.

Figure 1: Under the current CeMS program, software was developed to link additive manufacturing systems to FEM simulations via two paths: 1) custom-written software for path-planning and parameter

---

[1] Michaleris, P., "FEA Thermal Animation of Wheel Build on Optomec LENS," 2013. [Online]. Available: http://www.me.psu.edu/michaleris/research/DDM/wheel_m1_ffw.avi. [Accessed: 05-Mar-2014].

selection; and, 2) custom-written software for reverse engineering build plans and processing parameters extracted directly from Optomec LENS machine code.

In addition to developing infrastructure for direct linking between build plan and FEA thermal simulation, the authors have also developed software and hardware systems that integrate sensors and controls into a commercial directed-energy-deposition AM machine. Figure 2 is an overview of one application of the developed system, which enables real time sensing and control of processing conditions and the build plan within a given slice layer. Using the developed infrastructure, the authors have demonstrated the ability to alter the intra-layer path-plan in real time based on initial temperature and boundary conditions using simple, pyrometer sensors (Reutzel and Nassar, 2014).

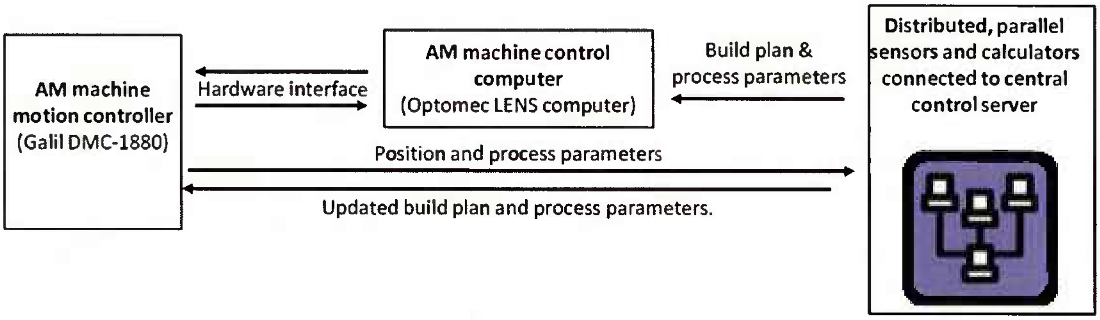
AM machine motion controller (Galil DMC-1880)
Hardware interface
AM machine control computer (Optomec LENS computer)
Build plan & process parameters
Distributed, parallel sensors and calculators connected to central control server
Position and process parameters
Updated build plan and process parameters.

Figure 2: Developed infrastructure for near-real-time sensing and control of directed-energy AM process

Closed-loop control of build plan

To demonstrate this capability, experiments were conducted in which the order of deposited hatches on each layer was selected according to a simple criteria: if the temperature at the start of a hatch exceeds a threshold value for that hatch, skip the current hatch and check the next closest hatch, continue until all hatches on a layer are deposited (Reutzel and Nassar, 2014). The rationale behind this strategy is based on the simple understanding that both the local and global thermal field within a part, during processing, depends upon initial as well as boundary conditions. Control of both global and local thermal fields is critical, since microstructure, thermal deformation, powder-capture efficiency, and build geometry all depend on local and global thermal fields. An alternative controller strategy could be to dwell at the beginning of a hatch until its temperature fell below the desired threshold, but this was not chosen due to the practical need to minimize the total time for part buildup.

Further details regarding the development of new system architecture and closed-loop, intra-layer build plan control for AM, can be found in Appendix 3 and Appendix 4.

Powder flow monitoring

The described architectures also enables process monitoring for quality verification. Developed strategies included powder-flow monitoring and spectroscopy-based defect detection. It is common knowledge among machine operators and OEMs that directed energy AM systems suffer from a variety of powder flow variations and interruptions during processing, due to conditions like clogging of one or more powder nozzle, variations in chamber pressure, or a drop in the pressure of the supply gas. Such interruptions typically require an operator to identify the anomaly, manually halt processing, resolve the problem, and then resume the process. Handling such changes in this manner has been shown to result in microstructural changes (Kelly et al., 2012)—see figure 3. Under this program preliminary efforts ware made towards the development of a powder flow monitoring system (Reutzel and Nassar, 2014), shown in figure 4.

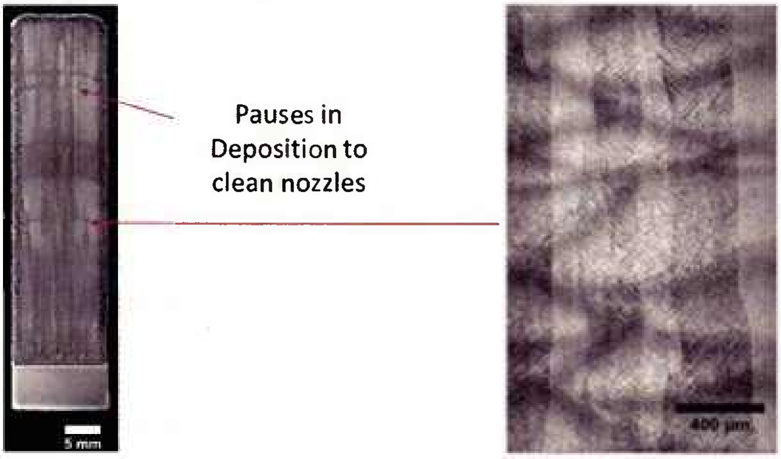

Figure 3: Microstructural changes have been shown to result from interruptions in processing due to powder flow disruptions (Kelly et al., 2012).

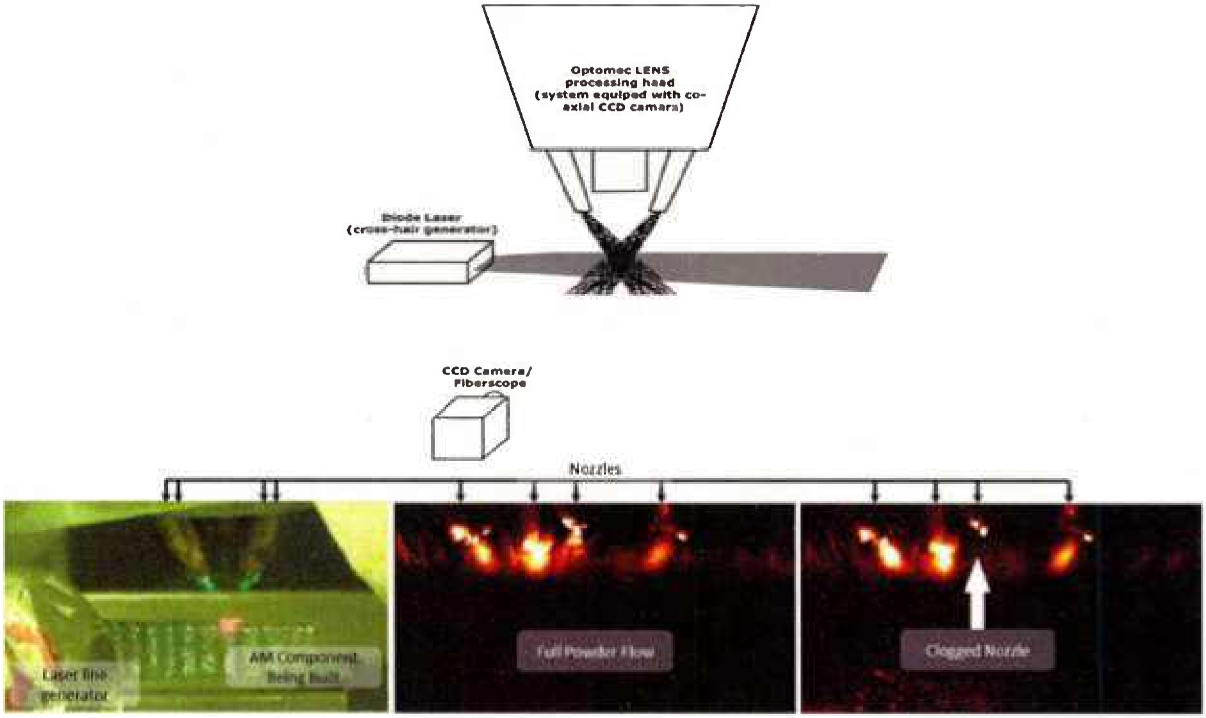
Optomec LENS processing head (system equiped with co-axial CCD camara)
Diode Laser (cross-hair generator)
CCD Camera/ Fiberscope
Nozzles
Laser line generator
AM Component Being Built
Full Powder Flow
Clogged Nozzle

Figure 4: Illustration of in-process powder flow monitor for directed-energy deposition

Further details regarding the powder monitoring systems for AM can be found in Appendix 3.

Optical emission spectroscopy for defect detection

Under this program, optical emission spectroscopy was also investigated as a means to detect defect formation. Preliminary results indicate that lack of fusion defects in Ti-6Al-4V parts, produced via directed energy deposition, may be correlated with atomic titanium (Ti I) and Vanadium (V I) emissions (Nassar et al., 2014). The developed software and hardware tools enable real-time acquisition and synchronization of collected spectra with position and processing conditions. An example of the correlation between defect location and spectral emissions is shown in figure 5.

Further details regarding the development of closed-loop, intra-layer build plan control for AM, can be found in Appendix 6.

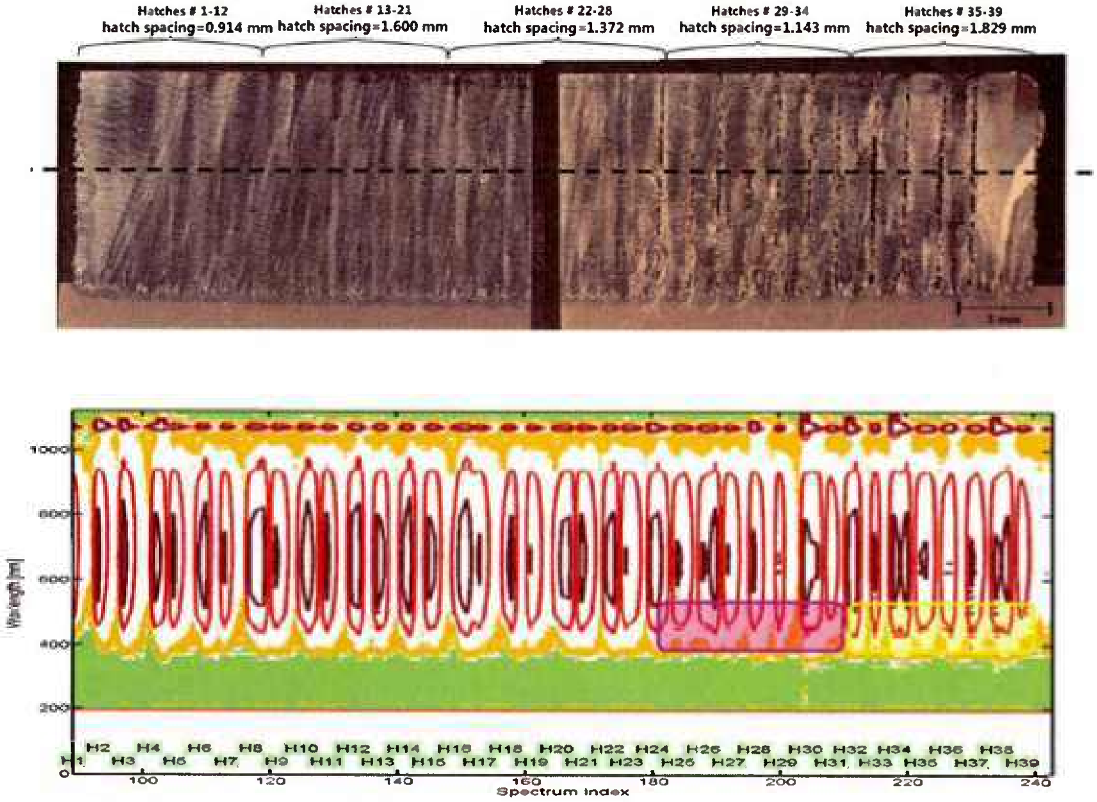

Figure 5: Top: Cross-section of part wherein lack of fusion defects were purposefully introduced. Bottom: Analysis of optical emissions spectra, synchronized with position and collected in real-time, over one layer of the deposition (shown with a dashed line in the top image). Spectral line emissions (Ti I and V I) were detected on hatches where defects occurred.

Deposition of overhanging structures by pulsed, voxel-wise buildup

During these developments, a novel technique for the deposition of overhanging structures by directed-energy deposition was invented. The method relies upon sequential deposition of individual voxels using appropriate build parameters, laser settings, and travel vectors. Overhanging structures with angles, relative to the propagation direction of the laser beam, as high as 60° were demonstrated—far exceeding what is typically possible using similar equipment (~15-25°).

Additional details regarding use of pulsed lasers for directed energy deposition of overhangs can be found in Appendix 6. Additionally, a provisional patent U.S. Patent Application Serial No: 62/051,174; Title: "METHOD FOR MANUFACTURING OVERHANGING MATERIAL BY PULSED, VOXEL-WISE BUILDUP" has been filed for this invention.

Summary

Significant developments related to interfacing, sensing, and control of cyber-physical systems have occurred under the Office of Naval Research "Cyber Enabled Direct Digital Manufacturing" program, award N00014-11-1-0668. Significant achievements have included the development of a digital thread concept for AM. This concept advanced efforts towards a universal schema for communicating data relevant to AM processes. Taking advantage of the developed schema, directed interfacing of build-plan and finite element simulations were enabled. Additionally, sensing strategies were demonstrated, including optical emission spectroscopy for defect detection and powder flow monitoring for powder anemology detection. Real-time control of build plan was also demonstrated and found to significantly impact microstructure and mechanical properties of the deposited Ti-6Al-4V components. A final notable achievement is the invention of a novel method for deposition of directed-energy-deposited high-overhanging structures.

References

Nassar, A.R., Reutzel, E.W., 2013. A Proposed Digital Thread for Additive Manufacturing, in: Solid Freeform Fabrication Symposium Proceedings, University of Texas, Austin, TX.

Nassar, A.R., Spurgeon, T.J., Reutzel, E.W., 2014. Sensing defects during directed-energy additive manufacturing of metal parts using optical emissions spectroscopy, in: Solid Freeform Fabrication Symposium Proceedings, University of Texas, Austin, TX.

Reutzel, E. W., Michaleris, P., Nassar, A., Heigel, J., Palmer, T. A., Martukanitz, R. P., 2012. Connecting Sensors and Models to Physical Systems for Additive Manufacturing, , SAMPE-WSU Direct Part Manufacturing Workshop, Dayton, OH.

Reutzel, E.W., Nassar, A.R., 2014. A survey of sensing and control for metal-based additive manufacturing, in: Solid Freeform Fabrication Symposium Proceedings, University of Texas, Austin, TX.

Kelly, S.M., Reutzel E.W., Palmer T.A., 2012. Impact of Path Planning on Thermal History during Additive Manufacturing of Ti-6Al-4V, ICALEO 2012 Proceedings. Anaheim, CA.

Appendix 1 – Publications, Presentations, and Patents

Conference Publications:

Nassar A R, Reutzel E W, "A Proposed Digital Thread for Additive Manufacturing" in *Solid Freeform Fabrication Proceedings. Proc. 2013* Solid Freeform Fabrication Symposium, Austin, TX 2013.

Nassar A R, Reutzel E W, "Sensing Defects during Directed-Energy Additive Manufacturing of Metal Parts using Optical Emissions Spectroscopy" in *Solid Freeform Fabrication Proceedings. Proc. 2014* Solid Freeform Fabrication Symposium, Austin, TX 2014.

Reutzel E W, Nassar A R, "A Survey of Sensing and Control Systems for Machine and Process Monitoring of Directed-Energy, Metal-Based Additive Manufacturing" in *Solid Freeform Fabrication Proceedings. Proc. 2014* Solid Freeform Fabrication Symposium, Austin, TX 2014. *(Best Paper Award Winner)*

Journal Publications:

Heigel J C, Michaleris P, Reutzel E W, Thermo-mechanical model development and validation of directed energy deposition additive manufacturing of Ti–6Al–4V, *Additive Manufacturing,* 5, 9–19, doi: 10.1016/j.addma.2014.10.003, 2015.

Reutzel E W, Nassar A R, A survey of sensing and control systems for machine and process monitoring of directed-energy, metal-based additive manufacturing. *Rapid Prototyping Journal,* 21, 159–167. doi:10.1108/RPJ-12-2014-0177, 2015.

Nassar A R, Reutzel E W, Additive Manufacturing of Ti-6Al-4V Using a Pulsed Laser Beam. *Metallurgical and Materials Transactions A*, doi:10.1007/s11661-015-2838-z, 2015.

Nassar A R, Keist J S, Reutzel E W, Spurgeon T J, Intra-layer closed-loop control of build plan during directed energy additive manufacturing of Ti–6Al–4V. *Additive Manufacturing,* 6, 39–52. doi:10.1016/j.addma.2015.03.005, 2015.

Presentations

Nassar A R, Reutzel E W, (2014) *Novel Strategies for Control of Microstructure in Directed-energy Additive Manufacturing of Metal Parts* Materials Science & Technology 2014 Conference & Exhibition, Pittsburgh, PA.

Nassar A R, Reutzel E W, (2014) *Sensing with Optical Emissions Spectroscopy for Real-time Defect Detection during Directed-energy Additive Manufacturing of Metal Parts* Materials Science& Technology 2014 Conference & Exhibition, Pittsburgh, PA.

Reutzel E W, Nassar A R (2014) *A Survey of Sensing and Control Systems for Machine and Process Monitoring of Directed-Energy, Metal-Based Additive Manufacturing* Solid Freeform Fabrication Symposium, Austin, TX.

Nassar, A.R., 2014. *Directed Energy Deposition for Additive Manufacturing and Repair Using LENS*. CIMP-3D Industry Practicum: Additive Manufacturing of Metallic Materials, University Park, PA

Nassar A R, Spurgeon T J, Reutzel E W, (2014) *Sensing Defects during Directed-Energy Additive Manufacturing of Metal Parts using Optical Emissions Spectroscopy* Solid Freeform Fabrication Symposium, Austin, TX.

Nassar A R, Reutzel E W, (2013) *A Proposed Digital Thread for Additive Manufacturing* Solid Freeform Fabrication Symposium, Austin, TX.

Reutzel E W, Michaleris P, Nassar, A, Heigel J, Palmer T A, Martukanitz, R. P., (2012) *Connecting Sensors and Models to Physical Systems for Additive Manufacturing,* SAMPE-WSU Direct Part Manufacturing Workshop, Dayton, OH.

Kelly S M, Reutzel E W, Palmer T A, (2012*) Impact of Path Planning on Thermal History during Additive Manufacturing of Ti-6Al-4V*. ICALEO, Anaheim, CA.

Patents

U.S. Patent Application Serial No: 62/051,174; Title: ``METHOD FOR MANUFACTURING OVERHANGING MATERIAL BY PULSED, VOXEL-WISE BUILDUP''

Appendix 2 – A proposed digital thread for additive manufacturing

Nassar A R, Reutzel E W, "A Proposed Digital Thread for Additive Manufacturing" in *Solid Freeform Fabrication Proceedings. Proc. 2013* Solid Freeform Fabrication Symposium, Austin, TX 2013.

A PROPOSED DIGITAL THREAD FOR ADDITIVE MANUFACTURING

A. R. Nassar* and E. W. Reutzel*

*Applied Research Laboratory, The Pennsylvania State University, University Park, PA 16804

Accepted August 16th 2013

Abstract

Additive manufacturing (AM) has been explored by the automotive, aerospace and medical industries for many years but has yet to achieve wide-spread acceptance. This is partially due to the lack of standard frameworks for the exchange of data related to design, modeling, build plan, monitoring, control, and verification. Here, a unified paradigm, built on Extensible Markup language (XML) -based file formats and influenced by the ASTM F291 standard, is proposed, to record and transmit data at every stage of the AM process. This digital thread contains all essential parameters, from design to testing of metal-based AM parts while remaining accessible, traceable and extensible.

1. Introduction

Additive manufacturing (AM) has been explored by the automotive, aerospace and medical industries for many years. The primary advantage of AM over conventional processes is the ability to produce complex and customized objects for low-volume or high-end use at a fraction of the cost and time [1, 2]. Within the aerospace industry in particular, AM of metals has garnered interest and investment, as illustrated by the acquisition of two additive manufacturing companies by GE Aviation in late 2012 [3] and the membership of Lockheed Martin, Boeing and others in the National Additive Manufacturing Innovation Institute [4]. Of primary interests are the fabrication and repair of rib-web structural components, for aircraft sub-structures, and engine components [5].

A recent national emphasis on this technology in the U.S. has highlighted the need to have a unified paradigm for sharing of digital data associated with the process: from design, to simulation, to build plan, to process monitoring and control, to verification [6]. Standards organizations, such as ASTM, have already begun to establish file formats that address some of these data links [7], but additional data formats must be established to realize the greatest potential of cyber-enabled manufacturing. Ideally, data necessary for part design, manufacturing, qualification and testing should be part of a single "digital thread" [8]. That is, essential parameters, from design to testing should be easily accessible, traceable and interoperable with all machines along the process chain.

In order to address data needs at various stages of AM, it is useful to view the entire process holistically. The additive manufacturing process can be simplified and considered as consisting of four phases: part design; path planning; execution of the part buildup; and, testing and verification. This simplified process description is illustrated in figure 1. Each phase of the process requires the generation and storage of a wide assortment of data.

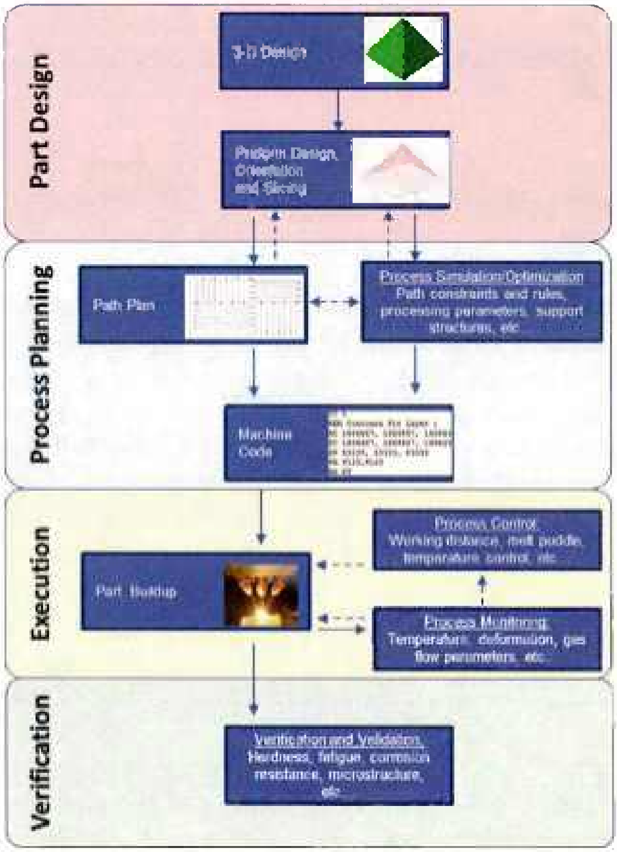
Part Design
3-D Design
Preform Design, Orientation and Slicing
Process Planning
Path Plan
Process Simulation/Optimization
Path constraints and rules, processing parameters, support structures, etc
Machine Code
Execution
Part Buildup
Process Control
Working distance, melt puddle, temperature control, etc
Process Monitoring
Temperature, deformation, gas flow parameters, etc
Verification
Verification and Validation
Hardness, fatigue, corrosion resistance, microstructure, etc

Figure 1: Simplified additive manufacturing engineering process. Feedbacks are illustrated by dashed arrows.

The first step within the part design phase is the construction of a 3-D object. This is typically generated as a solid model using 3-D Computer-Aided Drafting (CAD) software. The surfaces of the constructed object can be described using various file formats including STL or the, recently developed, Additive Manufacturing File (AMF) file [7]. While the STL file only describes geometry, the AMF file also allows materials and textures to be specified. ASTM International, which publishes the AMF standard, has noted that future versions of the standard may also include dimensional and geometric tolerances and provisions for surface roughness, support structures and surface textures. It may be noted that some manufacturers design a 3-D object "preform" to account for expected deformation, shrinkage and final machining of the part. Another factor that may influence part design is build orientation and support structure generation. Part orientation may not only determine the feasibility of the process and the required supports, but also build time and total cost.

Layer by layer slices are next generated using the object surfaces (typically using an STL file). Each slice along the buildup direction is of a defined thickness, dictated by the process conditions of the selected AM system, and is described as being two-and-a-half dimensional (2 ½ D). Within the slice file, the inner and outer perimeters (or contours) of each slice are described. Additional information regarding hatching (filling) of each slice may also be specified. For simple or heavily process-dependent geometries, process planning may be fully or partially manual, rather than automated. In these cases, machine code is directly generated, by an experienced operator, based on desired part geometry and prior process development. That is, rather than slicing a 3-D object, an operator devises a path plan, which may or may not be layer-by-layer, to build the object.

Following the generation of slices, a path plan is generated along each slice for part buildup. At this stage, path optimization—for example, via thermomechanical simulation—can be considered by taking constraints, e.g. build time, fixtures, and deformation, into account. Optimization of thermal history to produce a desired microstructure or to minimize residual stresses may also be considered here. Machine-specific processing parameters must also be specified for path planning. Although critical to defining the final geometry, microstructure, material properties, residual stresses and distortion of the final part, path planning and process data are typically not saved at this point. Instead, machine code is directly generated. While machine code is sufficient for replication of a process on a specific vendor's machine (assuming that essential process variables during part buildup are identical), it cannot be directly used to numerically simulate the process or to reproduce the process using a different vendor's technology. Additionally, interruptions of the buildup process, for example to heat-treat the part, clear a clogged powder nozzle or correct a problem with a wire feed, cannot typically be accounted for within the machine code. As previously noted, a path plan may also be partially or fully manually encoded. Inability to compare machine-to-machine build plans has been identified as a key challenge to structural design and qualification and certification of AM parts [2].

During the execution phase, the part is built-up contour by contour and hatch by hatch according to the machine code. Note, parts need not necessarily be built-up layer by layer. Each hatch and contour can be thought of an individual clad or weld. When thought of in this way, the need for recording of "essential variables", a term borrowed from the welding industry, along each clad or weld becomes readily apparent. While essential variables, such as processing power, translation speeds, part temperature, flow conditions, processing pressure, oxygen concentration, etc.., may be monitored for quality control, continuous recording of these variables is generally not done—no standard format exists for saving this data. Additional data may also include digital video or still images, e.g. melt pool shape or temperature, or measurement of real-time part deformation. Such data can also be fed back for real time process control, e.g. height or melt puddle control.

An additional step, not included in the simplified additive manufacturing engineering process shown in figure 1, is post processing of the part. Specifications for post processing of the part may be conceived within the design and planning phase and implemented at the end of the execution phase or following the testing and verification phase. Heat treatment of AM parts has been shown to have a significant effect on their mechanical properties [9]. A natural extension of the work presented here is the formulation of a standard format describing post processing and heat treatment.

2 Data Standards

To date, standards development has focused on the early stages of the additive manufacturing engineering process, specifically defining the part geometry that can be fed to proprietary slicing and process-planning code. Several of the leading 3-D and 2 ½-D standards are described in this section and illustrated in figure 2.

2.1 Part Design—3-D standards

Part design, as shown in figure 1, is defined here as encompassing the 3-D design along with slice data. Common 3-D and slice file formats are shown in

figure **2** (adapted from [10]). As indicated in figure 2, the STL format is the de facto standard for transmission of 3-D design data. One challenger to the STL format is the ISO 10303 standard [11]. The 10303 standard, also known as STEP, has been championed by some [12] as the standard which ought to replace the STL standard within the AM community. Another, newly introduced competitor is the ASTM F2915 (AMF file) [7] standard. As will be discussed below, the ASTM F2915 standard has a foothold within the AM community and is rapidly gaining popularity.

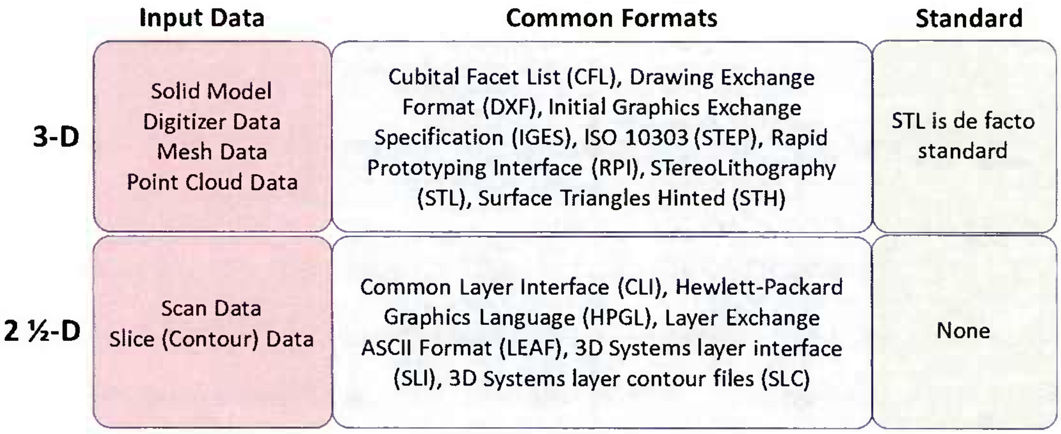

	Input Data	Common Formats	Standard
3-D	Solid Model Digitizer Data Mesh Data Point Cloud Data	Cubital Facet List (CFL), Drawing Exchange Format (DXF), Initial Graphics Exchange Specification (IGES), ISO 10303 (STEP), Rapid Prototyping Interface (RPI), STereoLithography (STL), Surface Triangles Hinted (STH)	STL is de facto standard
2 ½-D	Scan Data Slice (Contour) Data	Common Layer Interface (CLI), Hewlett-Packard Graphics Language (HPGL), Layer Exchange ASCII Format (LEAF), 3D Systems layer interface (SLI), 3D Systems layer contour files (SLC)	None

Figure 2 Common file formats of 3-D and slice files. Adapted from **[10]**.

2.1.1 Standard Tessellation Language Standard

The de facto standard representation of 3D part geometries is the Standard Tessellation Language (STL) format. This representation describes object surfaces using a triangular mesh. Each triangular facet is specified by a unit normal and three vertices. Facets are ordered arbitrarily while the order of vertices, following the right-hand rule, indicates the exterior of the object. An excerpt from an STL file, encoded in ASCII, is shown in figure 3(a).

In addition to its simplicity, the STL format has endured for over two decades due to several advantages. Expressing solids using triangular facets is "simple, robust and reliable" [12]. STL files are also accurate and, when saved in binary format, small [13]. Additionally, the format can accommodate a wide range of 3D representations [12].

The triangular facet approximation and the STL file schema do however have several drawbacks. While the triangular facet approximation is generally accurate, representation of curved surfaces can require a very large number of facets resulting in large file size. Redundancy of information contained within the file format, such as multiple vertices belonging to different facets and explicit inclusion of surface normals, which can be inferred from the order of vertices, also contributes to large file sizes. Another problem is that the format contains no scale information; AM slicing software is often left to guess the units based on part dimensions. The lack of topological information in STL files also contributes to gaps, degenerate and overlapping facets, and non-manifold topologies [12]. Other information, such as material, texture and life-cycle data are also not included within the STL format.

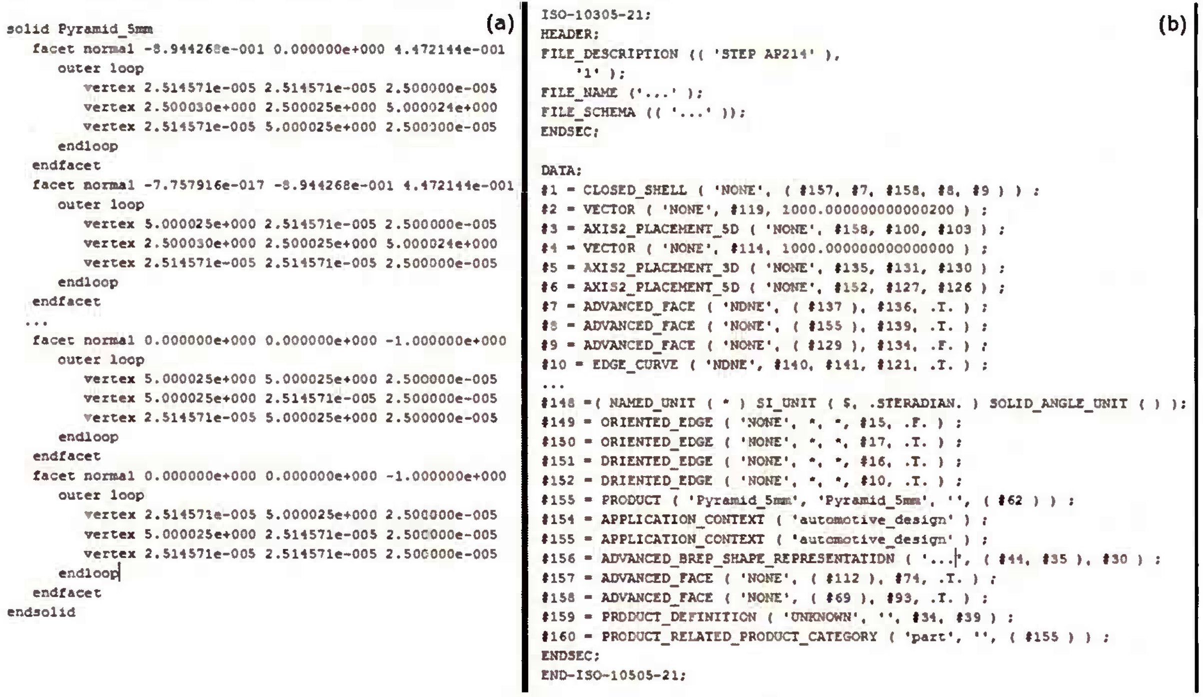

```
solid Pyramid_5mm
   facet normal -8.944268e-001 0.000000e+000 4.472144e-001
      outer loop
         vertex 2.514571e-005 2.514571e-005 2.500000e-005
         vertex 2.500030e+000 2.500025e+000 5.000024e+000
         vertex 2.514571e-005 5.000025e+000 2.500300e-005
      endloop
   endfacet
   facet normal -7.757916e-017 -8.944268e-001 4.472144e-001
      outer loop
         vertex 5.000025e+000 2.514571e-005 2.500000e-005
         vertex 2.500030e+000 2.500025e+000 5.000024e+000
         vertex 2.514571e-005 2.514571e-005 2.500000e-005
      endloop
   endfacet
  ...
   facet normal 0.000000e+000 0.000000e+000 -1.000000e+000
      outer loop
         vertex 5.000025e+000 5.000025e+000 2.500000e-005
         vertex 5.000025e+000 2.514571e-005 2.500000e-005
         vertex 2.514571e-005 5.000025e+000 2.500000e-005
      endloop
   endfacet
   facet normal 0.000000e+000 0.000000e+000 -1.000000e+000
      outer loop
         vertex 2.514571e-005 5.000025e+000 2.500000e-005
         vertex 5.000025e+000 2.514571e-005 2.500000e-005
         vertex 2.514571e-005 2.514571e-005 2.500000e-005
      endloop
   endfacet
endsolid
```

```
ISO-10305-21;
HEADER;
FILE_DESCRIPTION (( 'STEP AP214' ),
    '1' );
FILE_NAME ('...' );
FILE_SCHEMA (( '...' ));
ENDSEC;

DATA;
#1 = CLOSED_SHELL ( 'NONE', ( #157, #7, #158, #8, #9 ) ) ;
#2 = VECTOR ( 'NONE', #119, 1000.000000000000200 ) ;
#3 = AXIS2_PLACEMENT_5D ( 'NONE', #158, #100, #103 ) ;
#4 = VECTOR ( 'NONE', #114, 1000.000000000000000 ) ;
#5 = AXIS2_PLACEMENT_3D ( 'NONE', #135, #131, #130 ) ;
#6 = AXIS2_PLACEMENT_5D ( 'NONE', #152, #127, #126 ) ;
#7 = ADVANCED_FACE ( 'NDNE', ( #137 ), #136, .T. ) ;
#8 = ADVANCED_FACE ( 'NONE', ( #155 ), #139, .T. ) ;
#9 = ADVANCED_FACE ( 'NONE', ( #129 ), #134, .F. ) ;
#10 = EDGE_CURVE ( 'NDNE', #140, #141, #121, .T. ) ;
...
#148 =( NAMED_UNIT ( * ) SI_UNIT ( $, .STERADIAN. ) SOLID_ANGLE_UNIT ( ) );
#149 = ORIENTED_EDGE ( 'NONE', *, *, #15, .F. ) ;
#150 = ORIENTED_EDGE ( 'NONE', *, *, #17, .T. ) ;
#151 = DRIENTED_EDGE ( 'NONE', *, *, #16, .T. ) ;
#152 = DRIENTED_EDGE ( 'NONE', *, *, #10, .T. ) ;
#155 = PRODUCT ( 'Pyramid_5mm', 'Pyramid_5mm', '', ( #62 ) ) ;
#154 = APPLICATION_CONTEXT ( 'automotive_design' ) ;
#155 = APPLICATION_CONTEXT ( 'automotive_design' ) ;
#156 = ADVANCED_BREP_SHAPE_REPRESENTATIDN ( '...', ( #44, #35 ), #30 ) ;
#157 = ADVANCED_FACE ( 'NONE', ( #112 ), #74, .T. ) ;
#158 = ADVANCED_FACE ( 'NONE', ( #69 ), #93, .T. ) ;
#159 = PRDDUCT_DEFINITION ( 'UNKNOWN', '', #34, #39 ) ;
#160 = PRODUCT_RELATED_PRODUCT_CATEGORY ( 'part', '', ( #155 ) ) ;
ENDSEC;
END-ISO-10505-21;
```

Figure 3: Comparison of an (a) STL file with a (b) STEP file, both in ASCII format.

2.1.2 ISO 10303 Standard

The ISO 10303 standard, informally known as STandard for the Exchange of Product model data (STEP), was developed by the International Standards Organization (ISO) with the aim of establishing a single standard for product life-cycle data [11]. Life-cycle data extends beyond geometric data, such as that included in an STL file, and was envisioned to include all information regarding a product—from initial design to disposal.

STEP data are transferred between systems using a neutral 10303 format. An excerpt of a STEP file is included in figure 3(b). Schemas, descriptions of the structure and restraints on contents, of entries within the 10303 format are specified in the EXPRESS language. The EXPRESS language was initially developed for 3D geometrical modeling but, much like XML, can be extended to include any type of entity [14]. Data exchange standards defining the neutral 10303 format are called Application Protocols (APs). A large number of Application Protocols have been written, including those defining neutral file formats for exchanging drafting, 3D designs, structural analysis, electronic assembly, dimensional inspection, plant spatial configuration, material, verification, product life cycle and numerical control process plan data [15].

The use of STEP for additive manufacturing processes has been championed by several authors—see [12] and references therein. A primary advantage of using STEP is its ability to transfer not only process parameters and planning data but also “the results of build simulation and analyses on how different scan strategies will affect the final part” [12]. However, APs specific to additive manufacturing have yet to be developed. Other barriers facing the adoption of STEP for AM applications include the required familiarity with the, very complex, EXPRESS language and slow development of APs, compared with XML standards [14].

2.1.3 ASTM F2915 Standard

The ASTM F2915 standard specifies an XML (Extensible Markup Language) -based file format for additive manufacturing files [7]. XML hold several advantages over the EXPRESS language and other formats: it is self-describing and human-readable; it is simple to understand and use; and, it is ubiquitous and commonly used for online data exchange [16]. In addition to this, XML is extensible by nature—users can create and define tags, as they wish, to meet their specific needs. Files which conform to the ASTM F2915 standard are known as Additive Manufacturing File (AMF) files.

Within an AMF file, object surfaces are described by a triangular mesh. As in the STL format, each triangle is specified by a unit normal and three vertices. However, unlike the STL format, the AMF standard allows definition of curved triangles, in order to better model curved geometries using fewer triangular facets, and includes material, texture and constellation descriptions. Additional information can also be included as metadata. Metadata elements can be used to specify attributes of the overall file, such as authorship and part description, or attributes of surfaces, materials, textures or constellations. Moreover, the AMF format is such that STL files can be converted to AMF files directly and without loss of information [7].

A complete description of the AMF file is available in ASTM F2915 standard [7]. Here, portions of the file structure will be summarized for the reader’s convenience. Five top-level elements are specified within the AMF file format [7]: <object>, <material>, <texture>, <constellation> and <metadata>. All five elements are children of an <amf> element, which is the root element and are specified as follows.

- Surfaces of one or more build objects are defined within <object> elements.
- The <object> element requires the definition of a child mesh element, <mesh>.
- The <vertices> element is a child of the <mesh> element and contains a list of implicitly numbered vertex coordinates, contained within <vertex> element.
- Cartesian coordinates of each vertex are defined within a <coordinates> element, which is a child of the <vertex> element and contains the <x>, <y> and <z> elements as children.
- The object element must also contain at least one volume element, <volume>, which is a sibling of the <mesh> element.

- The <volume> element defines a closed surface based on the mesh of <triangle> elements.
- Each <triangle> elements is a child of the <volume> element and contains three vertices within <v1>, <v2> and <v3> elements.
- Contained in each of the <v1>, <v2> and <v3> elements is an index of a previously defined vertex.

Materials specified within <material> elements are referenced to within each <volume> element. Multiple materials, as well as mixed and graded materials, can be specified. Additionally, 2-D and 3-D texture maps can be encoded within the AMF file as a string of bytes (Base64) within the <texture> element. The <constellation> element can be used to specify the position and orientation of multiple objects. Any other attributes of the overall file or of surfaces, materials, textures or constellations can be included within <metadata> elements. An excerpt of an AMF file is shown in figure 4.

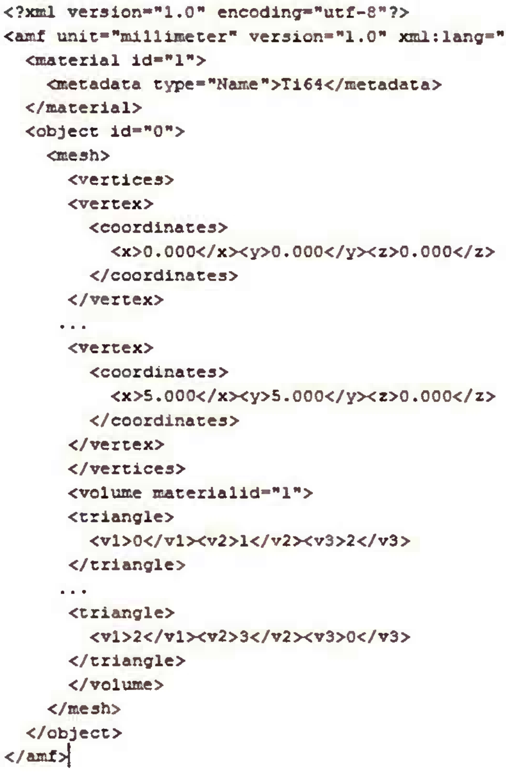

```
<?xml version="1.0" encoding="utf-8"?>
<amf unit="millimeter" version="1.0" xml:lang="en">
  <material id="1">
    <metadata type="Name">Ti64</metadata>
  </material>
  <object id="0">
    <mesh>
      <vertices>
      <vertex>
        <coordinates>
          <x>0.000</x><y>0.000</y><z>0.000</z>
        </coordinates>
      </vertex>
     ...
      <vertex>
        <coordinates>
          <x>5.000</x><y>5.000</y><z>0.000</z>
        </coordinates>
      </vertex>
      </vertices>
      <volume materialid="1">
      <triangle>
        <v1>0</v1><v2>1</v2><v3>2</v3>
      </triangle>
     ...
      <triangle>
        <v1>2</v1><v2>3</v2><v3>0</v3>
      </triangle>
      </volume>
    </mesh>
  </object>
</amf>
```

Figure 4: AMF file.

Although many have tried to modify, extend or replace the de facto standard of the STL file, the AMF file and other standards developed by the ASTM F42 committee have a promising chance of gaining hold within the additive manufacturing community. Reasons for this include the participation of a number of influential leaders in the AM field, including research laboratories, software developers, machine manufacturers, part fabricators, and the Society of Manufacturing Engineers' (SME) Rapid Technologies and Additive Manufacturing (RTAM) community [17]. Furthermore, the signing of a cooperation agreement between the ASTM F42 and ISO Technical Committee 261 allows for fast-tracking of ASTM standards as ISO standards [18]. Several popular commercial slicing packages, including Materialise® Magics 17 and netfabb, already support the AMF file format.

As a result of its origins in rapid-prototyping with non-metallic materials, a primary limitation of the ASTM F2915 standard is that not all essential data pertinent to laser- and electron-beam-based AM processes can be easily specified within an AMF file. For instance, information regarding the sequence and timing of deposition paths has been shown to influence the microstructure, residual stresses, and deformation of laser-deposited components [5] [19] [20]. The standard does allow for inclusion of non-standard data as metadata or as a new, unofficial element. According to the ASTM F291 standard [7], unofficial elements can be ignored by readers until officially accepted into the standard. However despite this advantage, the standard does not provide a clear framework for the inclusion of essential parameters required for replication or numerical modeling of a 3D part build. Specification of the laser or electron-beam deposition path would require the generation of a complex arrangement of <metadata> elements or the creation of unofficial elements. This however undermines several advantages of the XML Schema defined by ASTM F291—that it is intuitively structure, simple and standard.

2.2 Part Design—2 1/2-D Standards

Whereas 3-D data currently has a de facto, technology-independent, standard, in the form of an STL file, no de facto standard exists for slice data. Rather, several open-source and proprietary file formats are used, including Common Layer Interface (CLI), 3D Systems layer interface (SLI), 3D Systems layer contour files (SLC) and Layer Exchange ASCII Format (LEAF). Vendor-specific file formats are also often referred to as SLC or SLI files [3]. Among these formats, the open-source CLI is notable for its simplicity—slices are defined using polyline contours which specify both external and internal boundaries. Additionally, the CLI files format standard is freely available, both in American Standard for Information Exchange (ASCII) and binary encoding, on the internet (http://www.forwiss.uni-passau.de/~welisch/papers/cli_format.html).

CLI files begin with a header section which contains information regarding the file type (binary or ASCII), the units and the file version. The header may also contain the date, the coordinates of a bounding box, which contains the part, the number of layers used to construct the part as well as comments regarding the software used to produce the slice or the author. Contained within the body of a CLI file are geometric commands specifying coordinates of polylines used to construct outer and inner contours as well as hatches. Outer contours are specified using a counter-clockwise ordering of points while inner contours are specified using a clockwise ordering, when viewed in the negative build-up direction. A direction parameter is also included to reaffirm the ordering and indicate open lines, which can be used to indicate hatching or support structures [21]. A full description of the file format is available online [22].

2.3 Process planning standards

Processing paths are typically specified based on hatches constructed within slicing software, taking into account processing parameters such as hatch spacing and layer thickness, or directly by the AM machine's internal software. In most cases, planning and process data are not saved. Rather, machine code is directly generated. No standard specifications exist for transmitting technology-neutral processing paths and parameters. It may however be noted that the Hewlett-Packard Graphics Language (HPGL) [23], originally developed as a command set for pen plotters, and G-code [24] are commonly used with AM machines.

2.4 Execution and Verification Standards

No standards currently exist for data produced and recorded during the execution and verification phases of the AM process, e.g. temperature history, deformation, gas flow parameters, microstructure, tensile properties, etc... The ASTM F42 committee has to date released four standards related to additive manufacturing: Standard Terminology for Additive Manufacturing—Coordinate Systems and Test Methodologies (F2921), Standard Specification for Additive Manufacturing Titanium-6 Aluminum-4 Vanadium with Powder Bed Fusion (F2924), Standard Terminology for Additive Manufacturing Technologies (F2792) and Standard Specification for Additive Manufacturing File Format (F2915). Many more proposed standards are currently being developed; including, New Practice for Reporting Results of Testing of Specimens Prepared by Additive Manufacturing (WK30107), New Guide for Conditioning of machines and performance metrics of metal laser sintering systems (WK25479) and New Practice for Machine Operation for Directed Energy Deposition of Metals (WK37654).

Some of the proposed standards currently under review by the ASTM F42 committee may meet the need for standardized data formats at some phases of the AM process. For example, perhaps the New Practice for Reporting Results of Testing of Specimens Prepared by Additive Manufacturing (WK30107) may provide a standard way for reporting data recorded during the verification and validation phase. In the meantime, however, there is a clear and imminent need for standardized, or at the least open and easily-understood, formatting to enable definition of essential process data necessary for numerical simulation, replication and validation of numerical simulations, as well as for recording specimen test data.

3 A Proposed Digital Thread for AM

Rather than attempt to modify the AMF file format to include all the data required at every stage of the AM process, it is proposed that additional file formats be produced, each containing data, or a subset of data, pertinent to a specific phase of the process. Each format will mirror the example set by the ASTM F291 standard; the file formats will aim to be technology-independent (where possible), easy to understand, scalable, require reasonable computer resources to read and write, backwards compatible with existing file formats (where possible) and allow for easy extensibility to accommodate advances in technology. Like the ASTM F291 standard, data will be encoded in XML [16]. The proposed files are summarized in table 1 and will be discussed in the next sections. Together, the files will form a common digital thread. This digital thread will enable designers, manufacturers, end-users and modelers to easily transfer information and speak a common language with the ability to access only information which is of interest or all data at every phase of the AM process. Work is currently underway at Applied Research Laboratory at Penn State University to utilize the formats proposed here. This is viewed as key to cross-linking ongoing experimental work with simulation capabilities and verification efforts. This publication will only deal with the part design and process planning phases. The execution and testing phases are more complex and will be the topic of a future publication.

Table 1: Proposed file formats to contain data necessary at every phase of the additive manufacturing engineering process

Phase	Data Type	File Format
Part Design	3-D Design	AMF
	Slice	AMSF
Process Planning	Path Plan (and processing parameters)	AMPF
Execution	Sensor Data and Qualification Record	AMQF
Testing	Verification and Validation Data	AMVF

3.1 Slice

In addition to the AMF file, used to specify the 3-D design, four additional file formats are believed necessary and will be specified. The Additive Manufacturing Slice File (AMSF) will contain data regarding the slicing of the 3-D object and will be backwards compatible with the CLI file format. The AMSF will form part of the digital thread connecting all AM files. As such, information regarding the material, texture and color and constellation may be inferred from the AMF file. For example, the "materialid" attribute may be used within the AMSF to refer to a material defined within the AMF file. Alternatively material, texture, color and constellation data may also be specified within AMSF, following the AMF file standard. For cases in which both AMF and AMSF specify this data, data in the AMSF shall take precedence. An excerpt of the proposed AMSF file format is shown in figure 5.

As with the CLI format, the AMSF format will represent slices along the z-axis (the build-up direction as defined by ASTM F2921 [25]) using a polyline representation of the slice contours (boundaries). The definition of inner and outer contours as well as open lines and hatches will be identical to the CLI format [22]. Outer contours will be specified using a counter-clockwise ordering of points while inner contours will be specified using a clockwise ordering, when viewed in the negative build-up direction. As with the CLI format, a direction parameter will also be included to reaffirm the ordering and indicate open lines. Hatches will also be specified as in the CLI format, start and end (x,y) coordinates will be specified for each hatch.

```
<?xml version="1.0" encoding="utf-8"?>
<amsf angle="degree" unit="millimeter" version="1.0"
xml:lang="en">
  <object id="0">
    <transformation>
      <translation>0</translation>
      <rotation>0</rotation>
      <scaling>1</scaling>
    </transformation>
    <dimension>
      <x1>0</x1>
      <y1>0</y1>
      <z1>0</z1>
      <x2>5</x2>
      <y2>5</y2>
      <z2>5</z2>
    </dimension>
    <slices materialid="1">
      <numberOfSlices>19</numberOfSlices>
      <slice>
        <z>0.254</z>
        <polyline>
          <direction>1</direction>
          <points>
            <numberOfPoints>5</numberOfPoints>
            <pointCoordinates>
              <p1x>0.12701</p1x>
              <p1y>4.873</p1y>
              <p2x>0.12701</p2x>
              <p2y>0.12701</p2y>
              <p3x>4.873</p3x>
              <p3y>0.12701</p3y>

              <p4x>4.873</p4x>
              <p4y>4.873</p4y>
              <p5x>0.12701</p5x>
              <p5y>4.873</p5y>
            </pointCoordinates>
          </points>
        </polyline>
      </slice>
                  ...
      <slice>
        <z>4.826</z>
        <polyline>
          <direction>1</direction>
          <points>
            <numberOfPoints>5</numberOfPoints>
            <pointCoordinates>
              <p1x>2.413</p1x>
              <p1y>2.587</p1y>
              <p2x>2.413</p2x>
              <p2y>2.413</p2y>
              <p3x>2.587</p3x>
              <p3y>2.413</p3y>
              <p4x>2.587</p4x>
              <p4y>2.587</p4y>
              <p5x>2.413</p5x>
              <p5y>2.587</p5y>
            </pointCoordinates>
          </points>
        </polyline>
      </slice>
    </slices>
  </object>
</amsf>
```

Figure 5: Structure of proposed AMSF file format.

Ideally, all axes coordinates should conform to the ASTM F2921 standard [11]. This standard specifies an absolute, right-handed coordinate system having an origin at the center of the build volume, a Z-axis pointing in the build-up direction, an X-axis parallel to the front of the machine (pointing from left to right) and a Y-axis perpendicular to the X and Z axes. There is however a potential conflict between the ASTM F2921, coordinate system, standard and the ASTM F2915, AMF file, standards, as well as with the standard proposed here. The AMF file standard was designed for backwards compatibility with STL files. However, STL files typically require positive coordinates. While some software, such as SolidWorks 2012, do allow export of STL files with negative coordinates, others, like AutoCAD 2012, do not allow this. Therefore, vertex coordinates for files directly converted from STL to AMF will not conform to the ASTM F2921, coordinate system, standard. Moreover, some slicing formats, such as CLI and SLI, do not typically support negative coordinates—unsigned integers are typically used to encode point coordinates. Therefore, files directly converted from the CLI format to the proposed AMSF format may also not adhere to the ASTM F2921, coordinate system, standard. This seemingly trivial conflict may result in significant confusion at later stages in the digital thread—for example, in identifying the location where sensor data was recorded. Therefore, to maintain backwards compatibility to the STL and CLI formats, maintain compatibility with existing drafting and slicing software and reduce confusion, it is recommended that all coordinates be specified in the positive X-Y-Z octant within the initial AMF file. Additionally, any translation, rotation or scaling from the original AMF file should be specified within the AMSF.

One more point should be made with respect to the Z-axis coordinates of Slice files. The first slice (z=0) is typically empty. Some slicing software specify an empty first slice (at z=0), others begin with the first slice for which contours can be defined (at z= slice thickness). That is, since there is nothing to be sliced through at the bottom of the part, contours are not specified. Therefore, the first slice for which contour coordinates are specified will be where the z-axis equals the slice (layer) thickness. This may cause some confusion as some deposition systems define the starting position of the process at z=0. Slices can be thought of as defining the top z-coordinate of each layer.

The file declaration will be identical to that specified within the AMF file. The <amsf> element will be the root element. Within the <amsf> element, the version and unit attributes will be specified as in the AMF file but an additional attribute, angle, will be added. Possible values for the angle attribute will be "degree" and "radian." In its absence, "degree" will be assumed as the value of the angle attribute. Also, as in the AMF file, <metadata> elements will be used to specify file name information as well as any additional element or object information. Other elements will be specified as follows:

- The <object> element will be a top-level element. Within it, a unique identification number, id, attribute will be contained beginning with "0," for the part. The id number should equal the objectid, specified within the AMF file, of the sliced object.
- The <transformation> element will be a child of the <object> element. The <translation>, <rotation> and <scaling> elements will be children of the <transformation> element.

Their element contents will specify translation distance, rotation angle and scaling factor, respectively, applied to the part, specified within the AMF file, prior to slicing. Transformation order shall be implied by the order of the <translation>, <rotation> and <scaling> elements.

- The <dimension> element will be a sibling of the <transformations> element and will be used to specify the boundaries of a bounding box which contains the part. Note that the bounding box should enclose the object, described in the AMF file, to be sliced, not just the slices. Coordinates of the boundary box will be specified within the contents of the <x1>,<y1>,<z1>,<x2>,<y2> and <z2> elements, which will be children of the <dimension> element. Coordinates should be specified such that the contents of <x1> are less than <x2>, etc…
- The <slices> element will be a child of the <object> element. It will contain the <numberOfSlices> element and the <slice> element. An optional materialid attribute may be specified within the <slices> element. This attribute should refer to a material specified within the AMF file or within the AMSF.
- The number of slices specified for the object will be contained within the <numberOfSlices> element. If included, an empty first layer counts towards the total number of layers.
- The <slice> element will be a child of the <slices> element and a sibling of the <numberOfSlices> element. In the case of graded materials, an optional materialid attribute may be specified within the <slice> element instead of the <slices> element. This attribute, which allows for graded structures, should refer to a material specified within the AMF file or within the AMSF.
- Children of the <slice> element will include the <z> element along with the <polyline> element.
- The contents of the <z> element will define the z-axis coordinate at which a slice through the object, specified in the AMF file, was made. That is, the z-coordinate specifies the top of each layer.
- The <polyline> will have the <direction> and <points> elements as children.
- The contents of the <direction> element will be a redundant specification of the polyline orientation, where 0 indicates an internal contour, 1 an external contour and 2 an open line. To maintain compatibility with CLI files, open lines may be used to specify hatches or support structures. Orientation will be defined by the <direction> element in case of a discrepancy between the order of points and the <direction> element.
- The <numberOfPoints> element will be a child of the <points> element and will contain the number of points used to construct the polyline.
- The <pointCoordinates> element will be a child of the <points> element and will contain <p1x>,<p1y>,<p2x>,<p2y>,…,<pnx>,<pny> as children elements—the x and y coordinates of points along the polyline will be the contents of these elements. A clockwise ordering of points, when viewed in the negative z (build) direction, will

indicate an internal contour while a counter-clockwise ordering will indicate an external contour. The first and last coordinates along each polyline must match for closed contours.

Hatches can also be optionally included within the AMSF within a <hatch> element. In the absence of a path specification within the path plan file, which will be described in Section 3.2, the hatching contained within the AMSF shall be assumed to describe the processing path. An excerpt of the hatch contained within an AMSF is shown in figure 6. Note that, though hatches provide a machine or scan path, alone they do not provide enough information to perform machine programming or simulation, i.e. information such as the processing speed, laser/E-beam parameters and material feed rate are not included.

- The <hatch> element will be the child of the <slice> element.
- The <numberOfHatches> element and < hatchCoordinates > element will be children of the <hatch> element.
- The contents of the <numberOfHatches> element will be the number of hatches.
- The <hatchCoordinates> element will contain <hp1sx>, <hp1sy>, <hp1ex>, <hp1ey>,…, <hpnsx>, <hpnsy>, <hpnex>, <hpney> as child elements. The x and y coordinates of the start and end points of each hatch will be the contents of these elements.

```
<hatch>
        <numberOfHatches>9</numberOfHatches>
        <hatchCoordinates>
          <hp1sx>0.12701</hp1sx>
          <hp1sy>0.40201</hp1sy>
          <hp1ex>4.873</hp1ex>
          <hp1ey>0.40201</hp1ey>
          <hp2sx>0.12701</hp2sx>
          <hp2sy>0.95201</hp2sy>
          <hp2ex>4.873</hp2ex>
          <hp2ey>0.95201</hp2ey>
          . . .
          <hp8sx>0.12701</hp8sx>
          <hp8sy>4.252</hp8sy>
          <hp8ex>4.873</hp8ex>
          <hp8ey>4.252</hp8ey>
          <hp9sx>0.12701</hp9sx>
          <hp9sy>4.802</hp9sy>
          <hp9ex>4.873</hp9ex>
          <hp9ey>4.802</hp9ey>
        </hatchCoordinates>
      </hatch>
```

Figure 6: Example of hatches contained within an AMSF

3.2 Path Plan

Data regarding the path plans and processing parameters, such as power, speed and time will be contained within an Additive Manufacturing Path File (AMPF). This file captures the information necessary to generate machine code to drive a scanner or linear stages and to control the energy source, or to perform a thermomechanical simulation. While the path (AMPF) file contains sufficient data for reconstruction of slices (AMSF), it will be distinct in that it contains points and vectors describing the path of deposition as well as essential processing parameters required for replication and modeling. In contrast, the slice file exclusively contains a slice-based representation of the part. In other words, although geometric data contained within the AMF and AMSF files can, in principle, be reconstructed using the AMPF, they will be kept separate to ensure compatibility and ease of comparison with STL and CLI file formats, respectively, while still remaining part of the continuous digital thread. For cases in which AMSF contains hatch information and AMPF specify paths, data in the AMPF shall take precedence, with respect to the actual deposition path.

The path plan file (AMPF) will be structured similar to the AMF and AMSF files. An excerpt of an AMPF is shown in figure 7. The file declaration will be identical to that specified within the AMF and AMSF files. The <ampf> element will be the root element. Within the <ampf> element, the version unit and angle attributes will be specified as in the AMF file but additional attributes, time, mass, temperature, pressure, energy, power, voltage, current and flow will be added. Possible values for each attribute, along with default values, are given in table 2.

Table 2: Attributes contained within the <ampf> element specifying units.

Attributes	Possible Values	Default Value
unit	"millimeter", "inch", "foot", "meter", "micrometer"	"millimeter"
angle	"degree", "radian"	"degree"
time	"second", "millisecond", "hour"	"second"
mass	"gram", "kilogram", "pound"	"gram"
temperature	"celsius", "fahrenheit", "kelvin"	"celsius"
pressure	"pascal", "bar", "atm", "torr", "psi"	"pascal"
energy	"joule"	"joule"
power	"watt", "kilowatt"	"watt"
voltage	"volt", "kilovolt"	"kilovolt"
current	"ampere",	"ampere"
volume	"liter", "gallon", "cubicCentimeter", "cubicMeter", cubicInch", "cubicFoot"	"liter"

Variables essential for modeling and reproducing the process will be contained at the beginning of the AMPF file. In determining which process variables ought to be specified, Weld Process Specification (WPS) standards adopted by the American Welding Society (AWS C7/C7.4M [26]) as well as by the American Society of Mechanical Engineering (ASME Boiler and Pressure Vessel Code, Section IX [27]) provide a starting point for specification of essential variables in AM processes. Both codes specify similar variables. It may be noted that equivalent or analogous variables are also used in electron beam welding WPS [28]. It should also be noted that many processes may not require specification of the all parameters and variables discussed in the following paragraphs. For those processes, users may wish to specify only those parameters which are essential to their process.

Many of the variables contained within WPS specifications for laser and electron-beam welding are directly applicable to additive manufacturing processes using lasers and electron beams. The recently adopted ASTM F2924 [29] standard also provides guidance as to which variable ought to be specified in AM processes. The XML language is especially well-suited for recording and transmitting such structured data. Within the AMPF, general data, such as the company information, date of production and a tracking or part number will be contained within a <general> element. All other data regarding the process will be contained within a <process> element which also contains an "id" parameter. This process id may be referenced further down the digital thread, within the AMVF. The reader is referred to figure 7 for an example of how process variables will be specified. In addition to specification of process variables, the option for including technical drawings or diagrams is also included. Within the <drawing> element, metadata describing the file contents, formatting, size and location will be included—the schema for this is loosely based on the Dublin Core Metadata Element Set (DCMES) vocabulary [30]. In this sense, "virtual datasets" of technical drawings can be constructed without incurring the high costs of data reformatting and transfer [31].

To be clear, the AMPF is not intended to be a qualification record. Variables recorded during processing will be recorded separately in a verification file (AMVF) which may then be used to qualify parts. A list of variables to be specified within the AMPF is shown in table 3. The structure and sample content of elements associated with these variables is illustrated in figure 7.

Table 3: Variables included in the proposed AMPF

Variable Category	Parent Element Type	Variable(s)	Child Element Type
General	<general>	Company Name	<company>
		Date	<date>
		Process/Part Number	<number>
Process	<process>	Laser/E-beam Settings, optics, environment configuration, materials, drawings	<laser>/<eBeam>, <optics>, <environment>, <configuration >, <base>, <filler>, <drawing>
Laser/E-beam Settings	<laser>/<eBeam>	Process category as specified by ASTM F2792	<category>
		Wavelength/Voltage	<wavelength>/<voltage>
		Current, Filament Type	<current>, <filament>
		Nominal beam profile at work piece	<profile>
		Laser Beam Quality/ E-beam raster	<quality>/<raster>
		Operating Mode	<mode>
		Power	<power>
		Pulse parameters: Energy, rate, length	<energy>, <rate>, <length>
Beam delivery optics	<optics>	Laser Polarization	<polarization>

		Spot size at work piece	<spotAtWorkpiece>
Environment	<environment>	Chamber pressure (absolute not gauge)	<chamberPressure>
		Gas compositions	<gas>
		Flow rates, Gas pressures	<flowRate>, <gasPressure>
		Flow orientation	<flowOrientation>
Process configuration	<configuration>	Angle of beam relative to part normal vector	<beamAngle>
		Controlled substrate temperature, cooling or heating	<substrateTemperature>, <substrateCooling>, <substrateHeating>
		Preheating, interpass and post heat treatment	<preHeating>, <interpassHeating>, <postHeating>
		Process Interruptions	<Interruption>
Base Material	<base>	Type	<type>
		Standard classification: M-number, UNS,ASTM Grade	<mNumber>, <uns>, <astmGrade>
		Shape	<baseShape>
		Geometry: thickness, length along x-axis, length along y-axis	<baseThickness >, <baseXDimension>, <baseYDimension>, <baseXCurvature>, <baseYCurvature>
		Description	<description>
Filler material	<filler>	Type	<type>
		Standard classifaction: UNS, ASTM Grade	<uns>, <astmGrade>
		Shape (wire or powder)	<shape>
		Dimensions: size, distribution, tap density	<size>, <distribution>, <tapDensity>
		Total mass feed rate	<massFeedRate>
		Method of delivery	<deliveryMethod>
		Number of feeders	<numberOfFeeders>
		Position (Feeder to workpiece distance)	<feederWorkingDistance>
		Description	<description>
Technical drawings	<drawing>	Title	<title>
		Creator	<creator>
		Description	<description>
		Date	<date>
		Format	<format>
		Identifier (link to file)	<identifier>
		File size	<fileSize>

Metadata	<metadata>

The AMPF will also define the process path used to construct the part and will include the power <powern>, speed <speedn>, beginning time <timen> and the start (<pnsx>,<pnsy>) and end (<pnex>,<pney>) coordinates for each (n^{th}) path. A constant power for each layer, rather than a power for each path, can be specified using a <power> element and speed within a <speed> element. A materialid parameter can also be contained within <path> or <layer> elements as was done for <layer> and <polyline> elements within the AMSF. The materialid can refer to a material specified within the AMPF file or in one of the upstream files along the digital thread. Materials defined within the AMPF shall take precedence, over those specified in the AMSF or AMF files.

Only paths used for part build up will be included within the AMPF file. Dwell times and time used to move to the beginning of a path will be taken into account by defining the beginning time of each laser path. These elements will be specified as follows:

- The <object> element will be defined as in the AMSF format.
- The <layers> element will be a child of the <object> element and will have the <numberOfLayers> element and the <layer> element as children.
- The <numberOfLayers> element will contain the number of layers to be deposited. The number of layers may be one less than the number of layers specified in the AMSF file since an empty first layer can be used to indicate the first layer, as in a CLI file. This should however be avoided. If an empty first layer is specified in the AMSF file, an empty first layer should be specified within the AMPF file.
- The <layer> element will be a child of the <layers> element and have the <z> element as its child along with the <path> element.
- The <z> element will define the z-coordinate though which the slice was made. The first z-coordinate on which paths are specified should equal the layer thickness. Working distances are with respect to the first z-coordinate on which paths are specified.
- The <path> element will have <numberOfPaths>, <powers>, <times>, <speeds> and <points> as children elements.
- The < numberOfPaths > element will define the number of paths used for part construction.
- The <powers> element will have either the <power> element, for constant power along the entire layer, or <powern> elements, for a defined power along each (n^{th}) path, as children.
- The <speeds> element will have the <speed> element, for constant speed along the entire layer, or <speedn> elements, for a defined speed along each (n^{th}) path, as children.
- The <times> element will have <timen> elements, defining the time at the beginning of each (n^{th}) path. All times are with respect to the first time on the first processing path, typically equal to zero.

- The <points> elements will have <pCoordinates>. Children of the <pCoordinates> element, <pnsx>,<pnsy>,<pnex> and <pney> will define the start and end (x,y) coordinates of each (n^{th}) process path.

```
<?xml version="1.0" encoding="utf-8"?>
<ampf unit="millimeter" time="second"  mass="gram" temperature="celsius" pressure="pascal" power="watt"
volume="liter" version="1.0" xml:lang="en">
        <general>
                <company>AM Corp</company>
                <date>11-12-13</date>
                <number>A1B2C3</number>
        </general>
        <process id="0">
                <category>direct energy deposition</category>
                <laser>
                        <wavelength>1070e-6</wavelength>
                        <profile>TEM00</profile>
                        <quality>1.1</quality>
                        <mode>CW</mode>
                        <power>450</power>
                </laser>
                <optics>
                        <polarization>random</polarization>
                        <spotAtWorkpiece>1042e3</spotAtWorkpiece>
                </optics>
                <environment>
                        <chamberPressure>101325</chamberPressure>
                        <gas>Argon</gas>
                        <flowRate>40</flowRate>
                        <flowOrientation>coxaial</flowOrientation>
                </environment>
                <configuration>
                        <beamAngle>0</beamAngle>
                        <preHeating>one laser scan prior to deposition</preHeating>
                        <postHeating>heat treatment at 700 C for 100 h</postHeating>
                        <interruption>pause process for 30 seconds after layer 5 </interruption>
                </configuration>
                <base>
                        <type>Ti-6AL-4V</type>
                        <mNumber>54</mNumber>
                        <uns>R56400</uns>
                        <astmGrade>5<astmGrade>
                        <baseShape>rectangular plate<baseShape>
                        <baseThickness>3.175</baseThickness>
                        <baseXDimension>76.2</baseXDimension>
                        <baseYDimensions>50.8</baseYDimensions>
                        <description>Flat plate purchased from ABCD corp<description>
                </base>
                <filler>
                        <type>Ti-6AL-4V</type>
                        <astmGrade>5</astmGrade>
                        <fillerShape>Powder</fillerShape>
                        <shape>spherical powder</shape>
                        <size>325 mesh</size>
                        <massFeedRate>0.05</massFeedRate>
                        <deliveryMethod>Coaxial Nozzle</deliveryMethod>
                        <numberOfFeeders>4</numberOfFeeders>
                        <feederWorkingDistance>9.27</feederWorkingDistance>
                        <description>virgin PREP powder purchased from ABCD corp delivered coaxially
                        by four nozzles. Nozzles are located at a working distance of 9.27 mm from work
                        piece.
                        </description>
                </filler>
                <drawing name="PowderNozzles">
                        <title>Orientation of Powder Nozzles</title>
                        <creator>ARL at PSU</creator>
```

```
            <description>Orientation of powder nozzles relative to substrate and laser
            beam.</description>
            <date>01-01-2013</date>
            <format mimeType="application/pdf"></format>
            <identifier>Drawing_Nozzles.pdf</identifier>
            <fileSize>147663</fileSize>
        </drawing>
    </process>
    <object id="0">
        <layers>
            <numberOfLayers>19</numberOfLayers>
            <layer>
                <z>0.254</z>
                <path>
                    < numberOfPaths >9</ numberOfPaths >
                    <powers>
                        <power1>450</power1>
                        <power2>0</power2>
                        <power3>450</power3>
                        <power4>0</power4>
                        <power5>450</power5>
                        ...
                        <power86>0</power86>
                    </powers>
                    <times>
                        <time1>0.00000</time1>
                        <time2>0.89988</time2>
                        <time3>1.79977</time3>
                        <time4>2.69966</time4>
                        <time5>3.59955</time5>
                        ...
                        <time9>37.19910</time9>
                    </times>
                    <speeds>
                        <speed1>10.58333</speed1>
                        <speed2>10.58333</speed2>
                        <speed3>10.58333</speed3>
                        <speed4>10.58333</speed4>
                        <speed5>10.58333</speed5>
                        ...
                        <speed9>10.58333</speed9>
                    </speeds>
                    <points>
                        <pCoordinates>
                            <p1sx>1.27010</p1sx>
                            <p1sy>0.40201</p1sy>
                            <p1ex>4.8730</p1ex>
                            <p1ey>0.40201</p1ey>
                            <p2sx>0.12701</p2x>
                            <p2sy>0.95201</p2y>
                            <p2ex>4.8730</p3x>
                            <p2ey>0.95201</p3y>
                            ...
                        </pCoordinates>
                    </points>
                </path>
            </layer>
            ...
        </layers>
    </object>
</ampf>
```

Figure 7: Structure of proposed AMPF file format.

5. Discussion, Concluding Remarks and Ongoing Work

The digital thread for additive manufacturing files proposed here hold many advantages over the status quo—a de facto STL standard for 3D data which is disconnected from a myriad of open source and proprietary slice formats which are disconnected from the actual path plan used for part build up. Adoption of a single digital thread, in the form of AMF, AMSF, AMPF, AMQF and AMVF files, will enable designers, manufactures, modelers and end-users to have complete access to the variables and parameters they need to better understand and document AM processes and to enable well-informed decision making. The formats presented here are flexible and will continue to evolve to the needs of users are every level of the AM engineering process.

This work demonstrates the importance of having an ability to input processing and path-plan data, using a neutral format. The proposed AMSF and AMPF formats address this need. These file formats will enable users to easily compare the performance of different AM software and hardware systems. It will also reduce the time required to learn vendor-specific software. While operators must still have a thorough knowledge of the AM system's operational capabilities and limitations, they will not have to learn a specific machine code or reverse-engineer a vendor's software and hardware to customize processing parameters and path plans. In the opinion of the authors, empowering operators with the ability to simulate, tune and validate processing parameters to obtain desired microstructures, stresses, and properties is critical to the further development and adoption of AM technologies. Such "open" formats will also drive competition amount numerical simulation software developers and enable users to readily compare and contrast different AM simulation software.

A key challenge to the adoption of the strategy proposed here may be the reluctance of AM machine manufacturers to adopt a non-proprietary format for transmission and input of process parameter data. In fact, AM systems manufactures have been known to charge hefty prices simply to enable operators to modify and develop new processing parameters. Operators may also be charged for material-specific processing parameters, which may be considered proprietary by systems manufacturers. Data encryption, together with the proposed formats, can be used to safeguard this intellectual property while allowing end users to easily accesses processing data. Standards organizations can play an important role with respect to this challenge.

Also critical to the wide-spread adoption of AM technologies are the recording and transmission of sensor data. Recording and transmitting time-dependent sensor data, such as time and/or spatially-dependent deflection or temperatures, within an XML format can however be problematic [31]: the format and encoding of multimedia data associated with a sensor is designated by its manufacturer, or chosen by the end user, and cannot be reasonably expected to adhere to a single standard; data may require proprietary software or algorithms to interpret; the data size may be enormous, especially for video data; and, end users may only be interested in small subsets of the data. One solution is to point to the data along with a description of the data (metadata) within the AMQF file. In this sense, "virtual datasets" can be constructed without incurring the high costs of data reformatting and transfer [31].

Several standards already exist which aim to describe the meaning and format of stored data. Among these standards are Dublin Core Metadata Element Set (DCMES) [30], MPEG-7 [32] and METS [33]. In many cases however, these standards require detailed knowledge regarding their encoding schema. Since users of the AQMF file are likely more interested in accessing and understanding sensor data rather than details concerning the data encoding schemas, a simplified schema is being developed at the Applied Research Laboratory at Penn State, built partly on the DCMES vocabulary [30] and METS [33] standards.

After execution of the part buildup, verification and validation of part parameters and properties is often necessary. Verification and validation data will be recorded within an Additive Manufacturing Verification File (AMVF). A wide variety of Non-Destructive evaluation (NDE) as well as destructive evaluations techniques can be used to evaluate and verify the properties of a part. The techniques used are largely dependent on a part's intended application. Therefore, as with sensor data, it is envisioned that the locations and format of verification and validation data be specified within the AMVF file along with any information necessary for analysis. The format and contents of the AMVF are also under development at the Applied Research Laboratory at Penn State.

Ideally, all five files as well as any multimedia data, such as images or video should be stored within the same directory or folder. Filenames and descriptions of multimedia data will be included within the AMSF and AMVF files. Together, all five files will provide all the data necessary to reproduce, numerically model and validate a part produced using additive manufacturing process.

Acknowledgements

This work was supported by the Office of Naval Research , under Contract No. N00014-11-1-0668. Any opinions, findings and conclusions or recommendations expressed in this publication are those of the authors and do not necessarily reflect the views of the Office of Naval Research.

References

[1] I. Campbell, D. Bourell and I. Gibson, "Additive manufacturing: rapid prototyping comes of age," *Rapid Prototyping Journal,* vol. 18, no. 4, pp. 255-258, 2012.

[2] W. E. Frazier, "Direct digital manufacturing of metallic components: vision and roadmap," in *Twenty-First Solid Freeform Fabrication Symposium*, Austin, TX, 2010.

[3] K. Linebaugh, "GE Brings Engine Work Back," *The Wall Street Journal,* p. B2, 7 February 2013.

[4] National Center for Defense Manufacturing and Machining, "National Additive Manufacturing Innovation Institute," [Online]. Available: http://namii.org/. [Accessed 11 February 2013].

[5] P. A. Kobryn, N. R. Ontko, L. P. Perkins and J. S. Tiley, "Additive Manufacturing of

Aerospace Alloys for Aircraft Structures," AFRL/MLSC Acquisition Systems Support Branch Materials and Manufacturing Directorate Air Force Research Laboratory, Wright-Patterson Air Force Base, Ohio, 2006.

[6] Energetics Incorporated, "Roadmapping Workshop: Measurement Science for Metal-Based Additive Manufacturing," Gaitherburg, MD, 2012.

[7] ASTM International, "F2915-12 Standard Specification for Additive Manufacturing File Format (AMF) Version1.1," ASTM International, 2012.

[8] Society of Manufacturing Engineers, "Connecting the Digital Threads," *Manufacturing Engineering,* vol. 146, no. 6, pp. 33-36, 2011.

[9] M. Thone, S. Leuders, A. Riemer, T. Troster and H. A. Richard, "Influence of heat-treatment on selective laser melting products--e.g. Ti6Al4V," in *Twenty-Third Annual International Solid Freeform Fabrication (SFF) Symposium*, Austin, Texas, 2012.

[10] M. J. Wozny, "CAD and Interfaces," Rapid Prototyping Association of the Society of Manufacturing Engineering, Baltimore, Maryland, 1997.

[11] M. J. Pratt, "Introduction to ISO 10303 - the STEP Standard for Product Data Exchange," *Journal of Computing and Information Science in Engineering,* vol. 1, no. 1, pp. 102-103, 2001.

[12] A. L. Marsan, V. Kumar, D. Dutta and M. J. Pratt, "An assessment of data requirements and data transfer formats for layered manufacturing," U.S. Department of Commerce, 1998.

[13] C. K. Chua, K. F. Leong and C. S. Lim, Rapid Prototyping: Principles and Applications, World Scientific Publishing Co., 2010.

[14] M. Hardwick, "On STEP-NC and Complexities of Product Data Integration," *Transactions of the ASME,* vol. 4, no. 1, pp. 60-67, 2004.

[15] SCRA, "STEP Application Handbook ISO 10303 Version 3," North Charleston, SC, 2006.

[16] World Wide Web Consortium (W3C), "Extensible Markup Language (XML) 1.0 (Fifth Edition)," November 2008. [Online]. Available: http://www.w3.org/TR/xml/.

[17] "ASTM International News Releases," ASTM International, February 2009. [Online]. Available: http://www.astmnewsroom.org/default.aspx?pageid=1674. [Accessed January 2013].

[18] "Standardization News," ASTM International, November/December 2011. [Online]. Available: http://www.astm.org/standardization-news/outreach/astm-and-iso-sign-additive-manufacturing-psdo-agreement-nd11.html. [Accessed January 2013].

[19] S. M. Kelly, E. W. Reutzel and T. A. Palmer, "Impact of Path Planning on Thermal History during Direct Digital Deposition of Ti-6Al-4V," in *Materials Science & Technology 2012*, Pittsburg, PA, October 7-11, 2012.

[20] J. P. Kruth, M. Badrossamay, E. Yasa, J. Deckers, L. Thijs and J. V. Humbeeck, "Part and material properties in selective laser melting of metals," in *Proceedings of the 16th International Symposium on Electromachining (ISEM XVI)*, Shanghai, China, 2010.

[21] P. K. Venuvinod and W. Ma, Rapid Prototyping: Laser-based and Other Technologies, Norwell, Massachusetts: Kluwer Academic Publishers, 2004.

[22] A. Welisch, "COMMON LAYER INTERFACE (CLI) VERISON 2.0," [Online]. Available: http://www.forwiss.uni-passau.de/~welisch/papers/cli_format.html. [Accessed 14 February 2013].

[23] Hewlett-Packard Company, The HP-GL/2 Reference Guide - A Handbook for Program, Barcelona, Spain: Hewlett-Packard Company, 1996.

[24] International Organization for Standardization, ISO 6983-1:2009 Automation systems and integration -- Numerical control of machines -- Program format and definitions of address words -- Part 1: Data format for positioning, line motion and contouring control systems, 2009.

[25] ASTM International, "F2921-11e2 Standard Terminology for Additive Manufacturing—Coordinate Systems and Test Methodologies," ASTM International, 2011.

[26] American Welding Society, "AWS C7.4/C7.4M:2008 Process Specification and Operator Qualification for Laser Beam Welding," 2008.

[27] American Society of Mechanical Engineers, "2013 ASME Boiler and Pressure Vessel Code (BPVC), Section IX: Welding and Brazing Qualifications," 2013.

[28] American Welding Society, "AWS C7.3:1999R Process Specification for Electron Beam Welding," 1999.

[29] ASTM International, "F2924-12a Standard Specification for Additive Manufacturing Titanium-6 Aluminum-4 Vanadium with Powder Bed Fusion," ASTM International, 2012.

[30] Dublin Core Metadata Initiative, "Dublin Core Metadata Element Set, Version 1.1," 2012.

[31] R. E. McGrath, "XML and Scientific File Formats," The HDF Group, Champaign, IL , 2003.

[32] "MPEG-7," The Moving Picture Experts Group website, [Online]. Available: http://mpeg.chiariglione.org/standards/mpeg-7. [Accessed 02 2013].

[33] Digital Library Federation, "METS: Metadata Encoding and Transmission Standard Version 1.9.1," 2012.

Appendix 3 – A survey of sensing and control systems for machine and process monitoring of directed energy, metal-based additive manufacturing

Reutzel, E.W., Nassar, A.R., 2015. A survey of sensing and control systems for machine and process monitoring of directed-energy, metal-based additive manufacturing. Rapid Prototyping Journal 21, 159–167. doi:10.1108/RPJ-12-2014-0177

Downloaded by Pennsylvania State University, Doctor Edward Reutzel At 09:04 07 May 2015 (PT)

A survey of sensing and control systems for machine and process monitoring of directed-energy, metal-based additive manufacturing

Edward W. Reutzel and Abdalla R. Nassar
Applied Research Laboratory, Pennsylvania State University, University Park, Pennsylvania, USA

Abstract

Purpose – The purpose of this paper is to surveys classic and recently developed strategies for quality monitoring and real-time control of laser-based, directed-energy deposition. Additive manufacturing of metal parts is a complex undertaking. During deposition, many of the process variables that contribute to overall build quality – such as travel speed, feedstock flow pattern, energy distribution, gas pressure, etc. – are subject to perturbations from systematic fluctuations and random external disturbances.

Design/methodology/approach – Sensing and control of laser-based, directed-energy metal deposition is presented as an evolution of methods developed for welding and cladding processes. Methods are categorized as sensing and control of machine variables and sensing and control of build attributes. Within both categories, classic methods are presented and followed by a survey of novel developments.

Findings – Additive manufacturing would not be possible without highly automated, computer-based controllers for processing and motion. Its widespread adoption for metal components in critical applications will not occur without additional developments and integration of machine- and process-based sensing systems to enable documentation, and control of build characteristics and quality. Ongoing work in sensing and control brings us closer to this goal.

Originality/value – This work serves to introduce researchers new to the field of additive manufacturing to common sources of process defects during metal powder-based, directed-energy deposition processing, and surveys sensing and control methods being investigated to improve the process. The work also serves to highlight, and stress the significance of novel developments in the field.

Keywords Control systems, Layered manufacturing, Lasers, Metals, Material properties, Feedback control

Paper type General review

1. Introduction

Today's metals-based additive manufacturing (AM) processes can be considered an evolution of the welding and cladding processes that have been used for decades. As such, many of the strategies developed for sensing and control of welding and cladding have been or are being adapted for AM. Common examples include single-input, single-output (SISO) control of melt geometry or temperature through variation of laser power or travel speed to achieve a consistent weld. More recently, novel sensing and control approaches are being developed to cope with the additional challenges that AM processes bring, including multi-layer deposition with components or features that require complex build paths in each layer. A primary driver of many of these efforts is the need for rapid qualification and verification of low-volume production or specialized AM components. Here, we survey in-process sensing and control strategies for laser-based, directed-energy AM of metal components and highlight recent developments.

2. AM processes and subsystems

Fully dense metal parts can be built using AM processes in one of two categories:

1 directed-energy deposition; and
2 powder-bed fusion (ASTM F42 Committee, 2012).

The distinction lies in how material is introduced into the process. In directed-energy systems, powder or wire is fed into a molten pool atop a substrate. In powder-bed systems, a laser or electron beam is scanned over a bed of powder atop the substrate.

The current issue and full text archive of this journal is available on Emerald Insight at: **www.emeraldinsight.com/1355-2546.htm**

Rapid Prototyping Journal
21/2 (2015) 159–167
© Emerald Group Publishing Limited [ISSN 1355-2546]
[DOI 10.1108/RPJ-12-2014-0177]

The authors gratefully acknowledge the contributions by Mr Corey Dickman from the Applied Research Laboratory at the Pennsylvania State University. This work was supported in part by the Office of Naval Research, under Contract No. N00014-11-1-0668. Any opinions, findings and conclusions or recommendations expressed in this publication are those of the authors and do not necessarily reflect the views of the Office of Naval Research. This work was supported in part by the Air Force Research Laboratory through America Makes under agreement number FA8650-12-2-7230. The US Government is authorized to reproduce and distribute reprints for Governmental purposes notwithstanding any copyright notation thereon. The views and conclusions contained herein are those of the authors and should not be interpreted as necessarily representing the official policies or endorsements, either expressed or implied, of Air Force Research Laboratory or the US Government.

Received 10 December 2014
Revised 5 January 2015
Accepted 6 January 2015

Downloaded by Pennsylvania State University, Doctor Edward Reutzel At 09:04 07 May 2015 (PT)

Aside from how the feedstock material is introduced, both processes rely on similar subsystems, including:

- a laser or electron beam;
- a beam delivery system;
- motion controls;
- feedstock delivery system; and
- environmental controls.

The subsystems of both powder-blown and wire-fed directed-energy deposition processes, along with many of the potential observable or controllable variables, are shown in Figure 1.

There is potential to use both sensing and feedback control within each of these subsystems. Here, powder-blown, directed-energy AM is discussed. A high-level summary of some of the details of the process, from start to finish, is provided below to set the stage for subsequent sensor and control discussions.

A typical laser-based, directed-energy-deposition process begins with positioning of a substrate or build plate in the work space. As the laser beam optics and powder feed nozzles are designed to focus to a specific location, they will operate best at a predefined, optimal stand-off distance. Variations in the location of the substrate position caused by misalignment, overbuilding or in-process distortion will result in variations in powder feed alignment or energy density that can impact the process. Powder is typically fed through one or more coaxially aligned nozzles with assistance from a carrier gas. Variations in powder flow resulting from disturbance in chamber back pressure, powder clogs or other instabilities will impact the manner in which the laser beam interacts with the feedstock and can lead to melt pool fluctuations and process instability. The laser beam is then delivered to the interaction zone through a series of optics. Misalignment of the laser beam or contamination/damage to the beam delivery system will impact energy density at the surface, and can also produce fluctuations in the melt pool. The laser energy interacts with the powder and substrate, melting both. Some vaporization also occurs. Contamination of the powder or substrate can result in release of non-metal gaseous emissions that can result in porosity on solidification. Volatilizing contaminants or low vapor-pressure alloy-constituents can also lead to rapid expansion of gas, resulting in undesirable, and sometimes violent, expulsion of liquid metal and/or powder.

The beam–material interaction zone is translated in space relative to the substrate and previous depositions. If the volumetric energy transferred to the build is too low for a given initial substrate temperature, due to low laser power or high travel speed, then there is potential for lack of fusion, reduction in deposition volume, and/or reduction in depth of the fusion zone. This can result in a reduction of dilution or variation in build geometry (height, width and angle of repose), leading to detrimental misalignment in the subsequent deposits. If the volumetric energy is too high for a given substrate temperature, then puddle size will increase and overbuilding may occur, or increasing vaporization may lead to a keyholing effect and undesirable melt ejection from the vapor recoil force. As the melt pool solidifies, thermal gradients will lead to residual stresses that can result in substrate distortion. As the build proceeds, the energy that is deposited into the component may lead to a global temperature rise that can influence many of the factors above.

3. Sensing and control of machine variables

During normal operations, all AM systems must operate within known limits that are largely independent of the details of the process:

- the beam power and mode ought to be stable;
- motion stages and scanners should to be precise and accurate;
- material feed rate or powder layer thickness ought to be well-defined; and
- chamber pressure and gas concentrations ought to remain constant during processing.

To address this category of process parameters, process monitors and warning indicators, or independent, SISO control loops are typically used.

3.1 Laser beam delivery

The laser energy reaching the interaction zone can vary during normal operations due to electronic noise within the laser system, variations in beam front due to distortion and variation in the index of refraction resulting from thermal load

Figure 1 Subsystems of (a) laser-based powder-fed and (b) electron beam, wire-fed directed-energy deposition processes

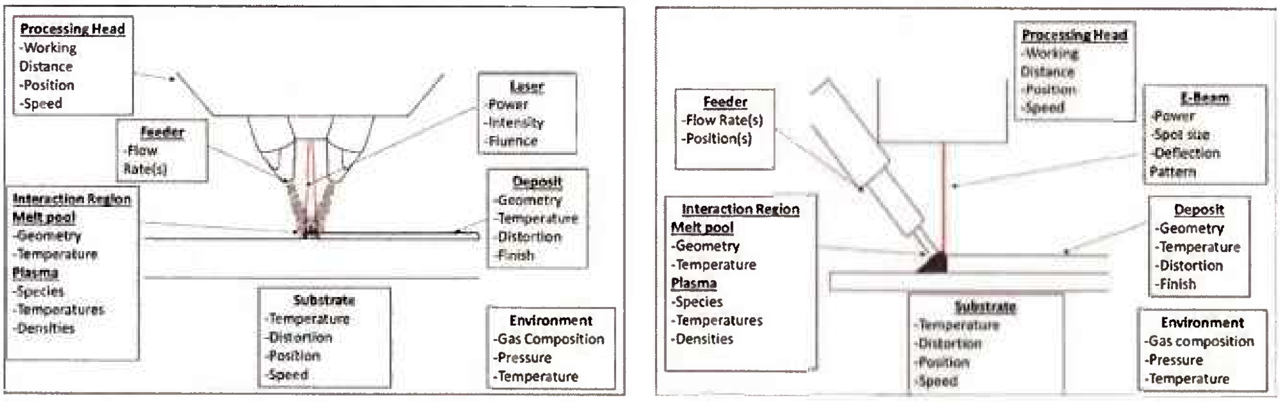
Processing Head
-Working Distance
-Position
-Speed
Feeder
-Flow Rate(s)
Laser
-Power
-Intensity
-Fluence
Interaction Region
Melt pool
-Geometry
-Temperature
Plasma
-Species
-Temperatures
-Densities
Deposit
-Geometry
-Temperature
-Distortion
-Finish
Substrate
-Temperature
-Distortion
-Position
-Speed
Environment
-Gas Composition
-Pressure
-Temperature
Feeder
-Flow Rate(s)
-Position(s)
Processing Head
-Working Distance
-Position
-Speed
E-Beam
-Power
-Spot size
-Deflection Pattern
Interaction Region
Melt pool
-Geometry
-Temperature
Plasma
-Species
-Temperatures
-Densities
Deposit
-Geometry
-Temperature
-Distortion
-Finish
Substrate
-Temperature
-Distortion
-Position
-Speed
Environment
-Gas composition
-Pressure
-Temperature

(a) (b)

Downloaded by Pennsylvania State University, Doctor Edward Reutzel At 09:04 07 May 2015 (PT)

on the optics, or damage to optical elements from process contaminants. Internal fluctuations in beam power can be reduced though closed-loop control of pump power (Paschotta, 2008). Systems based on monitoring reflections from turning mirrors (Johnstone, 2000) and from laser-induced Rayleigh scatter in air (Ophir Photonics, 2014) have potential to be used for non-intrusive, real-time measurement and assessment of both internal and external laser beam power fluctuations. Thermal load on the optical elements produces changes in lens geometry and index of refraction that lead to energy fluctuations at the substrate. These fluctuations are difficult to actively control, but are only an issue when operating at high laser powers, and effects can be reduced via active cooling.

Optical elements closest to the laser–substrate interaction zone are most vulnerable to be damaged from gaseous process emissions and melt spatter, and are thus most likely to distort or attenuate the laser beam. If contamination is severe, processing with a high-power laser can induce thermal stresses within the lens that result in cracking, as shown in Figure 2. In directed-energy laser deposition systems, a focusing lens, together with a protective cover lens, are enclosed within a processing head. Various researchers (Bi *et al.*, 2007; Tönshoff *et al.*, 2003) have shown that monitoring of the reflected laser light from the protective glass using a photodiode can be used to sense damage to the protective cover lens. Additionally, they show that monitoring temperatures within the cladding head can also be used for real-time assessment of the condition of the optics. A schematic of the optics monitoring setup used by Bi *et al.* (2007) is shown in Figure 3.

3.2 Chamber environment

Monitoring of key conditions within the processing environment is straightforward. For laser-based processes, the processing chamber is filled and recirculated with argon, nitrogen or other inert gases, depending on the material being deposited, to limit contamination through oxidation or other source. To ensure part quality, oxygen concentration within the build environment is typically monitored using a trace oxygen sensor. Electrochemical oxygen sensors can measure concentrations down to parts per million, but require periodic calibration because exposure to oxygen that occurs during normal operations reduces sensor lifetime.

Figure 2 Extreme case of optics damage during high-power laser processing

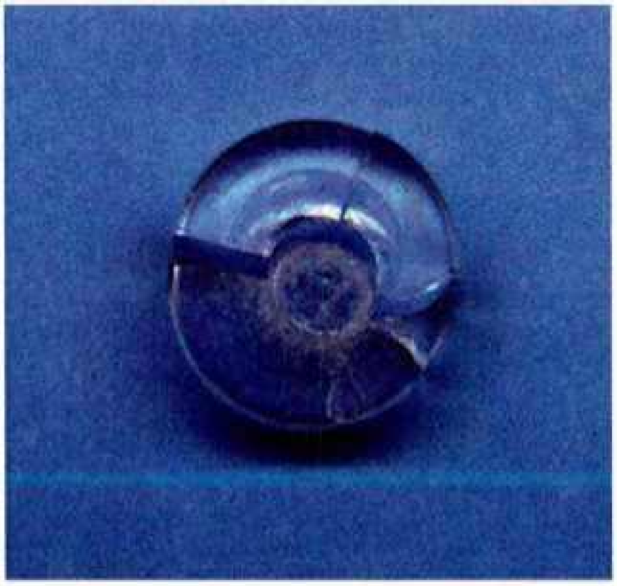

Figure 3 Schematic of an optics system utilized to monitor contamination of beam delivery optics

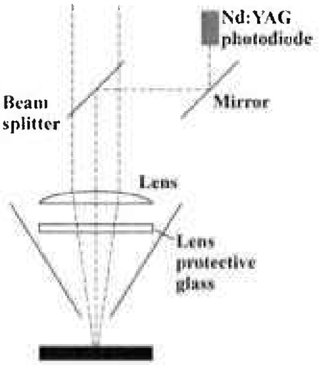

Source: Adapted from Bi *et al.* (2007)

Chamber pressure fluctuations have been observed to influence the feed rate of powder and the flow rate of processing gas in powder-blown systems. AM processes are also vulnerable to contamination from outgassing of polymers or vaporization of water or other volatile compounds.

3.3 Feedstock delivery

To achieve consistent quality, powder-blown and wire-fed directed-energy deposition systems require a well-defined volume or mass of material feedstock to be introduced at the proper rate to the correct location. In both the powder-blown and wire-fed processes, the angle, location (with respect to the beam), velocity and/or mass flow rate at which the material is fed, (as well as the powder feedstock and flow stream morphology for powder-blown systems), all affect the deposition process. A study of the impact of powder, carrier gas and nozzle characteristics on powder flow was performed by Balu *et al.* (2012) to maximize powder concentration at the substrate working distance. Various researchers have demonstrated ways to monitor, and in some cases, control feedstock properties to ensure quality depositions.

In powder-blown systems, powder delivery and flow characteristics must remain consistent if consistent quality is to be achieved. From a practical standpoint, nozzles can clog or suffer damage during operations. Examples of a clogged and damaged nozzles are shown in Figure 4.

To provide real-time monitoring of perturbations of powder flow resulting from damaged or clogged nozzles, imaging methods to assess flow at the processing head have been developed. One example of such a system, developed by Nassar and Reutzel (2014), uses a filtered camera to view the light from a laser line generator that is reflected off powder exiting the nozzles during the deposition process. Figure 5 illustrates this method, and shows the resultant images prior to

Downloaded by Pennsylvania State University, Doctor Edward Reutzel At 09:04 07 May 2015 (PT)

Figure 4 Example of nozzles that were (a) damaged, and (b) clogged during AM processes

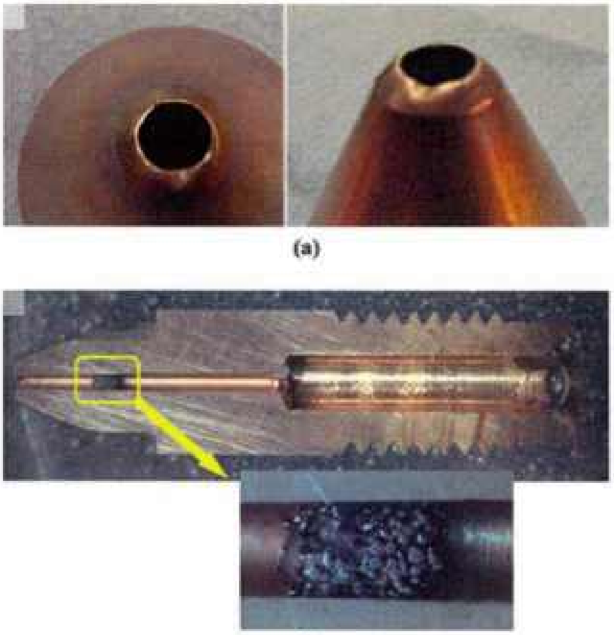
(a)
(b)

analysis. Automated identification of clogged or damaged nozzles can be important for quality control during long builds.

In powder-blown systems, real-time monitoring and control of feed rate is most often achieved using continuous weight measurements. Due to slow sampling rates found in typical commercial weigh-based measurement systems, there is a significant time delay between changes in set point and a stable powder flow. This is especially problematic when more than one powder feeder is used to produce alloys or functionally graded materials. Hu and Kovacevic (2003) developed a diode-based sensor that measures the attenuation of a laser beam, as it is transmitted through a glass tube connected to the powder feeder. The setup is illustrated in Figure 6.

An additional delay results from the fact that, in many commercial systems, the processing laser head is located away from the powder feeder, resulting in a substantial lag between changes in set point and observable changes in feed rate at the beam–material interaction zone. This delay time depends on the length of the tubes connecting the feeder to the deposition head coupled with the material feed rate.

To account for this and other delays in powder flow, Muller *et al.* (2013) developed a model of powder flow rate at the deposition head as a function of the input signal to the powder feeder. They then coupled the model to a closed-loop predictive control system, enabling them to generate an numerical control (NC) program that compensates for delays to deposit functionally graded materials with the desired composition.

Figure 5 Illustration of method to assess powder flow from individual nozzles

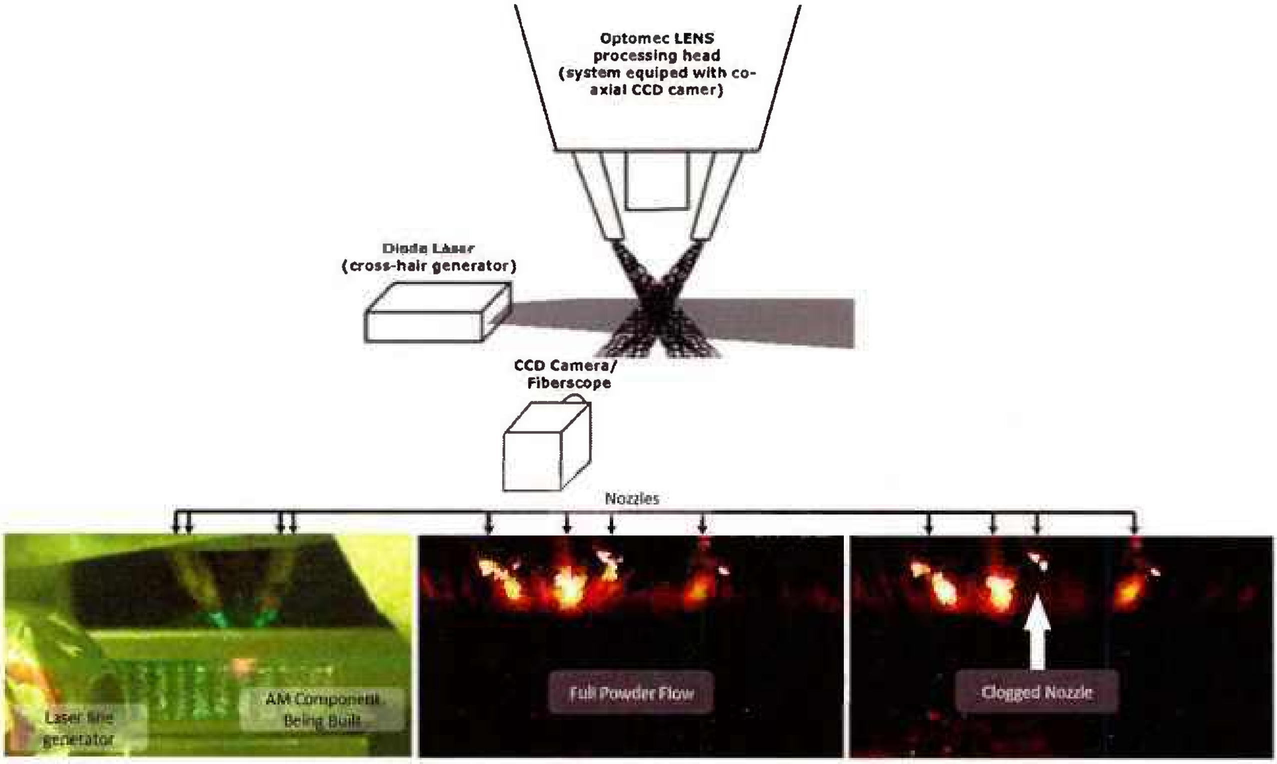
Optomec LENS processing head (system equiped with co-axial CCD camer)
Diode Laser (cross-hair generator)
CCD Camera/ Fiberscope
Nozzles
Laser line generator
AM Component Being Built
Full Powder Flow
Clogged Nozzle

Figure 6 Illustration of the Hu and Kovacevic powder feed rate controller

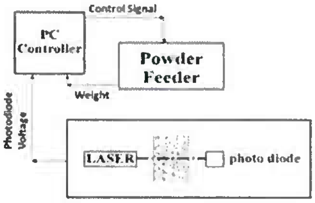

Source: Adapted from Hu and Kovacevic (2003)

While it is difficult to precisely control the material feed rate in powder-blown processes, it is relatively easy to do so in wire-feed processes. Commercial wire feeders have long existed for the welding industry and can be readily integrated into AM machines. They handle a wide range of wire sizes and typically allow real-time control of feed rate based on an analog voltage or current. One possible source of noise during wire feed operations is slipping of the wire relative to the feed rolls, but this can usually be corrected by reducing the feedlength, eliminating sharp bends in the wire conduit, and by properly adjusting the roller pinching force.

4. Sensing and control of build attributes

Although sensing and control of process-independent machine variables can be realized largely without concern for the specifics of the process, process-dependent build attributes require some knowledge of the desired part geometry, material composition, density, microstructure and other properties. Many of these characteristics cannot be directly measured, e.g. material composition, density and microstructure. However, certain characteristics of the beam–material interaction, as well as solidified regions of the deposit, can be monitored to allow estimation of these variables. For example, it has been argued that characteristics of the melt pool geometry can be used to predict deposited microstructures in Ti-6Al-4V (Bontha *et al.*, 2006) and Inconel 718 (Thompson, 2014).

4.1 Melt pool geometry

As noted earlier, melt pool geometry is influenced by a wide variety of process conditions. As it is straightforward to introduce coaxial imaging systems to a laser deposition system, the melt pool is an attractive characteristic of the process used for monitoring and as control. The impact on melt pool due to changes in build geometry, laser power, initial temperature, alignment to adjacent depositions, and many other factors, is illustrated by observing the variation in coaxial thermal melt pool images collected throughout deposition of a single layer of a relatively simply build (Figure 7). Note that the melt pool width increases in a regular fashion as the build proceeds along the first leg, but varies significantly once it enters the three-bead wide portion of the build. In the past two decades, many researchers have utilized coaxial melt pool imaging to monitor and control the process.

In some of the earliest work in process control related to laser- and powder-based, directed-energy-deposition systems, Hofmeister *et al.* (1999) used a visible light pyrometry technique to determine melt pool characteristics. They noted that the heat sink conditions at each phase of the deposition varied appreciably during a complex build, and this had a profound impact on the melt pool size. Images collected with a coxial, filtered high-speed video camera were converted to temperature to calculated the melt pool area. This melt pool area was used as input to a proportional–integral–derivative (PID) controller, which varied in laser power to maintain a constant melt pool area. The controller took in consideration

Figure 7 Coaxial thermal images of melt pool collected during a laser-based directed-energy deposition using powder feedstock without feedback control. The yellow portion of the image highlights the liquidus-to-solidus region

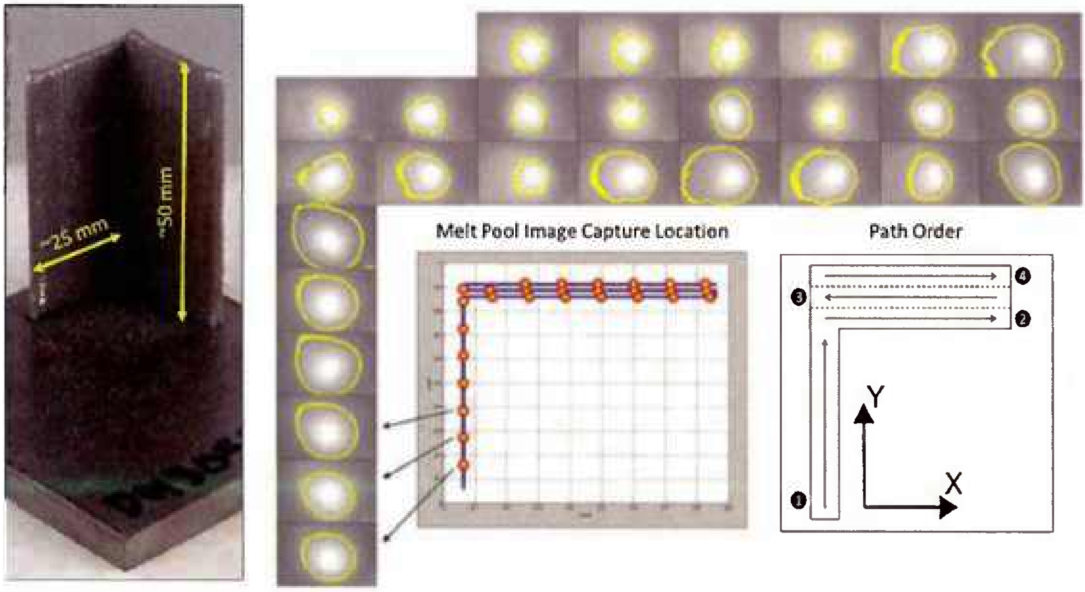

Downloaded by Pennsylvania State University, Doctor Edward Reutzel At 09:04 07 May 2015 (PT)

Downloaded by Pennsylvania State University, Doctor Edward Reutzel At 09:04 07 May 2015 (PT)

whether a boundary (contour) or fill pass (hatch) was being made. They demonstrated improvement in consistency of build dimensions with the controller.

Several years later, Hu and Kovacevic (2003) utilized coaxial single-color infrared (IR) imaging to demonstrate that, for a select group of processing conditions, the melt pool width and area could be correlated to the fusion zone depth and average melt pool temperature. Later, Colodron *et al.* (2011) showed that melt pool width also correlated closely to dilution and used an field-programmable gate array (FPGA)-based controller to vary laser power to control melt pool width based on measurement with a 50 fps, coaxial complementary metal–oxide–semiconductor (CMOS) camera. Their colleagues followed up a year later (Araujo *et al.*, 2012) with enhancements to compensate for noise in the images resulting from powder, optics contamination and other effects. The same year, Hofman *et al.* (2012) also demonstrated that varying laser power with a melt pool width controller was also effective in maintaining consistent microhardness in the face of substantial local changes in heat sink from geometry effects.

4.2 Melt pool temperature

Melt pool temperature is another characteristic that is impacted by many process variations and that influences final build attributes. In contrast to performing complex data analysis on noisy images, average melt pool temperature can be readily measured using low-cost photodiodes or other sensors. Bi *et al.* (2007, 2006) recognized the potential benefits of such a sensor, and showed that a suitable photodiode could be easily integrated into a processing head to provide a coaxial measurement, could identify anomalous build characteristics and could be correlated to dilution. They also demonstrated melt pool temperature control by varying laser power. More recently, Bi *et al.* (2013) confirmed that part geometry has a strong influence on melt pool temperature, and investigated the use of changing the energy density by means of laser defocusing to compensate. They found that controllability with these techniques was limited before low irradiance significantly degraded deposition quality. This study also revealed that oxidation during processing changes the spectral emissions and may result in false readings using this technique. Song and Mazumder (2011) demonstrated melt pool temperature control using measurements from a dual-color pyrometer by varying laser power using a controller based on an experimentally identified state space model of laser power-to-melt pool dynamics.

4.3 Deposition height

An important challenge during AM is achieving consistent material characteristics and geometry. In particular, build height is strongly influenced by distortion and changes in powder capture efficiency. Optical sensors are most often used for non-intrusive measurements of build height. The chromatic–aberration-based technique developed by Hand *et al.* (2000) detects the ultraviolet and IR components of the continuum radiation generated during processing. Taking advantage of variations in intensity of each spectral range with working distance, due to chromatic distortions, they designed a height control system and coupled it with a laser-power controller based on pyrometer measurements of melt pool temperature.

Fathi *et al.* (2006) utilized a more conventional, charge-coupled device (CCD) imaging sensors to assess the influence of various process conditions on deposition height, and then utilized system identification techniques to determine a dynamic system model. With this, they were able to construct PID controllers both with and without an additional feedforward term (based on the identified system dynamics). They varied travel speed to control build height and found that inclusion of the feedforward term resulted in responses more closely following the desired set point. More recently, Fathi teamed with Mozaffari *et al.* (2013) to develop advanced system identification techniques to develop neural network and other models of the highly non-linear deposition process. This enabled them to develop a multi-input multi-output controller capable of performing multi-objective optimization. In this case, they were able to demonstrate optimization of both clad height and dilution by varying travel speed, laser power and powder flow rate.

Song *et al.* (2011) developed a two-input, single-output hybrid control system that used a master height controller and slave temperature controller. The height was measured with three high-speed CCD cameras, and the temperature was measured with a two-color pyrometer. When the melt pool height exceeded a prescribed value, the temperature controller was blocked and laser power was reduced to limit build height. When melt pool height was within the specified range, the laser power was varied to control melt pool temperature. They found that this hybrid approach provided stable builds.

4.4 Optical emissions

During processing, the laser beam heats up the powder and the substrate material to an elevated temperature, leading to melting and vaporization. Bartkowiak (2010) demonstrated that the optical emissions and spectral lines that can be collected from the vapor emissions generated during low-power (< 2 kW laser) deposition are related to the temperature and composition of the melt pool. Song and Mazumder (2012) also demonstrated an ability to monitor chromium composition in real time during deposition of H13 tool steel. After proper calibration, they were able to predict chromium composition to within 2.8 per cent atomic weight. Nassar *et al.* (2014a) evaluated spectra from optical emissions during a build designed to have intentional lack-of-fusion defects. Their analysis suggests that optical emissions may contain information that can be related to build defects.

4.5 Path control

Process controller development efforts to date have targeted real-time control of one or more build attributes based on the specific characteristics of the process that are possible to sense, coupled with the process parameters that are available to vary. They promise to improve build consistency that is currently degraded by systematic process variations that are not compensated with traditional, purely feedforward processing. However, they all operate independent of the processing path, and do not allow variation in the path that may help to decrease thermal build-up or distortion. Additionally, they do not provide means to correct the inevitable intermittent

Downloaded by Pennsylvania State University, Doctor Edward Reutzel At 09:04 07 May 2015 (PT)

defects that will occur in production. In contrast to a casting of forging, the layerwise nature of the AM process allows machine access to the interior of the component as it is being built, offering opportunity to correct certain types of defects.

A system architecture has been developed and integrated into a commercial AM system that allows real-time adjustment of the build plan during each layer. The data flow utilized in the architecture is illustrated in Figure 8. To test and demonstrate the architecture, a test case was defined in which the build plan (specifically, the hatch pattern) was modified in real time based on a temperature reading. Prior to executing a given hatch, a pyrometer was used to interrogate the temperature of the substrate. If the substrate temperature exceeded an arbitrary set point, then the hatch was skipped until later, and the next programmed hatch was processed with the same algorithm. After all acceptable hatches were processed, the hatches that had been previously skipped were processed. Figure 9 illustrates the impact of the controller activity on the hatching order. Evaluation of cross-sections has revealed that the closed-loop controller produces a build with less variation in microstructure than an uncontrolled deposition (Nassar *et al.*, 2014b).

5. Conclusions

Without the development of highly automated computer-based controllers for processing and motion, modern AM would not be possible. These systems lend

Figure 8 System architecture to enable real-time path modification and control

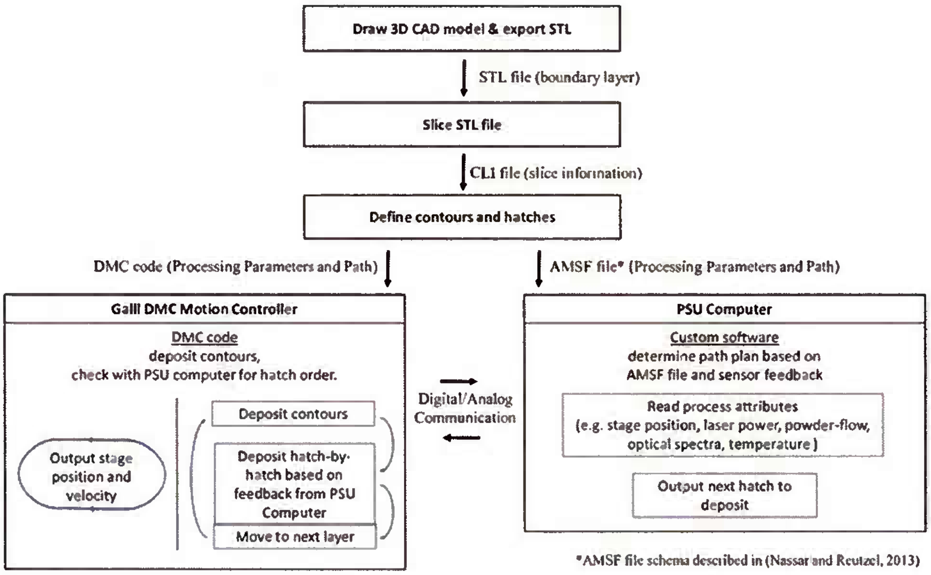
Draw 3D CAD model & export STL
STL file (boundary layer)
Slice STL file
CLI file (slice information)
Define contours and hatches
DMC code (Processing Parameters and Path)
AMSF file* (Processing Parameters and Path)
Galil DMC Motion Controller
DMC code
deposit contours,
check with PSU computer for hatch order.
Output stage position and velocity
Deposit contours
Deposit hatch-by-hatch based on feedback from PSU Computer
Move to next layer
Digital/Analog Communication
PSU Computer
Custom software
determine path plan based on AMSF file and sensor feedback
Read process attributes
(e.g. stage position, laser power, powder-flow, optical spectra, temperature)
Output next hatch to deposit
*AMSF file schema described in (Nassar and Reutzel, 2013)

Figure 9 Illustration of changing controller activity in changing hatch order during a build

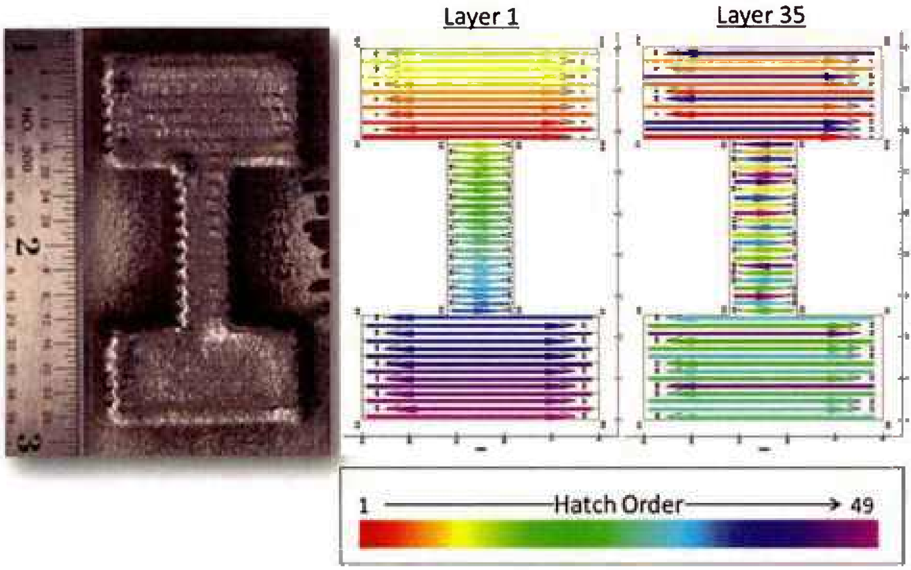

Downloaded by Pennsylvania State University, Doctor Edward Reutzel At 09:04 07 May 2015 (PT)

themselves to continuing development and integration of machine- and process-based sensing systems that improve process documentation, and enable control of build characteristics and quality. Such developments are essential for qualification activities and to garner widespread acceptance by the technical community. The research community has made numerous advancements in sensor and control technologies that bolster these efforts.

In recent years, researches have developed sensors for monitoring of the laser beam and delivery optics, chamber pressure and oxygen concentration, powder and wire feed rates, melt pool temperature and dynamics, optical emissions and substrate temperature. A subset of these efforts have been highlighted here along with recent developments toward in-process, path plan modification. To achieve the goal of rapid qualification of AM parts, further progress and commercialization of sensors and controls must continue.

References

Araujo, J.R., Rodriguez-Andina, J.J., Farina, J., Vidal, F., Mato, J.L. and Montealegre, M.A. (2012), "FPGA-based laser cladding system with increased robustness to optical defects", *IECON 2012-38th Annual Conference on IEEE Industrial Electronics Society, Montreal, QC*, pp. 4688-4693.

ASTM F42 Committee (2012), *Terminology for Additive Manufacturing Technologies*, ASTM International, West Conshohocken, PA.

Balu, P., Leggett, P. and Kovacevic, R. (2012), "Parametric study on a coaxial multi-material powder flow in laser-based powder deposition process", *Journal of Materials Processing Technology*, Vol. 212 No. 7, pp. 1598-1610.

Bartkowiak, K. (2010), "Direct laser deposition process within spectrographic analysis in situ", *Physics Procedia*, Vol. 5 Part B, pp. 623-629.

Bi, G., Gasser, A., Wissenbach, K., Drenker, A. and Poprawe, R. (2006), "Identification and qualification of temperature signal for monitoring and control in laser cladding", *Optics and Lasers in Engineering*, Vol. 44 No. 12, pp. 1348-1359.

Bi, G., Schürmann, B., Gasser, A., Wissenbach, K. and Poprawe, R. (2007), "Development and qualification of a novel laser-cladding head with integrated sensors", *International Journal of Machine Tools and Manufacture*, Vol. 47 Nos 3/4, pp. 555-561.

Bi, G., Sun, C.N. and Gasser, A. (2013), "Study on influential factors for process monitoring and control in laser aided additive manufacturing", *Journal of Materials Processing Technology*, Vol. 213 No. 3, pp. 463-468.

Bontha, S., Klingbeil, N.W., Kobryn, P.A. and Fraser, H.L. (2006), "Thermal process maps for predicting solidification microstructure in laser fabrication of thin-wall structures", *Journal of Materials Processing Technology*, Vol. 178 Nos 1/3, pp. 135-142.

Colodron, P., Fariña, J., Rodríguez-Andina, J.J., Vidal, F., Mato, J.L. and Montealegre, M.A. (2011), "Performance improvement of a laser cladding system through FPGA-based control", *IECON 2011-37th Annual Conference on IEEE Industrial Electronics Society, Melbourne, VIC*, pp. 2814-2819.

Fathi, A., Khajepour, A., Toyserkani, E. and Durali, M. (2006), "Clad height control in laser solid freeform fabrication using a feedforward PID controller", *The International Journal of Advanced Manufacturing Technology*, Vol. 35 Nos 3/4, pp. 280-292.

Hand, D.P., Fox, M.D.T., Haran, F.M., Peters, C., Morgan, S.A., McLean, M.A., Steen, W.M. and Jones, J.D.C. (2000), "Optical focus control system for laser welding and direct casting", *Optics and Lasers in Engineering*, Vol. 34 Nos 4/6, pp. 415-427.

Hofman, J.T., Pathiraj, B., van Dijk, J., de Lange, D.F. and Meijer, J. (2012), "A camera based feedback control strategy for the laser cladding process", *Journal of Materials Processing Technology*, Vol. 212 No. 11, pp. 2455-2462.

Hofmeister, W.H., MacCallum, D.O. and Knorovsky, G.A. (1999), "Video monitoring and control of the lens process", presented at the American Welding Society 9th International Conference of Computer Technology in Welding, *Detroit, MI*.

Hu, D. and Kovacevic, R. (2003), "Sensing, modeling and control for laser-based additive manufacturing", *International Journal of Machine Tools and Manufacture*, Vol. 43 No. 1, pp. 51-60.

Johnstone, I. (2000), "Beam sampling and process monitoring in laser material processing applications", *Industrial laser Solutions*, Vol. 20, pp. 34-35, available at: http://mbdaps.com/precision-optical/data/ta004.htm, (accessed February 20, 2015).

Mozaffari, A., Fathi, A., Khajepour, A. and Toyserkani, E. (2013), "Optimal design of laser solid freeform fabrication system and real-time prediction of melt pool geometry using intelligent evolutionary algorithms", *Applied Soft Computing*, Vol. 13 No. 3, pp. 1505-1519.

Muller, P., Mognol, P. and Hascoet, J.Y. (2013), "Modeling and control of a direct laser powder deposition process for Functionally Graded Materials (FGM) parts manufacturing", *Journal of Materials Processing Technology*, Vol. 213 No. 5, pp. 685-692.

Nassar, A.R. and Reutzel, E.W. (2014), "Real-time sening of powder flow during directed-energy deposition (In Preparation)".

Nassar, A.R., Spurgeon, T.J. and Reutzel, E.W. (2014a), "Sensing defects during directed-energy additive manufacturing of metal parts using optical emissions spectroscopy", *Solid Freeform Fabrication Symposium Proceedings*, University of Texas, Austin, TX.

Nassar, A.R., Spurgeon, T.J. and Reutzel, E.W. (2014b), "Intra-Layer Control via Alteration of Path Plan in Directed Energy Deposition (Submitted)", available at: www.journals.elsevier.com/additive-manufacturing/.

Ophir Photonics (2014), *Ophir Photonics'BeamWatch^{TM}, Industry's First Non-Contact Industrial Beam Monitoring System for Very High PowerYAG and FiberLasers*, available at: www.ophiropt.com/user_files/laser/press-release/OSI_BeamWatch_PR.pdf (accessed July 2, 2014).

Paschotta, R. (2008), "Laser noise", *Field Guide to Lasers*, Bellingham, WA, pp. 116-120.

Song, L., Bagavath-Singh, V., Dutta, B. and Mazumder, J. (2011), "Control of melt pool temperature and deposition height during direct metal deposition process", *The*

International Journal of Advanced Manufacturing Technology, Vol. 58 Nos 1/4, pp. 247-256.

Song, L. and Mazumder, J. (2011), "Feedback control of melt pool temperature during laser cladding process", *IEEE Transactions on Control Systems Technology*, Vol. 19 No. 6, pp. 1349-1356.

Song, L. and Mazumder, J. (2012), "Real Time Cr Measurement Using Optical Emission Spectroscopy During Direct Metal Deposition Process", *IEEE Sensors Journal*, Vol. 12 No. 5, pp. 958-964.

Thompson, J.R. (2014), *Relating Microstructure to Process Variables In Beam-Based Additive Manufacturing of Inconel 718 (Master Of Engineering)*, Wright State University, Dayton, Ohio.

Tönshoff, H.K., Ostendorf, A. and Kral, V. (2003), "Condition monitoring of laser systems: monitoring the cover slide", *Journal of Laser Application*, Vol. 15 No. 1, pp. 62-66.

Downloaded by Pennsylvania State University, Doctor Edward Reutzel At 09:04 07 May 2015 (PT)

About the authors

Edward W. Reutzel has been involved in arc- and laser-based material processing since 1993, historically with emphasis on macro-scale processing of metals, but more recently with emphasis on laser-based additive manufacturing technology. He has served as Chair for sessions at the International Congress on Laser and Electro Optics, and served as Chair of the Laser Material Processing for Solar Energy Conference at the SPIE Optics + Photonics event from 2012 to 2014. He has managed numerous programs to investigate laser material processing techniques covering a wide range of applications, has authored and co-authored book chapters, has provided invited articles and invited talks internationally. He has advised and co-advised numerous graduate students, and teaches a graduate-level laser processing laboratory course in Penn State's Graduate-Level Certificate Program in Laser Material Processing. Dr Reutzel currently manages ARL Penn State's Laser Processing Laboratory and is an Associate of Penn State's Center for Innovative Material Processing through Direct Digital Deposition.

Abdalla R. Nassar has accumulated experience in fields related to acquisition and control systems, numerical modeling and metallographic analysis, with an emphasis on laser-materials processing. At the Applied Research Laboratory at Penn State, Dr Nassar has developed software and algorithms related to direct integration of additive manufacturing processes with computational modeling, data acquisition and control of additive manufacturing equipment and defect–detection strategies. He earned his BS and PhD. in Engineering Science from the Pennsylvania State University in 2008 and 2012, respectively. He has co-authored publications on the digital thread concept for AM, sensing and control of AM processes, linking thermal sensors, modeling and AM machine behavior, laser-plasma nitriding of titanium, characterization of plasma via optical emission spectroscopy and numerical modeling of laser-sustained plasma. Abdalla R. Nassar is the corresponding author and can be contacted at: arn5000@psu.edu

For instructions on how to order reprints of this article, please visit our website:
www.emeraldgrouppublishing.com/licensing/reprints.htm
Or contact us for further details: **permissions@emeraldinsight.com**

Appendix 4 – Intra-layer closed-loop control of build plan during directed energy additive manufacturing of Ti–6Al–4V

Nassar A R, Keist J S , Reutzel E W, Spurgeon T J, Intra-layer closed-loop control of build plan during directed energy additive manufacturing of Ti–6Al–4V. *Additive Manufacturing,* 6, 39–52. doi:10.1016/j.addma.2015.03.005, 2015.

ELSEVIER

Available online at www.sciencedirect.com

ScienceDirect

Additive Manufacturing 6 (2015) 39–52

Additive
MANUFACTURING

www.elsevier.com/locate/addma

Intra-layer closed-loop control of build plan during directed energy additive manufacturing of Ti–6Al–4V

Abdalla R. Nassar*, Jayme S. Keist[1], Edward W. Reutzel[2], Todd J. Spurgeon

Applied Research Laboratory, The Pennsylvania State University, University Park, PA 16804, USA

Accepted 17 March 2015

Available online 25 March 2015

Abstract

The location, timing, and arrangement of depositions paths used to build an additively manufactured component – collectively called the build plan – are known to impact local thermal history, microstructure, thermal distortion, and mechanical properties. In this work, a novel system architecture for intra-layer, closed-loop control of the build plan is introduced and demonstrated for directed-energy deposition of Ti–6Al–4V. The control strategy altered the build plan in real time to ensure that the temperature around the start point of each hatch, prior to deposition, was below a threshold temperature of 415 °C. Potential hatches with an initial temperature above this threshold were temporarily skipped. Compared with open-loop processing, closed-loop control resulted in vertical alignment of columnar prior-β grains, more uniform α-lath widths, and more-uniform microhardness values within the deposited component.

© 2015 Elsevier B.V. All rights reserved.

Keywords: Additive manufacturing; Directed energy deposition; Control; Ti–6Al–4V; Lath width; Hardness

1. Introduction

Additive Manufacturing (AM) of metal-based components has recently garnered increasing attention. This interest is motivated by the potential to inexpensively and rapidly produce or repair high-value, complex parts. The novel capabilities offered by AM, however, come at an expense. Manufacturing of even simple components via AM is complex, typically requiring hundreds or thousands of individual laser or electron-beam depositions. The ordering, timing, and placement of depositions, also known as a hatch plan, path plan, or build plan, define a part's thermal history throughout the build. As is discussed in Section 1.1, this affects part microstructure, residual stresses, distortion, and mechanical properties.

1.1. Influence of build plan on microstructure and properties

Previous researchers have investigated the effects of build plan on microstructure and properties primarily using one of the two strategies. Following the first strategy, changes in microstructure and properties as a result of changing build orientation are investigated. Due to the greater flexibility in depositing overhangs, this approach is typically limited to powder-bed fusion (PBF) processes. Following the second approach, investigators examine the effects of location, order and timing of deposition paths on microstructure and mechanical properties.

To assess the effect of part orientation – and hence the build plan – researchers have built geometrically simple parts, such as cylindrical or flat tensile specimens, with their major axis oriented at various angles with respect to the build-up (z-axis) direction [1–3]. For example, Tolosa et al. [3] used a laser-based, BPF process to deposit flat AISI 316L stainless steel tensile and Charpy impact test specimens oriented at angles of 0°, 45°, 60°, and 90° with respect to the build-up direction. Additionally, the

---

* Corresponding author. Tel.: +1 814 863 9409; fax: +1 814 863 1183.
E-mail addresses: arn5000@psu.edu (A.R. Nassar), jsk25@psu.edu (J.S. Keist), ewr101@arl.psu.edu (E.W. Reutzel), tjs@vt.edu (T.J. Spurgeon).

[1] Tel.: +1 814 867 4785.

[2] Tel.: +1 814 863 9891.

http://dx.doi.org/10.1016/j.addma.2015.03.005

2214-8604/© 2015 Elsevier B.V. All rights reserved.

orientation of the flat-edge of the tensile samples and the rotation angle on the build plate were investigated. Differences in tensile strength, yield strength, and elongation percent were observed; however, explanations for this were not provided. Samples oriented parallel to the build-up direction exhibited the largest values for elongation percentage, while samples oriented perpendicular to the build-up direction, with the flat edge of the tensile sample laying on the build plate, exhibited largest values for yield and ultimate strength.

Similar patterns have been observed during electron beam PBF of Ti–6Al–4V using the Arcam EBM® process: tensile specimens showed larger elongation percentage for orientations parallel to the build-up direction and higher yield and ultimate strength when oriented perpendicular to the build-up direction [1,2]. Rafi et al. suggested that such differences might be due to defects along planes perpendicular to the build-up direction, inter-granular discontinuities, or differences in α-lath widths. The pattern observed by Tolsoa et al., Rafi et al., and Brandl et al. is, however, contradicted by the observations of Hrabe and Quinn [4]; they reported a higher elongation percentage and lower strength for Ti–6Al–4V samples deposited perpendicular to the build-up direction using the Arcam EBM® process. Though the results were attributed to the texture and elongation of the prior-β grains and reference was made to a previous study drawing similar conclusions [5], why results differed from studies [1,2], which employed similar AM technologies and analysis techniques, is unclear.

It is also unclear how mechanical properties such as indentation hardness are affected by orientation. On the one hand, Tolosa et al. [3] have suggested that hardness profiles of AM parts built using laser-based PBF are uniform and have mechanical properties comparable to wrought components irrespective of orientation. On the other hand, Roy [6] reported higher nanoindentation hardness values for electron-beam-PBF-deposited, Ti–6Al–4V tensile samples oriented perpendicular to the build-up direction than those oriented parallel to it.

Despite lack of a clear explanation for how part orientation in powder-bed systems impacts properties, its impact on microstructure is better understood. In Ti–6Al–4V, the ⟨0 0 1⟩ direction of β grains preferentially aligns parallel to the maximum thermal gradient [7,8]. Altering a part's build plan or part dimensions has been shown to alter prior-β grain orientation in Ti–6Al–4V [8]. Alternating layer-to-layer scan direction during selective laser melting has also been shown to result in a "herringbone pattern" [9,10].

Similar effects were found using directed-energy depositions (DED) of Ti–6Al–4V. Using a tungsten inert east (TIG) welding system, Baufeld [11] showed that prior-β grains were slanted along the temperature gradient. This was previously observed with laser-based, DED processes [12]. The effect of build plan on microstructure has also been observed in other alloy systems. For instance, for powder-feed DED of Inconel 625, Dinda et al. [13] showed that alternating layer-to-layer scan direction rotated the growth direction of columnar dendrites by 90° from layer-to-layer. Though build plan impacts microstructure, properties and thermal stress, the authors are unaware of any efforts toward closed-loop control of build plan.

1.2. Control of AM

Much work on closed-loop control of AM processes has been performed. Most researchers focus on real-time control of the deposition process by varying the laser power or processing speed based on sensing of the melt pool size [14–18] or temperature [19,20]. Some have also attempted to maintain a constant working distance, or layer build height, by sensing the build height and adjusting the processing head position [21], the processing speed [22,23], the filler material feed rate [24] or the laser power [25]. Another target of closed-loop control efforts is varying powder or wire-feed rates to control material composition for functionally graded materials deposition [26,27]. For reviews of in-process monitoring and control for AM, see [28–31].

Here, we depart from efforts using real-time control of one or multiple variables and instead investigate closed-loop control of the build plan during directed-energy AM. A system architecture was developed to enable intra-layer build-plan modification, based on measurement of the local, initial temperature of each potential deposition path, also referred to as hatch, on a layer. We found that closed-loop control of the order and timing of hatches, based on their initial temperature, affected the microstructure and properties of deposited parts. Closed-loop control resulted in vertical alignment of columnar prior-β grains, more uniform α-lath widths, and more-uniform microhardness values within a deposited component.

2. Experimental methodology

Experiments were conducted to assess the impact of the developed controller on deposition macrostructure, microstructure, and microhardness. Deposits were made with both uncontrolled (i.e. purely feed-forward) and controlled processing parameters. Details of the experiments follow.

2.1. Physical setup and parameters

Experiments were conducted with an Optomec LENS® MR-7, laser-based, DED system (subsequently referred to as LENS). The system used a 500 W, Ytterbium-doped fiber laser (IPG YLR-500-SM). The laser fiber was coupled to a 200 μm, multimode optical fiber and focused to a D4σ (second moment) spot size of 0.624 ± 12 μm, measured using a PRIMES GmbH FocusMonitor device. As shown in Figs. 1 and 2, the focused beam exited the laser head through a coaxial, center-purge nozzle. Through the center purge nozzle, 30 lpm of argon gas flowed, coaxially, out of a 6.35 mm diameter orifice and toward the substrate below. Around the coaxial nozzle were four, radially symmetrically oriented, powder-delivery nozzles through which 4 lpm of argon gas carried a 3 g/min flow of metal powder out of a 1.19 mm orifice.

The LENS processing chamber was filled with argon gas and maintained at a gauge pressure between 498 and 748 Pa (2–3 in. of water). Oxygen levels were kept below 20 ppm during processing.

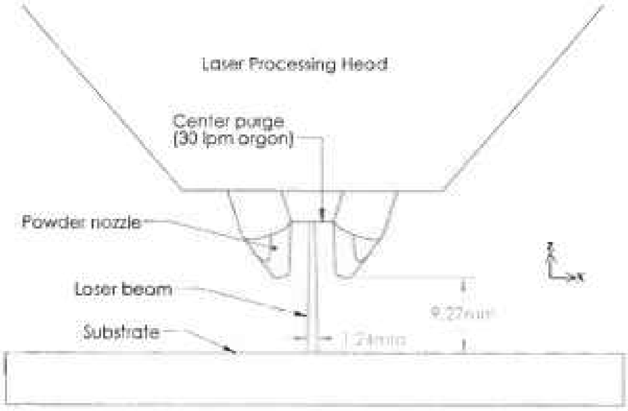

Fig. 1. Experimental setup on the laser-based, directed-energy-deposition system (Optomec, Inc. LENS).

A substrate was positioned at the working distance of 9.27 mm below the powder-delivery nozzles. At this position, below the laser focal point, the laser was defocused to a spot size of 1.24 mm. During deposition, the substrate was translated in the *X*–*Y* plane while the laser processing head remained stationary. Upon completion of a layer, the laser head moved upwards by a predefined layer height. Stage motion was controlled by a Galil DMC-1880 Motion controller. Stage position error was less than 10 μm.

During deposition, part temperature was monitored using a Raytek GPSCFLW series, single-wavelength pyrometer. A constant emissivity value of 0.40 was assumed – this was a rough estimate based on the results of Hagqvist et al. [32] and correlation with thermocouple measurements. The pyrometer measured the average temperature in a 4.5 mm diameter spot around the laser position. The pyrometer outputted a 0–10 V signal which was linearly scaled with the measured temperature. Noise in the analog signal was estimated to contribute an error of ±2 °C to measured values. The temperature around the start point of each potential hatch, prior to deposition, was used to actively control hatch order.

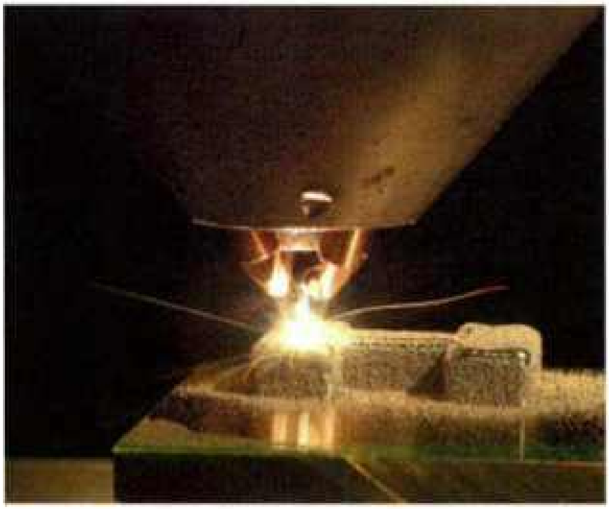

Fig. 2. Image of processes during deposition of Ti–6Al–4V within the LENS system.

2.2. Materials

The powder used for deposition was Grade 5 titanium (Ti–6Al–4V) with extra low interstitials (ELI grade), purchased from Phelly Materials, Inc. The powder was verified to be spherical with a mean particle size of 126.8 μm (45.9 μm stdev) using scanning electron microscope imaging and a Horiba LA950 particle size distribution analyzer, respectively. Powder was deposited atop a 76.2 mm × 76.2 mm Ti–6Al–4V substrate, with a thickness of 6.35 mm.

2.3. Processing parameters

Hatching parameters were determined following the method outlined by Policelli [33]. At a measured output laser power of 450 ± 25 W and a processing speed of 10.58 mm/s (25 in./min), the geometry of single-track deposits were used to determine hatch spacing and layer thickness. To reduce the likelihood that hatch skipping would result in lack-of-fusion, the bead contact angle, with respect to the substrate, was measured and verified to be at an obtuse angle (159°). Based on this analysis, a hatch spacing of 0.91 mm (0.036 in.) and a layer thickness of 0.18 mm (0.007 in.) were used for deposition of the part geometry. It may be noted that these parameters resulted in deposition of a layer thicker than the upwards movement of the laser deposition head between layers. This overbuilding on each layer is typical in directed-energy processes and was used to ensure that the powder streams converged toward the melt pool; in the case of underbuilding, the powder would have diverged near the melt pool, resulting in little to no deposition.

2.4. Control hardware, software and dataflow

To enable real-time control of hatch order, custom software and hardware systems were integrated into the LENS machine. The system's workflow is provided in Fig. 3. First, a 3D computer-aided design (CAD) model was constructed and exported as a Standard Tessellation Language (STL) file. Next, the part orientation (build direction) was defined and the STL file was sliced into layers. Each layer was defined using a poly-line boundary representation within a common layer interface (CLI) format. These first steps, construction of the STL file, part orientation and slicing, were completed using commercial software – SolidWorks® Premium 2012 and netfabb® Studio Professional 4.

Based on the slice data, custom-written software was used to generate two sets of instructions: LENS machine code and an Additive Manufacturing Slice File (AMSF) file [34]. Machine code was formatted in the Digital Motion Controller (DMC) language, defined by Galil Motion Control, Inc. Within the DMC code, instructions defined a communication schema between the Galil motion controllers and an external computer (referred to as PSU computer). The PSU computer was equipped with a National Instruments USB 6343 multifunctional

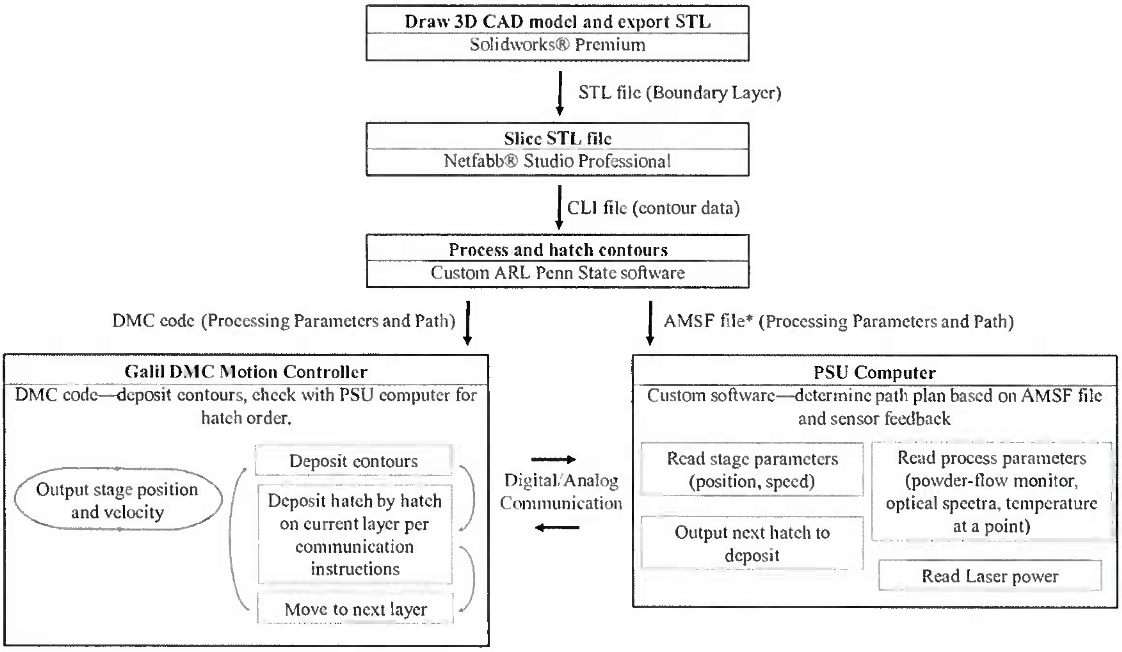
Draw 3D CAD model and export STL
Solidworks® Premium
STL file (Boundary Layer)
Slice STL file
Netfabb® Studio Professional
CLI file (contour data)
Process and hatch contours
Custom ARL Penn State software
DMC code (Processing Parameters and Path)
AMSF file* (Processing Parameters and Path)
Galil DMC Motion Controller
DMC code—deposit contours, check with PSU computer for hatch order.
Output stage position and velocity
Deposit contours
Deposit hatch by hatch on current layer per communication instructions
Move to next layer
Digital/Analog Communication
PSU Computer
Custom software—determine path plan based on AMSF file and sensor feedback
Read stage parameters (position, speed)
Read process parameters (powder-flow monitor, optical spectra, temperature at a point)
Output next hatch to deposit
Read Laser power

Fig. 3. Data flow for near real-time alteration of path plan. The AMSF file description can be found in Ref. [34].

Data Acquisition Device (DAQ). During processing, real-time position data were passed from the motion controller to the PSU computer using two analog (0–10 V) voltages proportional to the (*X* and *Y*-axes) stage position and digital inputs/outputs were used for hand shaking and to communicate hatch order. Analog signal noise contributed an error of less than ±17 µm in the measured position data.

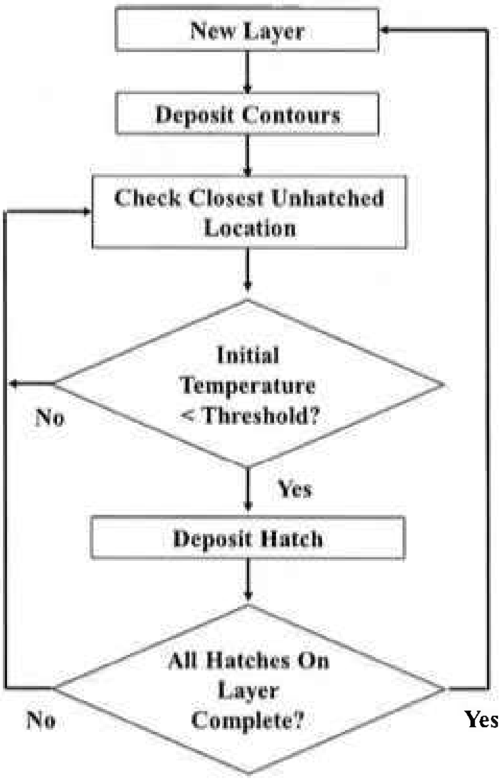
New Layer
Deposit Contours
Check Closest Unhatched Location
Initial Temperature < Threshold?
No
Yes
Deposit Hatch
All Hatches On Layer Complete?
No
Yes

Fig. 4. Flow chart for controller logic for the closed-loop build.

On the PSU computer, custom-written software interpreted the AMSF file and read the current position, hatch, layer, pyrometer reading, and laser power. Based on these data, control decisions were made and the PSU computer communicated hatch deposition sequence in real-time to the motion controller. A diagram of the control logic is provided in Fig. 4.

Throughout the build, the time, stage positions, current hatch and layer number, pyrometer reading, and laser power were monitored by the PSU computer. Meanwhile, the motion controller was instructed to deposit all contours on each layer, check for instructions from the PSU computer and modify hatch order as directed. Each hatch was assigned an index number and assigned a threshold initial temperature. All hatches were assigned a threshold value of 415 °C. This threshold was selected for reasons of practicality – it was slightly below the saturation limit of the pyrometer at the chosen emissivity. As shown in Fig. 4, in the closed-loop build, if the initial temperature at the start point of a potential hatch exceeded the threshold value, that hatch was skipped. Then, to minimize processing time, the next closest potential hatch location was checked. On each layer, all potential hatch locations were cycled through before a previously measured hatch temperature was rechecked.

2.5. *Part geometry*

A dogbone geometry, shown in Fig. 5, was selected in order to test the controller on a geometry with regions of varying thermal characteristics. On each layer, a contour was first deposited followed by a series of hatches. This sequence is illustrated in Fig. 6 for the uncontrolled (open-loop) build. The contour was

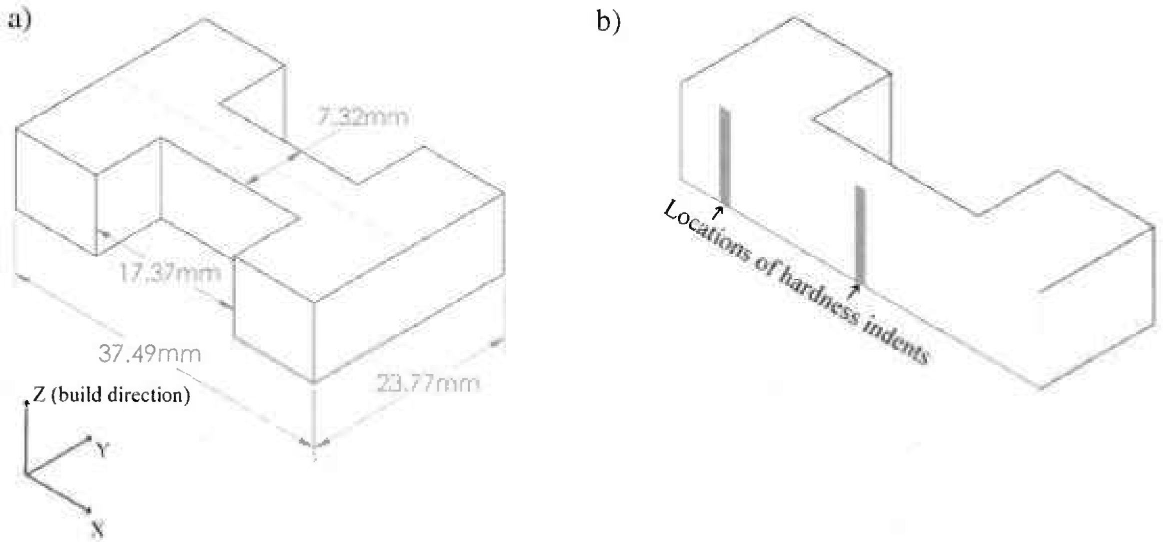
a)
7.32mm
17.37mm
37.49mm
23.77mm
Z (build direction)
Y
X
b)
Locations of hardness indents

Fig. 5. (a) Build geometry. The part was cross-sectioned along the dashed gray centerline. (b) Hardness was measured along the center of the wide, left region and along the center of the narrow, middle region.

deposited along the poly-line defined by points C1,C2,. . .,C*n*, shown in Fig. 6. Following deposition of the contour, hatches were deposited using a zig–zag, raster in the location and direction shown in Fig. 6. Text above each arrow in Fig. 6 indicates the order of deposited hatches. A hatch location number is located at the top of the figure. The hatch location number corresponds to each potential hatch position and is numbered sequentially along the *x*-axis. In the open-loop case, hatch order numbers correspond to hatch location numbers. In total, 40 hatches and 25 layers were deposited.

2.6. Characterization

Once deposited, both open-loop and closed-loop builds were cross-sectioned parallel to their length and along the centerline shown in Fig. 5. For each sample, both cross-section halves

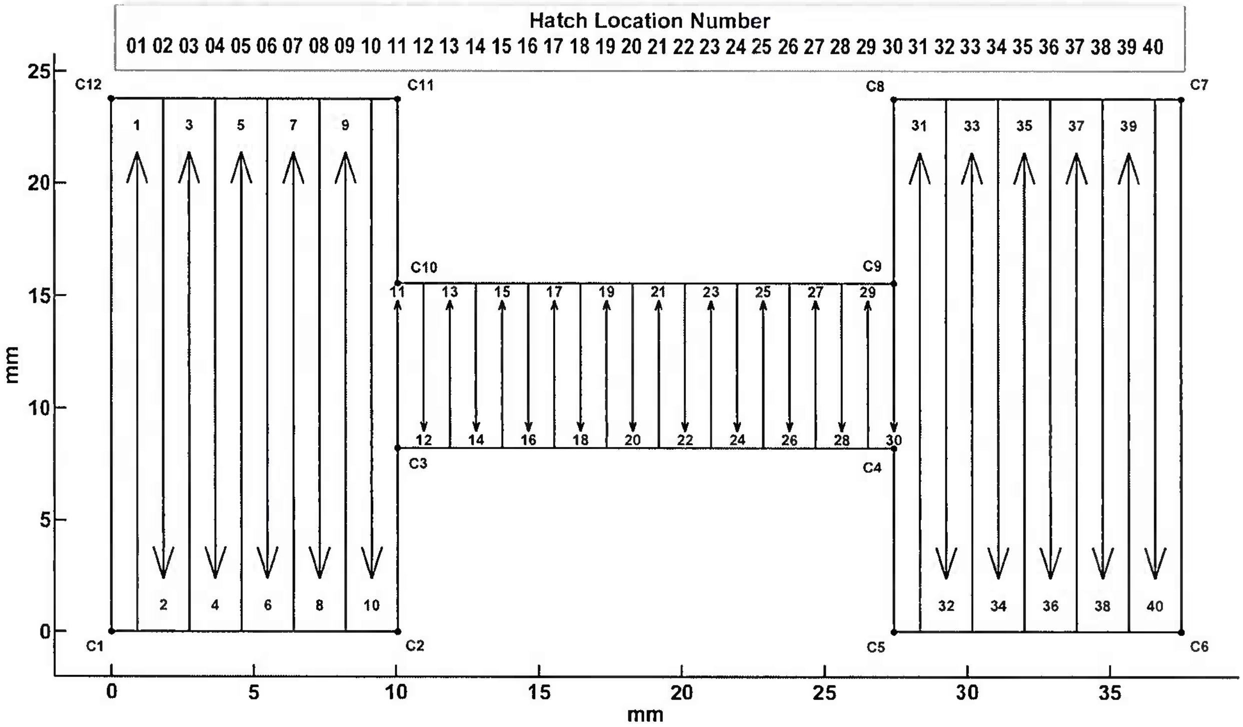
Hatch Location Number
01 02 03 04 05 06 07 08 09 10 11 12 13 14 15 16 17 18 19 20 21 22 23 24 25 26 27 28 29 30 31 32 33 34 35 36 37 38 39 40
C12
C11
C8
C7
C10
C9
C3
C4
C1
C2
C5
C6
1
3
5
7
9
2
4
6
8
10
11
13
15
17
19
21
23
25
27
29
12
14
16
18
20
22
24
26
28
30
31
33
35
37
39
32
34
36
38
40
mm
25
20
15
10
5
0
0
5
10
15
20
25
30
35
mm

Fig. 6. On each layer, a contour, defined by points C1,. . .,C*n*, was first deposited. In the open-loop build, hatches were deposited according to the order and direction shown. Hatch order numbers are located above each hatch arrow while the hatch location number is at the top of the figure. Note that the starts and ends of all hatches actually extend to contour perimeters.

were ground and polished following standard metallographic techniques. One cross-section half from each part was etched using Krolls reagent and studied using optical microscopy. On the etched cross-section, Vickers hardness was measured using a LECO-M-400-G1 hardness tester using a load of 1 kgf applied for 10 s. Hardness was measured, as a function of build height, at the two locations shown in Fig. 5(b): through the middle, narrow region and the left, wide region of the geometry. Within both regions, reported hardness values represented the average of three measurements along each depth and the standard deviation of the three measurements was represented by error bars. Unetched cross-sections were examined using a FEI Quanta 200 and a Philips XL30 environmental scanning electron microscope (SEM) in back-scattered imaging mode. From the SEM images, measurements of the α-lath widths were calculated from 20 manual measurements at random locations within each image.

3. Results and discussion

The objectives of this work were to develop an intra-layer control strategy, to assess the behavior of the control system though a case that employed temperature feedback as input to a path controller, and to determine its effects on the microstructure and hardness of the deposited part. The behavior of the system was assessed by comparing the time required to deposit all hatches on each layer, the hatch deposition order, and the initial temperatures prior to each hatch deposition. Compared to the open-loop build, the closed-loop build exhibited differences in macrostructure, microstructure, and hardness. The behavior of the control system is discussed in Section 3.1, followed by a review of macro and microstructure in Section 3.2, and the resulting microhardness along the depth of the deposited component in Section 3.3. Here, results are combined with discussion.

3.1. Behavior of control system

In the open-loop build, hatches were deposited on all layers in a sequential order as shown in Fig. 6. By the third layer, the initial temperature at the start point of most potential hatches exceeded the 415 °C threshold temperature. In the closed-loop build, the hatching sequence was significantly altered for all but the first layer.

To illustrate this, the hatching deposition sequence midway through the closed-loop build, on layer 13, is shown in Fig. 7. As in Fig. 6, the text above each arrow indicates the order of deposited hatches. The hatch location number is located at the top of the figure. Fig. 7 shows a highly active control system; on the first pass, no two hatches were deposited sequentially next to each other. On average, two hatches were skipped between each deposited hatch on this layer. This knowledge may be useful in redesigning the control algorithm; rather than checking the temperature of the nearest hatch, the total deposition time on each layer may be reduced by initially checking the second- or third-nearest hatch temperature.

Skipping of hatches which exceeded the threshold temperature is also illustrated in Fig. 8. Here, the temperature at the start of each potential hatch is shown along with the hatch location number. The threshold temperature is shown as a horizontal, dashed line and the saturation point of the pyrometer is shown as a dash-dot line.

As shown in Figs. 7 and 8, on the first pass, the temperature at the start of each potential hatch initially exceeded the threshold temperature, so the corresponding hatch was temporarily skipped. The average number of potential hatches skipped on the left, wide section of the geometry and the middle, narrow section was two. However, on the right, wide section of the geometry, only one hatch was skipped on average. Intuitively, it would be expected that, due to anticipated heat buildup, more hatches would be skipped in the middle, narrow section than on either end. However, this was not true: on average, an equal number of hatches were skipped on the left and middle sections. More hatches were also skipped on the left section than right section. The reason for this may be related to the deposition of an external contour ($C_1, C_2, \ldots, C_{13}$ in Fig. 7), at the beginning of each layer, before hatching. The contour started and ended at the left side of the geometry. Thus, the left side of the part was already hotter than the right or middle section prior to deposition of the first hatch.

The hatch order on all layers of the closed-loop build is revealed as an image plot in Fig. 9. Within the figure, the abscissa displays the layer number (1 through 25) and the ordinate displays the order of each deposited hatch (the first deposited hatch is bottommost on the axis and the last deposited hatch is topmost on the axis). The gray-scale intensity of each pixel indicates the hatch location number. As illustrated in Fig. 9, the first layer of the closed-loop build was deposited nearly in the same order as in the open-loop build – only hatches 12 and 22 were initially skipped. The number of hatches skipped on each layer increased up till the seventh layer. Beyond the seventh layer, similar patterns of skipped hatches occur on subsequent layer. Thus, the control system drove the process into steady state by the seventh layer.

The image plot of hatch sequences (Fig. 9) also reveals the number of passes (left-to-right or right-to-left hatching sequences) required to deposit each layer. Under closed-loop control, the initial temperature of each hatch was checked sequentially from left to right. Hatches with temperatures above the threshold were added to the end of the queue to be rechecked. In Fig. 9, a sequence of dark to light pixels on a layer indicates left-to right hatching along the positive *x*-axis, while a sequence of light to dark pixels indicates hatching from right-to-left hatching. Fig. 9 shows that on the first layer, only two passes were required, while beyond the second layer, six to seven passes were performed on each layer.

Hatch skipping in the closed-loop build resulted in a 33% increase is total build time compared with the open-loop build. The open-loop build was deposited in 51.56 min, while the closed-loop build was deposited in 68.53 min. The processing time for each layer, plotted in Fig. 10, shows that the layer deposition time increased with each layer, until layer 7. In contrast to the near-constant layer deposition time of 123.4 s (standard deviation of 0.6 s) in the open-loop build, each layer beyond layer seven was deposited in an average time of 166.5 s with a standard deviation of 1.5 s. The same conclusion can be drawn as

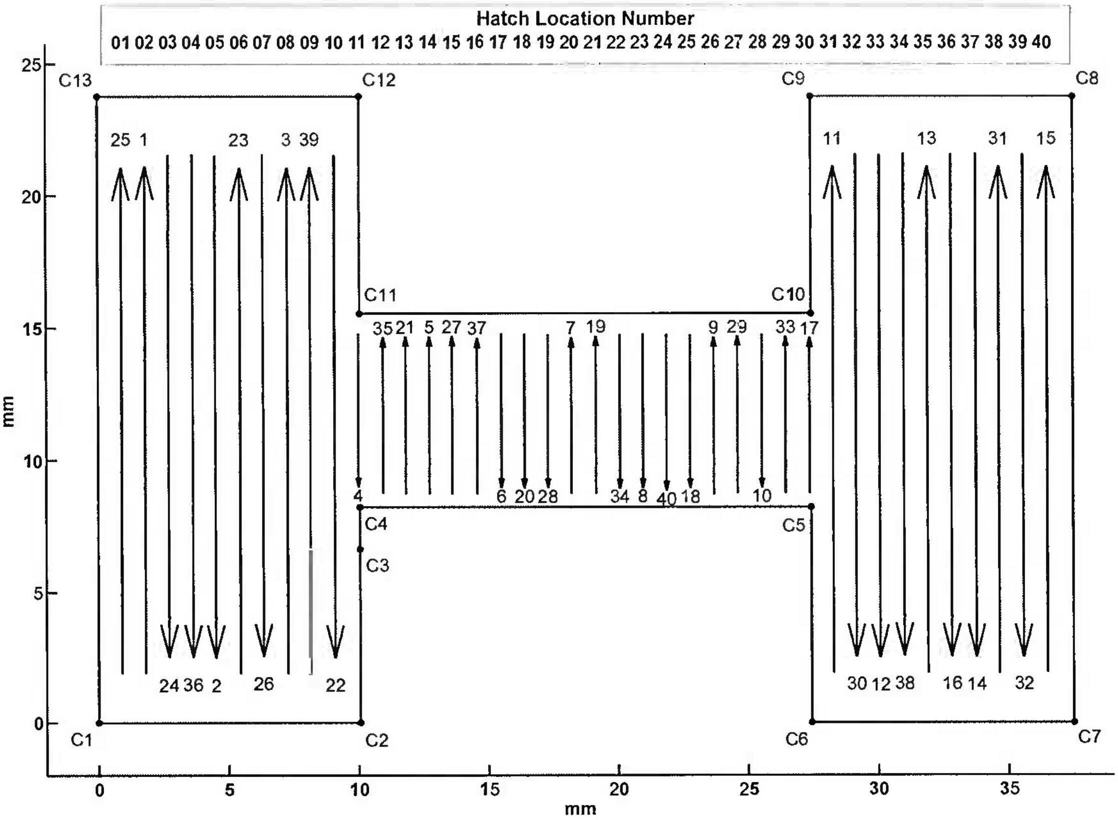
Hatch Location Number
01 02 03 04 05 06 07 08 09 10 11 12 13 14 15 16 17 18 19 20 21 22 23 24 25 26 27 28 29 30 31 32 33 34 35 36 37 38 39 40
C13
C12
C9
C8
C11
C10
C4
C5
C3
C1
C2
C6
C7
25 1 23 3 39
24 36 2 26 22
35 21 5 27 37 7 19 9 29 33 17
4 6 20 28 34 8 40 18 10
11 13 31 15
30 12 38 16 14 32
mm
mm
0
5
10
15
20
25
30
35

Fig. 7. Order of deposited hatches on layer 13 using closed-loop control. Arrows indicate the hatch direction while the numbers at each arrow's end indicates the order (e.g. 1 is the first deposited hatch). Hatch order numbers are located above each hatch arrow while the hatch location number is at the top of the figure. Note that the starts and ends of all hatches actually extend to contour perimeters.

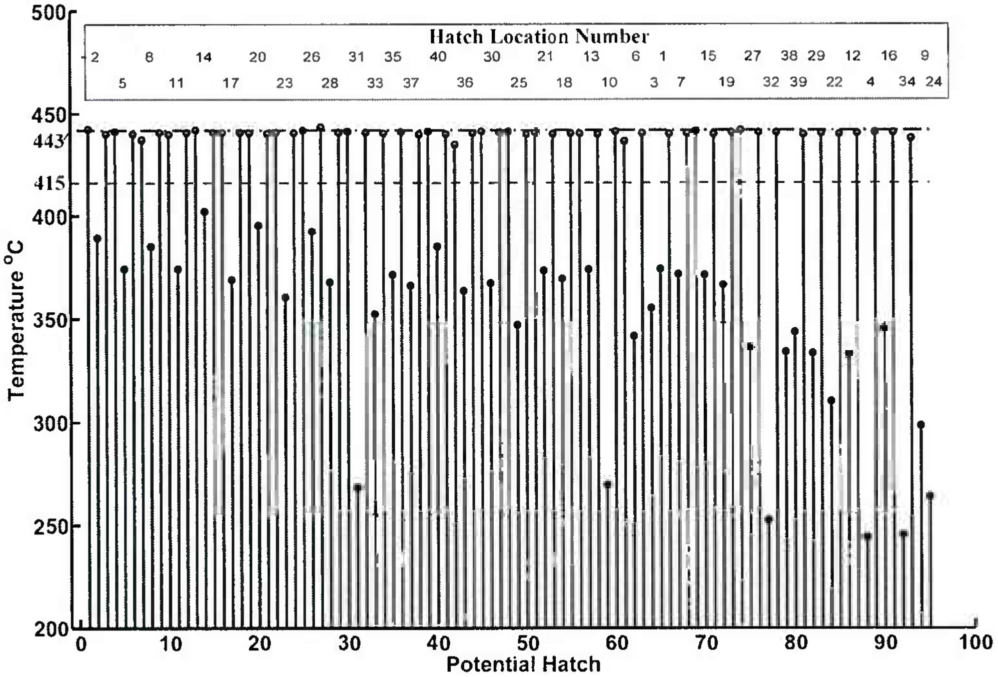

Fig. 8. Measured temperature at the start of each potential hatch on layer 13. The threshold temperature is shown as a horizontal, dashed line at 415 °C. The saturation temperature is a dash-dot line at 443 °C. The hatch location number is shown at the top of the figure.

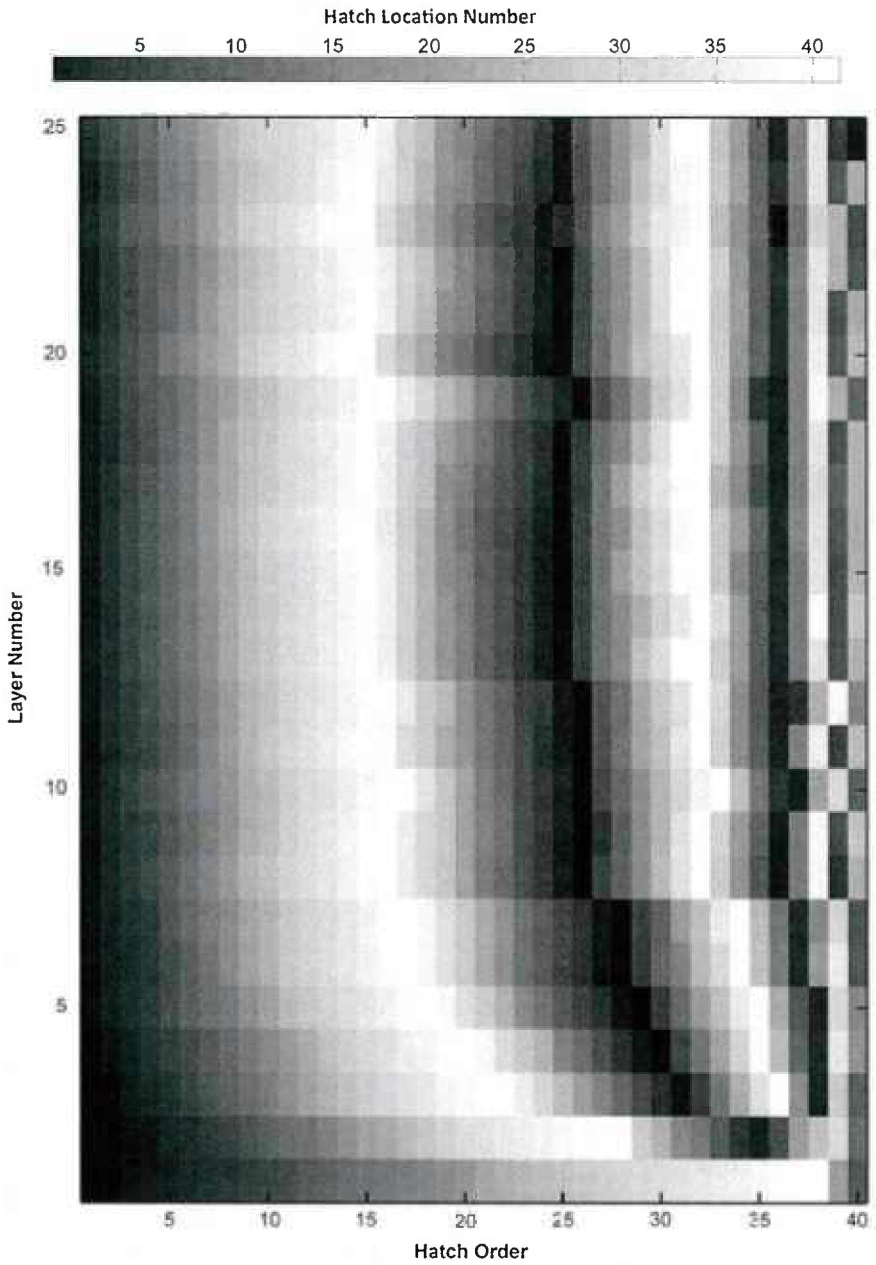

Fig. 9. This image shows the order and location of the deposited hatches, for each layer, in the closed-loop builds. The hatch location number is indicated by the gray-scale color bar. On each layer (vertical axis), the location at which a hatch was deposited can be determined by matching the hatch order (horizontal axis) with the hatch location number (top color bar).

earlier: the control system drove the processes into a near-steady state by the seventh layer.

In summary, the control system was highly active during the build. The hatching sequence was significantly altered for all but the first layer. The time to deposit each layer increased with each deposited layer until reaching a steady-state by the seventh layer. The order in which hatches were deposited similarly reached a steady-state by the seventh layer. Beyond the seventh layer, an average of two hatches were skipped on each pass. This suggests a potential improvement in the control algorithm: checking the second- or third-nearest hatch temperature rather than the temperature of the nearest hatch.

3.2. *Effect of control on macro and microstructure*

In both the open-loop (Fig. 11(a)) and closed-loop (Fig. 11(b)) builds, the macrostructures parallel to their length and along the centerlines, were characterized by large, columnar prior-β grains extending several millimeters in length from above the heat-affected zone (HAZ) to the top of the build. This is typical of AM Ti–6Al–4V deposits and has been explained to result from epitaxial layer-to-layer grow of β grains, from the bottom to the top of the solidifying melt pool, prior to cooling [7,8]. There was however a difference, between the open- and closed-loop builds: the orientation of prior-β grains. While

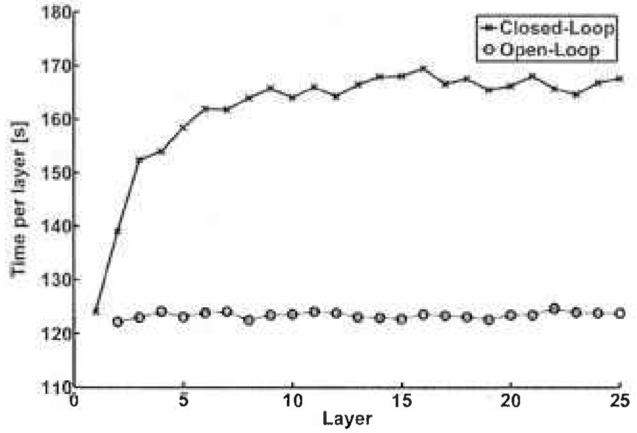

Fig. 10. Deposition time per layer for open loop (O) and closed loop (X) builds. Note that the first point in the open-loop sequence is missing due to a data-collection error on the first layer.

columnar prior-β grains were slanted away from the vertical direction in the open-loop build, β grains were nearly vertical in the closed-loop build. This is consistent with previous observations that columnar β grains orient themselves parallel to the thermal gradient [7,8].

To explain the slanting of prior-β grains, consider an uncontrolled, sequential hatching strategy proceeding from left to right, shown in Fig. 12. Due to multiple laser passes, the temperature on the left-hand side of the last drawn hatch is higher than the substrate temperature to the right of the last hatch. Assuming cooling is dominated by conduction of heat into the part, temperature gradients can be expected to appear as sketched in Fig. 12 and the thermal gradient will be oriented down as shown in the figure. Because β grains orient themselves along the thermal gradient and grow epitaxial from layer to layer, they will appear slightly slanted in the open-loop build (Fig. 11(a)). In contrast to this, the closed-loop build required initial hatch temperatures to be below a defined threshold and resulted in multiple back-and-forth passes on each layer. Heat input was spread more uniformly on each layer and the thermal asymmetry along each side of a deposited hatch was reduced. Thus, temperature gradients were oriented perpendicular to the substrate surface, resulting in vertically aligned, rather than slanted, prior-β gains.

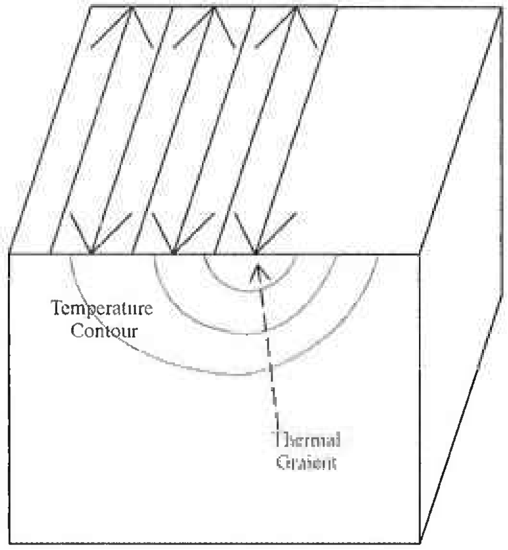

Fig. 12. Illustration of thermal gradients during sequential hatching.

Within the columnar, prior-β grains, the microstructure of each build appeared to consist of fine, acicular α platelets with a small amount of intergranular β. Scanning electron microscope (SEM) images, recorded in backscattered mode, of the open-loop and closed-loop builds along the center of the middle, narrow section of the geometry, are shown in Fig. 13. Corresponding measurements of the α-lath widths, as a function of distance from the top of the deposit, are provided in Table 1. In

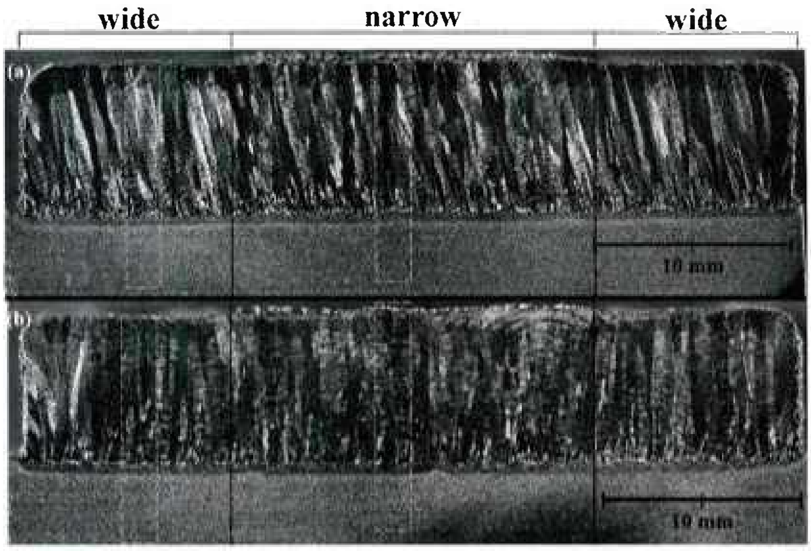

Fig. 11. Macrostructure of the (a) open-loop and (b) closed loop builds. The gray, dashed rectangles indicate the locations of hardness indents. On each build, hatching started from left to right.

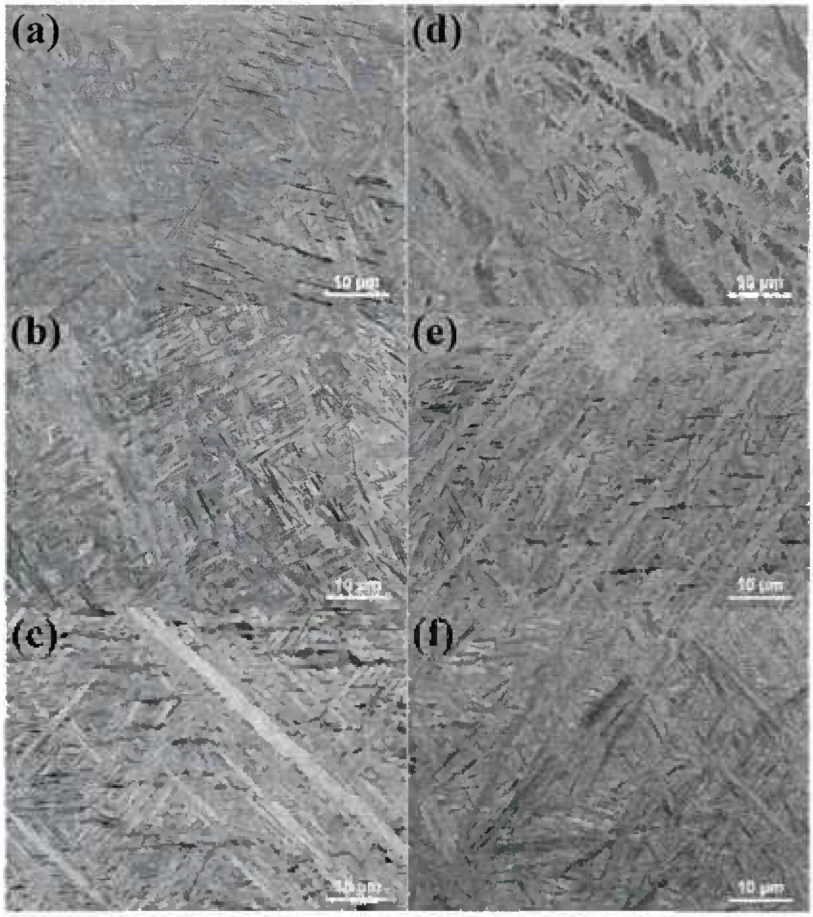

Fig. 13. Backscatter SEM images through the middle of the open-loop (a–c) and closed loop (d–f) builds. Microstructure was imaged at (a, d) 1 mm, (b, e) 4 mm, (c, f) 6 mm from the top surface of each build.

Table 1
α-Lath width through the middle of the open-loop and closed loop builds.

Distance from top (mm)	α-Lath width (μm)	Standard deviation (μm)
Open-loop		
1	0.47	0.11
4	0.63	0.13
6	0.95	0.28
Closed-loop		
1	0.29	0.07
4	0.30	0.08
6	0.33	0.08

the open-loop build (Fig. 13(a–c)), the width of α laths increased from the top to the bottom of the deposit. The change in lath width with distance from the top of the deposit was verified as statistically significant (p-value < 3.82e − 10) using an Analysis of variance (ANOVA) assuming a 95% confidence interval for the mean. In the closed-loop build (Fig. 13(d–f)), no statistically significant change in lath width with location was found (ANOVA p-value > 0.23). Average lath-widths were approximately 1.6–2.9 times smaller in the closed-loop build than in the open-loop build.

Differences in the α-lath widths between the open- and closed-loop builds can be attributed to differences in thermal conditions during the builds. Kelly and Kampe [35] have argued that wider α laths, within directed-energy deposited parts, may result from greater time above some threshold temperature below the β transus (996 °C). If correct, this may explain why the open-loop build exhibited wider α-laths and why lath width decreased with build height.

In addition to differences in α-lath width, the microstructures exhibit differences in the degree of contrast observed using backscattered electrons. As shown in Fig. 14, greater contrast was observed in the open-loop build (Fig. 14(a)) then in the closed-loop build (Fig. 14(b)). Note that contrast was enhanced in each image using contrast stretching, such that grayscale intensities were assigned linearly from the darkest to the brightest values in each the image. The greater variations in local contrast – and more clearly defined α plates – in the open-loop, compared with the closed-loop, build suggests that diffusion of alloying elements was greater in the open-loop build. We attribute this, like wider α-laths, to the greater length of time the part was exposed to some threshold temperature within the α–β phase field. A similar explanation was suggested by Griffith et al. [36] for an observed

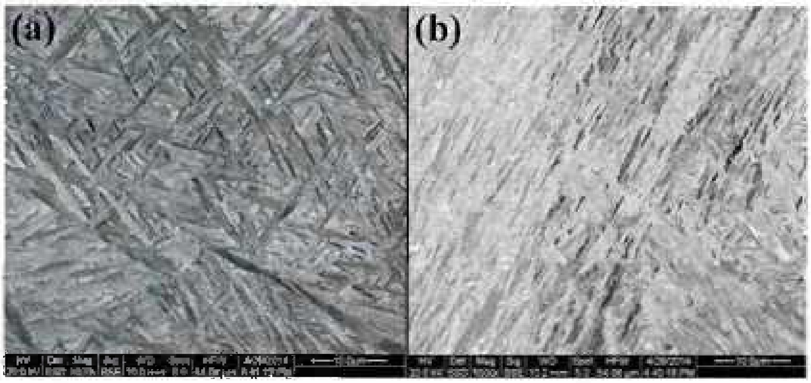

Fig. 14. Backscatter SEM images of (a) open-loop and (b) closed-loop builds taken at 4 mm from the top surface of the build. Images were recorded using the same magnification, acceleration voltage, and beam spot size. Greater contrast was observed in (a) the open-loop build then in (b) the closed-loop build, suggesting greater diffusion of alloying elements in the open-loop build.

reduction in hardness from the top to bottom of LENS-deposited of a H13 tool steel. They speculated that hardness variations were due to the tempering effect of multiple heat cycles and the resulting redistribution of carbide within the material.

3.3. Hardness

Variations in hardness were also observed between the open-loop and closed-loop builds. The hardness profile, as a function of build height, is shown in Fig. 15 for the middle, narrow region

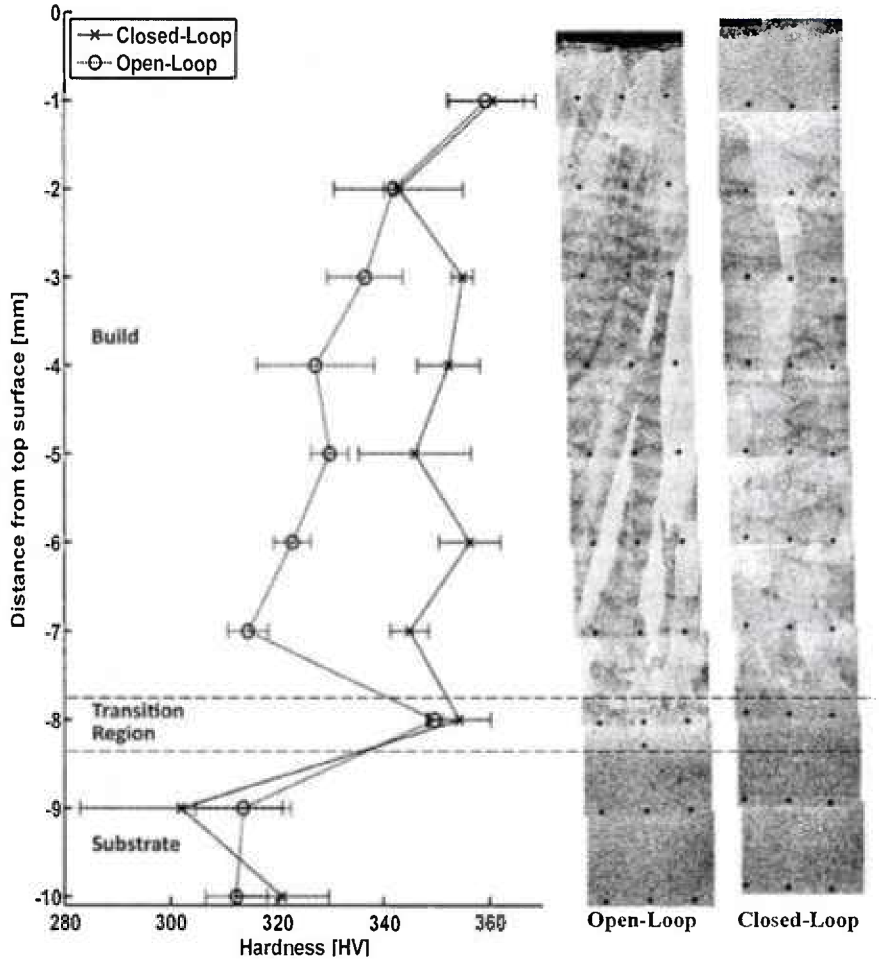

Fig. 15. The hardness profile along the middle region of the dog bone build. Approximate boundaries of the build and substrate are shown. Indents in the transition region were within the fusion zone. The sample processed with closed-loop-build-plan control was more homogeneous throughout the build than that processed without control.

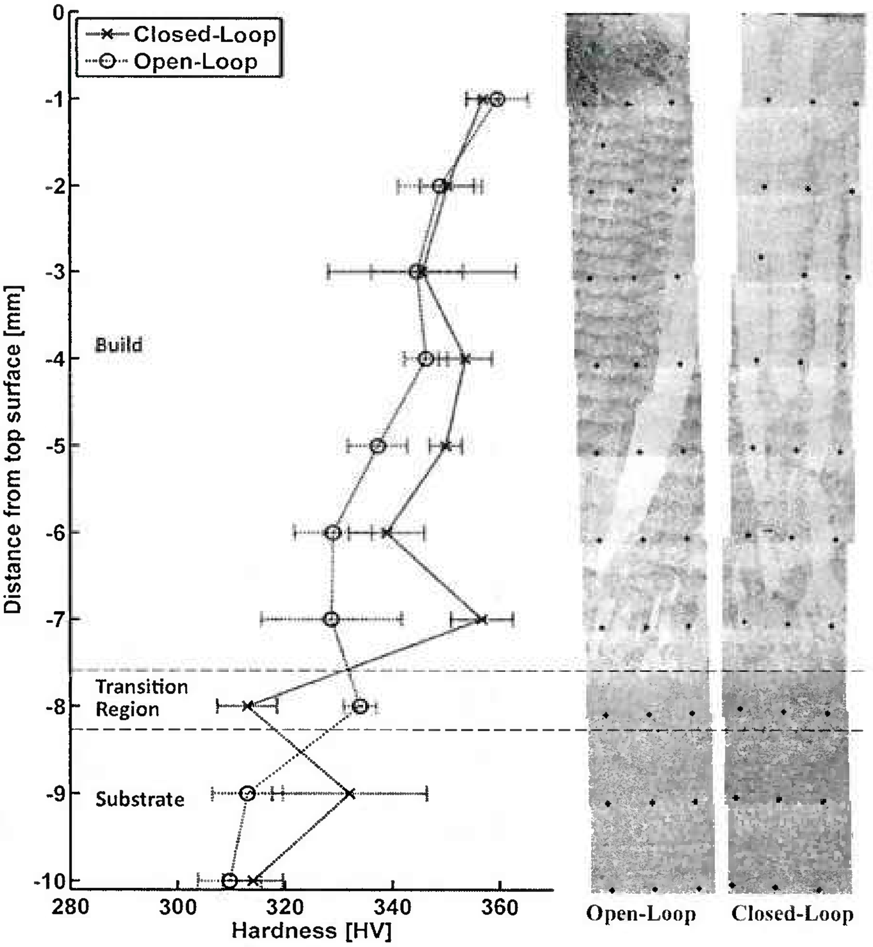

Fig. 16. Hardness along height of the left, wide region of dog bone deposit. Approximate boundaries of the build and substrate are shown. Indents within the transition region were in the heat-affected zone. The sample processed with closed-loop-build-plan control was more homogeneous throughout the build than that processed without control.

and in Fig. 16 for the left, wide region of the geometry. Through both regions, similar patterns emerged for the open-loop build: the hardness was greatest near the top surface of the build, became softer with increasing distance from the surface and then spiked in hardness within the fusion zone before reaching the substrate hardness. A similar pattern has been reported by Griffith et al. [36] for deposition of a one-bead-wide wall using H13 tool steel. In their case, the fall in hardness from the top to bottom of the build was attributed to redistribution of carbide within the material due to multiple heating cycles. Later, Costa et al. [37] demonstrated a similar pattern for a one-bead-wide deposit of AISI 420 stainless steel and showed that it could be affected by actively heating the substrate. Roy [6] also reported hardness variations between the top and bottom section of a Ti–6Al–4V part deposited using electron beam melting. Based on these reports, it appears that hardness variations with build height are a byproduct of the thermal cycling inherent in laser and e-beam AM processes.

Closed-loop control reduced the top-to-bottom variation in hardness. Through the middle, narrow region of the sample, for the open-loop build, hardness varied approximately from approximately 360 HV at 1 mm below surface of the deposit to below 315 HV at 7 mm below the surface of the build. At approximately the same coordinates in the closed-loop build, hardness varied from 360 to 345 HV. The open-loop build had significantly different (unpaired t-test with 95% confidence intervals, p-value = 0.002) hardness values at the surface of the build compared to 7 mm below its surface. At the same locations, the hardness values of the build produced using closed-loop control were not significantly different (p-value = 0.062). The same conclusion was drawn for the hardness through the wider, region of the samples: The hardness values of samples produced without control were significantly different ($p = 0.038$) from top-to-bottom, whereas those under closed-loop control were not significantly different (p-value = 0.935).

In addition, the hardness measured at the middle-height in both builds (the set of measurements at 4, 5 and 6 mm) was significantly different for both narrow regions ($p < 0.00001$) and wide regions ($p = 0.02438$). This difference can only be attributed to the controller. It is therefore concluded that the closed-loop build-plan controller significantly impacted microhardness and effectively reduced microhardness variations, improving overall uniformity, along the build height.

4. Concluding remarks

In this work, we introduced a system architecture to enable closed-loop control of build plan and hatch order during directed-energy additive manufacturing. To demonstrate this system architecture, a temperature-based controller was implemented and evaluated. The control system relied on tight interfacing with a commercial Optomec LENS machine and utilized a simple strategy: if the local, initial temperature of a potential hatch deposition exceeded a threshold temperature (415 °C) within the α–β phase field, it was temporarily skipped; otherwise, the hatch was deposited. This strategy resulted in control of the alignment of prior-β grains, more uniform α-lath widths, and possibly less diffusion of alloying elements within the build. In addition, uniformity of microhardness within the controlled build was enhanced.

The results indicate that intra-layer, build-plan control provides significant advantages and greater research along this direction is warranted. Additionally, controllers modeled after the one presented here offer tremendous flexibility in terms of control strategy. For instance, the threshold temperature can be specified for every possible deposition path based on heuristic knowledge or physics-based models. With slight modifications, specific paths can also be altered in mid-build, for control of macrostructure, microstructure, residual stress, distortion, and part properties. One topic of future research is how closed-loop control of path plan impacts uniformity of other physical properties, such as fatigue, elongation and strength along with potential for in-process defect corrections.

Acknowledgments

We acknowledge Mr. Edward A. Good for assistance in preparing metallographic samples. Funding for this work was provided by the Office of Naval Research, under Contract No. N00014-11-1-0668. Any opinions, findings and conclusions or recommendations expressed in this publication are those of the authors and do not necessarily reflect the views of the Office of Naval Research.

References

[1] Brandl E, Leyens C, Palm F. Mechanical properties of additive manufactured Ti–6Al–4V using wire and powder based processes. IOP Conf Ser Mater Sci Eng 2011;26:012004, http://dx.doi.org/10.1088/1757-899X/26/1/012004.

[2] Rafi KH, Karthik NV, Starr TL, Stucker BE. Mechanical property evaluation of Ti–6Al–4V parts made using electron beam melting. In: Solid free. fabr. symp. proc. Austin, TX: University of Texas; 2012. p. 526–35.

[3] Tolosa I, Garciandía F, Zubiri F, Zapirain F, Esnaola A. Study of mechanical properties of AISI 316 stainless steel processed by selective laser melting, following different manufacturing strategies. Int J Adv Manuf Technol 2010;51:639–47, http://dx.doi.org/10.1007/s00170-010-2631-5.

[4] Hrabe N, Quinn T. Effects of processing on microstructure and mechanical properties of a titanium alloy (Ti–6Al–4V) fabricated using electron beam melting (EBM), Part 2: Energy input, orientation, and location. Mater Sci Eng A 2013;573:271–7, http://dx.doi.org/10.1016/j.msea.2013.02.065.

[5] Bass BS [Master of Science] Validating the arcam EBM process as an alternative fabrication method for titanium–6Al–4V alloys. North Carolina State University; 2007.

[6] Roy L [Master of Science] Variation in mechanical behavior due to different build directions of Ti6Al4V fabricated by electron beam additive manufacturing technology. Tuscaloosa: The University of Alabama; 2013.

[7] Al-Bermani SS, Blackmore ML, Zhang W, Todd I. The origin of microstructural diversity, texture, and mechanical properties in electron beam melted Ti–6Al–4V. Metall Mater Trans A 2010;41:3422–34, http://dx.doi.org/10.1007/s11661-010-0397-x.

[8] Antonysamy AA, Meyer J, Prangnell PB. Effect of build geometry on the β-grain structure and texture in additive manufacture of Ti6Al4V by selective electron beam melting. Mater Charact 2013;84:153–68, http://dx.doi.org/10.1016/j.matchar.2013.07.012.

[9] Kruth J-P, Badrossamay M, Yasa E, Deckers J, Thijs L, Van Humbeeck J. Part and material properties in selective laser melting of metals. In: Proc. 16th int. symp. electromachining. 2010.

[10] Thijs L, Verhaeghe F, Craeghs T, Humbeeck JV, Kruth J-P. A study of the microstructural evolution during selective laser melting of Ti–6Al–4V. Acta Mater 2010;58:3303–12, http://dx.doi.org/10.1016/j.actamat.2010.02.004.

[11] Baufeld B. Effect of deposition parameters on mechanical properties of shaped metal deposition parts. Proc Inst Mech Eng B: J Eng Manuf 2011;226:126–36, http://dx.doi.org/10.1177/0954405411403669.

[12] Kobryn PA, Semiatin SL. Laser forming of Ti–6Al–4V: research overview. In: Solid free. fabr. symp. proc. Austin, TX: University of Texas; 2000.

[13] Dinda GP, Dasgupta AK, Mazumder J. Laser aided direct metal deposition of Inconel 625 superalloy: microstructural evolution and thermal stability. Mater Sci Eng A 2009;509:98–104, http://dx.doi.org/10.1016/j.msea.2009.01.009.

[14] Araujo JR, Rodriguez-Andina JJ, Farina J, Vidal F, Mato JL, Montealegre MA. FPGA-based laser cladding system with increased robustness to optical defects. In: IECON 2012 – 38th annu. conf. IEEE ind. electron. soc. 2012. p. 4688–93, http://dx.doi.org/10.1109/IECON.2012.6389491.

[15] Kruth J-P, Mercelis P, Van Vaerenbergh J, Craeghs T. Feedback control of selective laser melting. In: Proc. 3rd int. conf. adv. res. virtual rapid prototyp. 2007. p. 521–7.

[16] Bi G, Schürmann B, Gasser A, Wissenbach K, Poprawe R. Development and qualification of a novel laser-cladding head with integrated sensors. Int J Mach Tools Manuf 2007;47:555–61, http://dx.doi.org/10.1016/j.ijmachtools.2006.05.010.

[17] Hofman JT, Pathiraj B, van Dijk J, de Lange DF, Meijer J. A camera based feedback control strategy for the laser cladding process. J Mater Process Technol 2012;212:2455–62, http://dx.doi.org/10.1016/j.jmatprotec.2012.06.027.

[18] Hu D, Mei H, Kovacevic R. Closed loop control of 3D laser cladding based on infrared sensing. In: Solid free. fabr. symp. proc. Austin, TX: University of Texas; 2001. p. 129–37.

[19] Bi G, Gasser A, Wissenbach K, Drenker A, Poprawe R. Identification and qualification of temperature signal for monitoring and control in laser cladding. Opt Lasers Eng 2006;44:1348–59, http://dx.doi.org/10.1016/j.optlaseng.2006.01.009.

[20] Song L, Mazumder J. Feedback control of melt pool temperature during laser cladding process. IEEE Trans Control Syst Technol 2011;19:1349–56, http://dx.doi.org/10.1109/TCST.2010.2093901.

[21] Hand DP, Fox MDT, Haran FM, Peters C, Morgan SA, McLean MA, et al. Optical focus control system for laser welding and direct casting. Opt Lasers Eng 2000;34:415–27, http://dx.doi.org/10.1016/S0143-8166(00)00084-1.

[22] Fathi A, Khajepour A, Toyserkani E, Durali M. Clad height control in laser solid freeform fabrication using a feedforward PID controller. Int J Adv Manuf Technol 2006;35:280–92, http://dx.doi.org/10.1007/s00170-006-0721-1.

[23] Zeinali M, Khajepour A. Height control in laser cladding using adaptive sliding mode technique: theory and experiment. J Manuf Sci Eng 2010;1321:041016, http://dx.doi.org/10.1115/1.4002023.

[24] Heralić A, Christiansson A-K, Lennartson B. Height control of laser metal-wire deposition based on iterative learning control and 3D scanning. Opt Lasers Eng 2012;50:1230–41, http://dx.doi.org/10.1016/j.optlaseng.2012.03.016.

[25] Song L, Bagavath-Singh V, Dutta B, Mazumder J. Control of melt pool temperature and deposition height during direct metal

deposition process. Int J Adv Manuf Technol 2011;58:247–56, http://dx.doi.org/10.1007/s00170-011-3395-2.

[26] Muller P, Mognol P, Hascoet J-Y. Modeling and control of a direct laser powder deposition process for Functionally Graded Materials (FGM) parts manufacturing. J Mater Process Technol 2013;213:685–92, http://dx.doi.org/10.1016/j.jmatprotec.2012.11.020.

[27] Carvalho PA, Braz N, Pontinha MM, Ferreira MGS, Steen WM, Vilar R, et al. Automated workstation for variable composition laser cladding – its use for rapid alloy scanning. Surf Coat Technol 1995;72:62–70, http://dx.doi.org/10.1016/0257-8972(94)02333-L.

[28] Boddu MR, Landers RG, Liou FW. Control of laser cladding for rapid prototyping – a review. In: Solid free. fabr. symp. proc. Austin, TX: University of Texas; 2001. p. 6–8.

[29] Reutzel EW, Nassar AR. A survey of sensing and control for metal-based additive manufacturing. In: Solid free. fabr. symp. proc. Austin, TX: University of Texas; 2014.

[30] Steen WM, Mazumder J. Laser automation and in-process sensing. In: Laser material processing. London: Springer; 2010. p. 485–518.

[31] Sun A, Kannatey-Asibu Jr E, Gartner M. Sensor systems for real-time monitoring of laser weld quality. J Laser Appl 1999;11:153–68, http://dx.doi.org/10.2351/1.521893.

[32] Hagqvist P, Sikström F, Christiansson A-K. Emissivity estimation for high temperature radiation pyrometry on Ti–6Al–4V. Measurement 2013;46:871–80, http://dx.doi.org/10.1016/j.measurement.2012.10.019.

[33] Policelli M [B.S.] Development of a New Method to Fabricate Titanium Metal Matrix Composites viaLENS with Improved Material Properties. The Pennsylvania State University; 2011. https://scholarsphere.psu.edu/files/9880vs30g

[34] Nassar AR, Reutzel EW. A proposed digital thread for additive manufacturing. In: Solid free. fabr. symp. proc. Austin, TX: University of Texas; 2013.

[35] Kelly SM, Kampe SL. Microstructural evolution in laser-deposited multilayer Ti–6Al–4V builds: Part I. Microstructural characterization. Metall Mater Trans A 2004;35:1861–7, http://dx.doi.org/10.1007/s11661-004-0094-8.

[36] Griffith M, Schlienger ME, Harwell LD, Oliver MS, Baldwin MD, Ensz MT, et al. Thermal behavior in the LENS process. In: Solid free. fabr. symp. proc. Austin, TX: University of Texas; 1998.

[37] Costa L, Vilar R, Réti T. Simulating the effects of substrate pre-heating on the final structure of steel parts built by laser powder deposition. In: Solid free. fabr. symp. proc. Austin, TX: University of Texas; 2004. p. 643–54.

Appendix 5 – Sensing defects during directed-energy additive manufacturing of metal parts using optical emissions spectroscopy

Nassar A R, Reutzel E W, “Sensing Defects during Directed-Energy Additive Manufacturing of Metal Parts using Optical Emissions Spectroscopy” in *Solid Freeform Fabrication Proceedings. Proc. 2014* Solid Freeform Fabrication Symposium, Austin, TX 2014.

Sensing defects during directed-energy additive manufacturing of metal parts using optical emissions spectroscopy

A. R. Nassar*, T. J. Spurgeon*, and E. W. Reutzel*

* Applied Research Laboratory at the Pennsylvania State University,

University Park, PA 16802

REVIEWED

Abstract

Critical components produced via additive manufacturing must be free of unwanted defects. While defects may be detectable after deposition using nondestructive testing techniques, detecting defects during the deposition process offers many benefits: it may enable users to interrupt deposition to repair the part, or to abort deposition to minimize further loss of time and material. Here, we present a method for real-time defect detection during directed-energy additive manufacturing of metals. The method utilized optical emission spectroscopy and a custom-built data acquisition and control infrastructure. It was implemented on a LENS MR-7 machine, and employed during manufacturing of Ti-6Al-4V components in which defects were intentionally introduced. Emission spectra were correlated with defect locations, determined via computed tomography and metallographic cross-sectioning. Preliminary results indicated that defect formation was correlated with atomic titanium (Ti I) and Vanadium (V I) emissions and that measurement of the line-to-continuum ratio for line emissions could be used for defect detection. Based on these findings, sensing strategies for defect detection and, potentially, in-situ-defect repair may be realizable.

1. Introduction

Additive manufacturing (AM) has emerged as a potentially-transformative technology. However, a key obstacle to adoption of AM as a means to produce components for critical applications is qualification and certification. This is particularly true for manufacturing of metal components. Additively-manufactured, metal components are typically fabricated though powder-bed, powder-blown, or wire-based processes, each of which requires melting and solidification of many individual tracks using a laser or electron beam. During processing, defects can result from improper parameter selection, melt pool instability, greater-than-predicted thermal deformation, environmental or process anomalies (such as gas contamination, a damaged recoater blade, or a clogged powder nozzle), energy source fluctuations, and other machine malfunctions. Monitoring AM processes for such in-process errors is vital to component and process qualification.

Researchers have developed numerous strategies to perform in-process monitoring for metal AM. Broadly, in-process signals can be classified in three categories: beam characteristics, worktable/motion characteristics, and process characteristics [1]. Specifically, researchers have monitored laser/e-beam parameters, melt pool metrics, part temperature, feed material or powder bed, geometry, and optical emissions during processing. See [1]–[4] for reviews on in-process monitoring for laser-materials processing and AM.

A common strategy is sensing and control of melt-pool size [5]–[9] or temperature [10], [11]. Other efforts have attempted to maintain a constant layer build height by directly sensing build height and adjusting processing head position [12], processing speed [13], [14], filler material feed rate [15], or laser power [16]. Recently, researchers have also investigated the use of optical emission spectroscopy (OES) for monitoring of AM processes [17]–[19].

Optical emission spectroscopy has long been used to better understand physical mechanisms and to monitor conditions during laser-materials processing. In CO_2 laser welding of AISI 304 stainless steel, Ancona et al. [20] used in-process OES to measure the excitation temperatures of iron, chromium, and magnesium vapors and found that welding defects correlated with fluctuations in one or more species temperature. OES has also been used to study the effect of gas shielding [21], vaporization [22], [23], and weld quality [24] during laser welding. It has also been used to study processing regimes and oxidation during laser nitriding of titanium [25].

Recent studies by Bartkowiak [17] and by Song, Wang, and Mazumder [18], [19] demonstrate the potential utility of OES for monitoring of AM processes. Using powder-blown, direct-energy deposition, Bartkowiak demonstrated that spectral line emissions varied with energy input during deposition of Inconel 625. Also using directed-energy deposition, Song and Mazumder [18] found that analysis of the ratio of specific chromium (Cr I) to iron (Fe I) emission lines could be used to accurately determine chromium concentration in AM of H13 tool steel mixed with 10-60% chromium. Predictions of the chromium concentration using the gaseous plume excitation temperature and electron density were also attempted, though they proved less reliable than the line ratio technique. Further investigations [19], also indicated that phase transformations can be detected using the line ratio technique. These works, along with earlier works on weld-quality monitoring, inspire the use of OES for investigation of metal-based AM.

Here, OES is used to investigate defect detection during AM of Ti-6Al-4V using the Optomec, Inc. LENS process. Preliminary OES data and analysis techniques are presented. It is demonstrated that the line-to-continuum ratio of spectral atomic line emissions can be correlated with the formation and presence of lack-of-fusion defects.

2. Experimental Setup

Additive manufacturing experiments were conducted on an Optomec LENS MR-7 laser-based, directed-energy-deposition system. The LENS system utilized a 500 watt, Ytterbium-doped fiber laser (IPG YLR-500-SM). The laser beam spot size was measured, using a Primes, GmbH FocusMonitor system, to have a second-moment diameter of 1.24 mm at the working distance. As shown in figure 1, a working distance of 9.27 mm was used, as measured from the substrate to four, radially-symmetrically powder-delivery nozzles. Centered within the four powder nozzles was a center-purge nozzle though which a coaxial flow of argon exited onto the substrate.

A custom designed-and-built, sensor-mounting fixture surrounded the laser processing head. The fixture assembly is shown in figure 1. Mounted onto the fixture was a spectrometer fiber with a 400 µm diameter silica core. The opening of the optical fiber was protected with a UV-fused silica window and located 59.7 mm from the melt pool. The viewing angle of the spectrometer was 75 degrees with respect to the laser beam. The opposite end of the optical fiber was coupled to an Ocean Optics, Inc. HR4000 CG UV-NIR spectrometer with a spectral range from 200 to 1100 nm and an optical resolution of 0.50 nm (full width at half maximum). Absolute intensity calibration was not performed on the spectrometer. The spectrometer was synchronized with part buildup, using custom-written software, such that the time, position, layer, and hatch number were all stored with each collected spectrum. A spectrometer integration time of 100 ms and a capture rate of $8.3\overline{3}$ Hz were used.

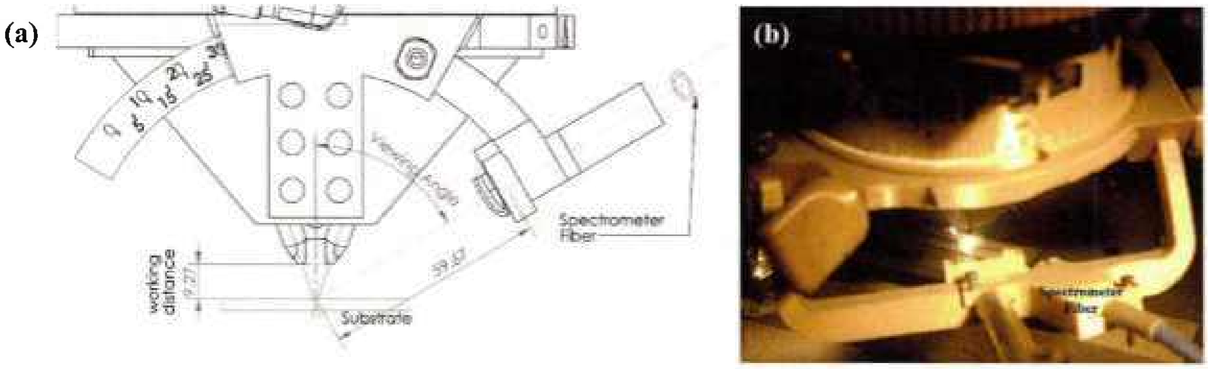

Figure 1: (a) LENS processing head with custom-build, sensor-mounting fixture. (b) Image of fixture, taken during processing, showing spectrometer fiber.

Both the substrate and filler material were ASTM grade 5 titanium (Ti-6Al-4V). The powder was spherical, Extra Low Interstitials (ELI)-grade with a mean particle size distribution of 126.8 µm (stdev = 45.94 µm). The substrate was 3.175 mm thick and ground-finished. Prior to processing, the substrate was cleaned with acetone and isopropyl alcohol.

Processing was conducted in a positive-pressure, argon-filled chamber, maintained at 2 to 3 inches of water (498 to 748 Pa) gauge pressure. Oxygen was below 20 ppm during processing. Titanium powder flow rates were measured at 3 grams per minute. A measured output laser power of 450 W, and a processing speed of 10.58 mm/s were used for part deposition.

A rectangular block, shown in figure 2, with internally-varying hatch spacing was selected for deposition. The block was built-up using a total of 71 layers spaced 0.173 mm apart. On each layer, a total of thirty-nine parallel hatches were deposited. Each hatch was 3.18 mm long, extending along the width of the block. As shown in figure 3, the spacing between hatches was increased from 0.914 mm at one end of the block to 1.829 mm at the other. Hatch spacing was incremented by 0.229 mm every ten millimeters.

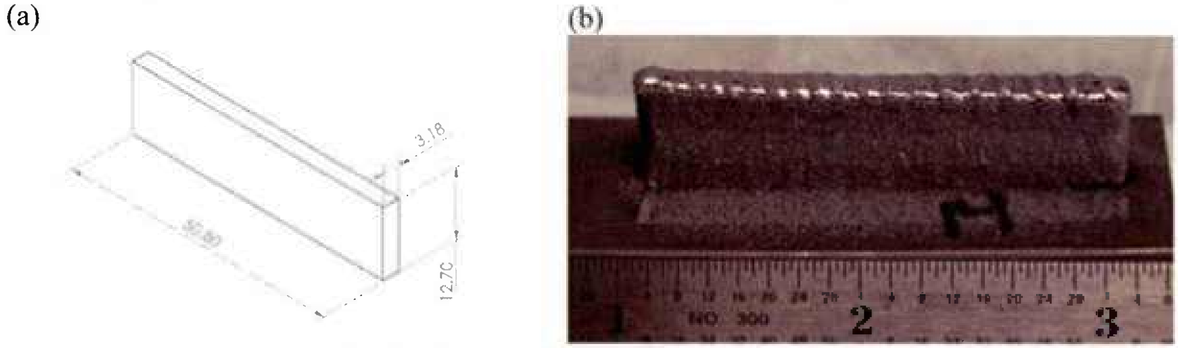

Figure 2: (a) Part geometry with dimensions in millimeters. (b) Image of deposited part.

On each layer, a contour was first deposited along the perimeter of the part, followed by hatches. Hatches were deposited using a zig-zag raster, as shown in figure 3. The order of hatches was unchanged from layer to layer. This geometry was purposely chosen to introduce lack-of-fusion defects between neighboring hatches within the widely-spaced-hatch regions.

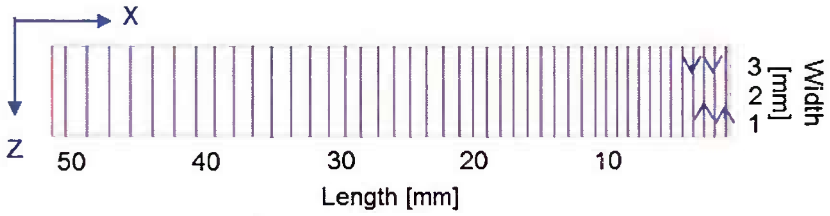

Figure 3: Illustration of deposition path (not to scale). A contour was deposited on each layer followed by hatches starting at the lower right corner of the figure.

After buildup, parts were cross-sectioned through their middle, perpendicular to the hatch vectors, then ground and polished using standard metallographic techniques. Polished cross sections were etched using Krolls reagent and imaged under an optical-microscope equipped with a digital camera. Computed topography (CT) scans were also taken using a GE phoenix v|tome|x m system using a 300 kV microfocus tube.

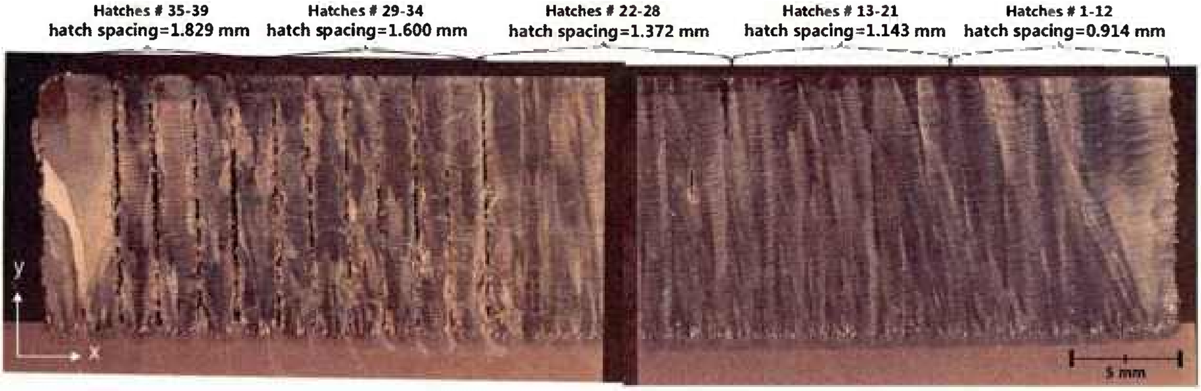
Hatches # 35-39
hatch spacing=1.829 mm
Hatches # 29-34
hatch spacing=1.600 mm
Hatches # 22-28
hatch spacing=1.372 mm
Hatches # 13-21
hatch spacing=1.143 mm
Hatches # 1-12
hatch spacing=0.914 mm
y
x
5 mm

Figure 4: Cross-sectional macrograph of deposited part.

3. Results and Data Analysis

A cross-section, taken though the center of the deposit, perpendicular to the hatching vectors (figure 4), revealed internal lack-of-fusion defects between hatches spaced at and above 1.6 mm apart. CT scans of the build (figure 5) confirmed the presence of defects midway through the width of the build. Lack-of-fusion was most prominent for hatches 35 to 39, which were spaced 1.829 mm apart, though defects were also observed at hatches spaced 1.372 mm apart. Based on CT-scans, these lack-of-fusion defects were observed only between hatches and not along the outer contours of the deposit—see figure 5.

Manual observations of collected spectra indicated that spectral emissions attributable to atomic titanium and vanadium emissions were more intense over regions where defects were observed. Optical emissions captured over layer 35, shown in figure 6, illustrate this observation. Line emissions around 625, 550, 520, 500, 453, 445, 430, and 395 nm were most intense throughout the regions with intentional defects, i.e. hatches 19 through 39.

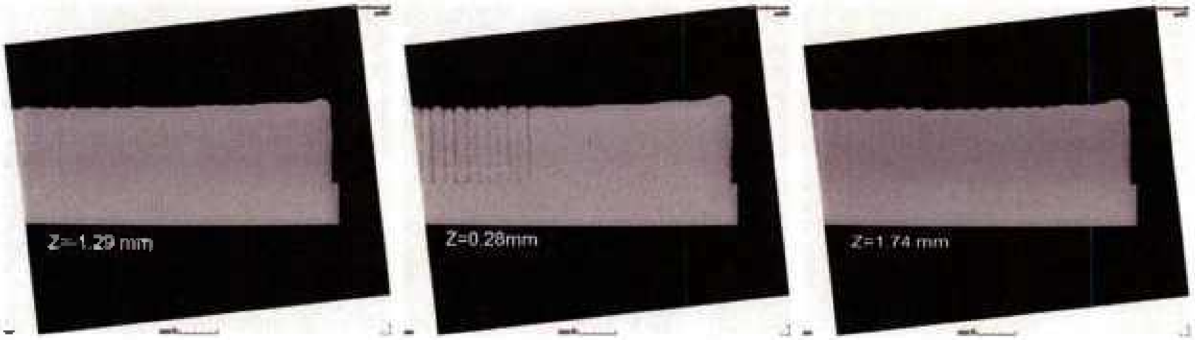
Z=-1.29 mm
Z=0.28mm
Z=1.74 mm

Figure 5: CT-Scans at three locations though the deposit. The center of the deposit was at approximately Z=0 mm.

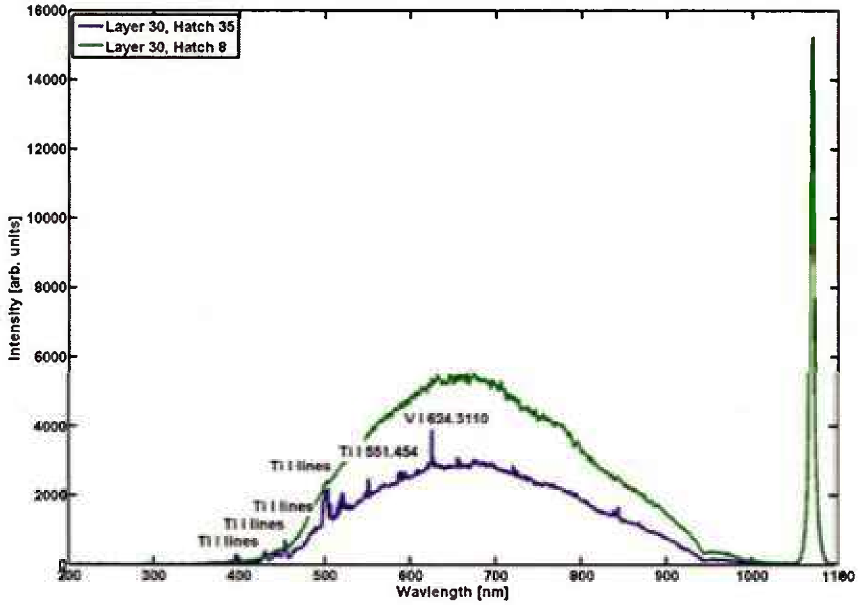

Figure 6: Optical emission spectra captures above hatch 35 (blue) and hatch 8 (green) on layer 30 of the deposit. Atomic emissions of titanium and vanadium were observed over hatch 35, where lack-of-fusion defects were also observed. Note that scattered laser-beam light was observed at 1070 nm.

Based on the observation that line radiation was most prominent over defect regions, a line-to-continuum ratio technique was investigated for correlations with defect location. The continuum radiation was defined according to equation (1),

$$\mathrm{I}_{Continuum} = \int_{\lambda_0-\Delta\lambda}^{\lambda_0+\Delta\lambda} \frac{\mathrm{I}(\lambda_0+\Delta\lambda) - \mathrm{I}(\lambda_0+\Delta\lambda)}{2\Delta\lambda} \cdot \lambda\, d\lambda + \mathrm{I}(\lambda_0-\Delta\lambda) d\lambda, \tag{1}$$

Where $I(\lambda)$ is the observed spectral radiation for a wavelength λ , λ_0 is the central wavelength, and $2\Delta\lambda$ is the wavelength window over which line emissions were observed. Line emissions over the wavelength window was defined according to equation (2),

$$\mathrm{I}_{\lambda_0} = \int_{\lambda_0-\Delta\lambda}^{\lambda_0+\Delta\lambda} \mathrm{I}(\lambda)\, d\lambda - \mathrm{I}_{\mathrm{Continuum}} \tag{2}$$

An illustration of the line radiation and continuum radiation is provided in figure 7. The line-to-continuum ratio was defined as $\mathrm{I}_{\lambda_0}/\mathrm{I}_{Continuum}$.

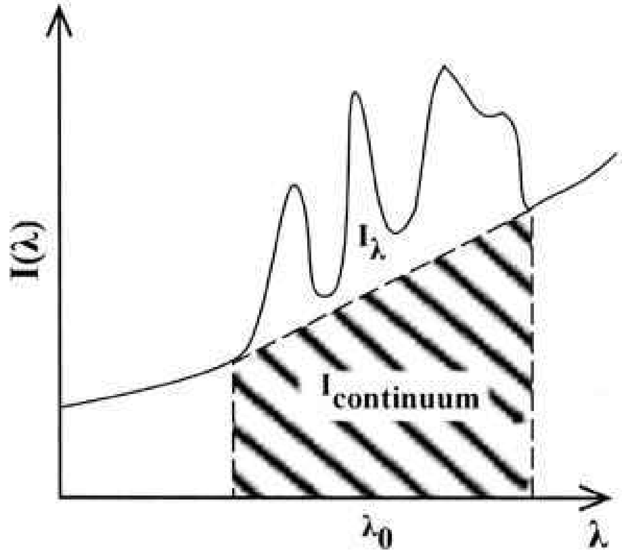

Figure 7: Definition of I_λ *and* $I_{continuum}$.

Preliminary analysis of the line-to-continuum ratio was conducted around 550 nm, with a wavelength window of 10 nm and around 430 nm with a wavelength window of 7 nm. Within each region, several overlapping titanium (Ti I) line emission were observed. The spectrometer resolution was insufficient for deconvolution of individual spectral lines. The average line-to-continuum ratio for each region, on layer 30, as a function of hatch number, is shown in figure 8. Around both 430 and 500 nm, the line-to-continuum ratio was lowest for defect-free hatches. Beyond hatch 28, the line-to-continuum ratio values above 0.3 were observed. This indicated the presence of strong line emissions over defect-containing hatches.

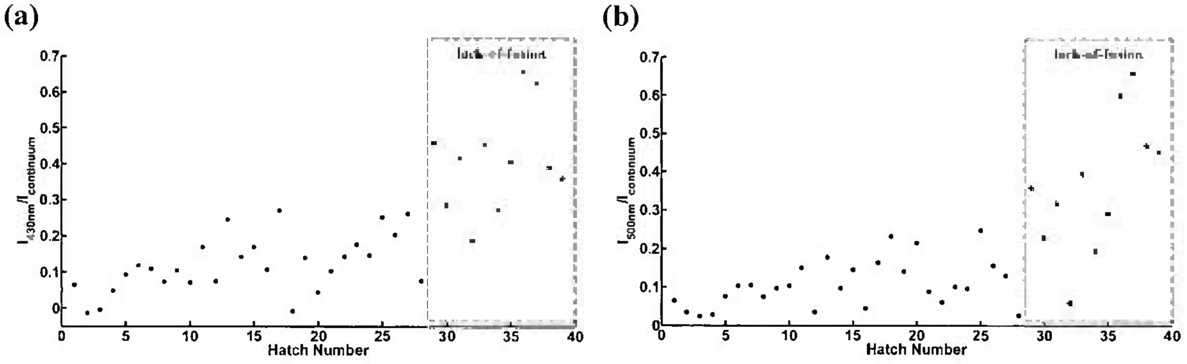

Figure 8: Average line-to-continuum ratio, around (a) 550 nm and (b) 430 nm emission lines, over each hatch of layer 30.

4. Discussion and Concluding Remarks

Observed optical emission from excited or ionized gases above a substrate are influenced by many factors, including present atomic and molecular species, species concentration, ion, electron and excitation temperatures, and the optical thickness of the plume. These factors are in turn influenced by how the laser interacts with the melt pool, how and which species are vaporized, and interactions of the laser beam with emitted species and with atmospheric gases. Thus, fluctuations in melt pool dynamics or in the surrounding substrate temperature—for example, due to localized heating of an insulated defect—affect the characteristics of excited and ionized gases above the substrate. Given this, optical emission of excited gases and plasma may serve as a proxy for monitoring weld pool, surface, and subsurface conditions during additive manufacturing.

Our results indicate that defects formed as a result of improper parameter section, and possibly melt pool instability, correlated with increased and fluctuating line emissions from excited gases above the melt pool. In the experiments described here, Ti-6Al-4V was deposited atop a Ti-6Al-4V substrate. The line-to-continuum ratio of Ti I emissions around 430 nm and 550 nm were found to correlate with defect locations. Over defect-containing regions, the line-to-continuum ratio fluctuated from hatch to hatch; this may be indicative of instabilities within the excited gases above melt pool during deposition.

Based on this work, we argue that optical emissions sensors may be used for monitoring lack-of-fusion defects between hatches, and instabilities during the additive manufacturing of metals. The extent to which this technique can be applied to monitoring of lack-of-fusion between layers is being explored. Work is also ongoing to explore the potential of applying high-speed camera imaging, photodiodes, and custom-built spectrometers to further explore the line-to-continuum ratio technique, described here, for defect detection. Applications to other metallic systems and other AM processes are also being explored.

Acknowledgements

The authors acknowledge Dr. David B. Saint John and Mr. Griffin T. Jones for performing computed topography scans of processed samples and Mr. Ed A. Good for help with metallography. This work was supported by the Office of Naval Research, under Contract No. N00014-11-1-0668. Any opinions, findings and conclusions or recommendations expressed in this publication are those of the authors and do not necessarily reflect the views of the Office of Naval Research.

References

[1] W. M. Steen and J. Mazumder, “Laser Automation and In-process Sensing,” in *Laser Material Processing*, Springer London, 2010, pp. 485–518.

[2] M. R. Boddu, R. G. Landers, and F. W. Liou, “Control of laser cladding for rapid prototyping—A review,” in *Solid freeform fabrication symposium Proceedings*, 2001, pp. 6–8.

[3] E. W. Reutzel and A. R. Nassar, "A review of sensing and control for metal-based additive manufacturing," in *Solid Freeform Fabrication Proceedings*, Austin, TX. (submitted), 2014.

[4] A. Sun, E. Kannatey-Asibu Jr, and M. Gartner, "Sensor systems for real-time monitoring of laser weld quality," *J. Laser Appl.*, vol. 11, no. 4, pp. 153–168, 1999.

[5] J. R. Araujo, J. J. Rodriguez-Andina, J. Farina, F. Vidal, J. L. Mato, and M. A. Montealegre, "FPGA-based laser cladding system with increased robustness to optical defects," in *IECON 2012-38th Annual Conference on IEEE Industrial Electronics Society*, 2012, pp. 4688–4693.

[6] J.-P. Kruth, P. Mercelis, J. Van Vaerenbergh, and T. Craeghs, "Feedback control of selective laser melting," in *Proceedings of the 3rd International Conference on Advanced Research in Virtual and Rapid Prototyping*, 2007, pp. 521–527.

[7] G. Bi, B. Schürmann, A. Gasser, K. Wissenbach, and R. Poprawe, "Development and qualification of a novel laser-cladding head with integrated sensors," *Int. J. Mach. Tools Manuf.*, vol. 47, no. 3–4, pp. 555–561, Mar. 2007.

[8] J. T. Hofman, B. Pathiraj, J. van Dijk, D. F. de Lange, and J. Meijer, "A camera based feedback control strategy for the laser cladding process," *J. Mater. Process. Technol.*, vol. 212, no. 11, pp. 2455–2462, Nov. 2012.

[9] D. Hu, H. Mei, and R. Kovacevic, "Closed loop control of 3d laser cladding based on infrared sensing," in *Solid Freeform Fabrication Proceedings*, 2001, pp. 129–137.

[10] G. Bi, A. Gasser, K. Wissenbach, A. Drenker, and R. Poprawe, "Identification and qualification of temperature signal for monitoring and control in laser cladding," *Opt. Lasers Eng.*, vol. 44, no. 12, pp. 1348–1359, Dec. 2006.

[11] L. Song and J. Mazumder, "Feedback control of melt pool temperature during laser cladding process," *Control Syst. Technol. IEEE Trans. On*, vol. 19, no. 6, pp. 1349–1356, 2011.

[12] D. P. Hand, M. D. T. Fox, F. M. Haran, C. Peters, S. A. Morgan, M. A. McLean, W. M. Steen, and J. D. C. Jones, "Optical focus control system for laser welding and direct casting," *Opt. Lasers Eng.*, vol. 34, no. 4, pp. 415–427, 2000.

[13] A. Fathi, A. Khajepour, E. Toyserkani, and M. Durali, "Clad height control in laser solid freeform fabrication using a feedforward PID controller," *Int. J. Adv. Manuf. Technol.*, vol. 35, no. 3–4, pp. 280–292, Oct. 2006.

[14] M. Zeinali and A. Khajepour, "Height Control in Laser Cladding Using Adaptive Sliding Mode Technique: Theory and Experiment," *J. Manuf. Sci. Eng.*, vol. 132, no. 4, p. 041016, 2010.

[15] A. Heralić, A.-K. Christiansson, and B. Lennartson, "Height control of laser metal-wire deposition based on iterative learning control and 3D scanning," *Opt. Lasers Eng.*, vol. 50, no. 9, pp. 1230–1241, Sep. 2012.

[16] L. Song, V. Bagavath-Singh, B. Dutta, and J. Mazumder, "Control of melt pool temperature and deposition height during direct metal deposition process," *Int. J. Adv. Manuf. Technol.*, vol. 58, no. 1–4, pp. 247–256, May 2011.

[17] K. Bartkowiak, "Direct laser deposition process within spectrographic analysis in situ," *Phys. Procedia*, vol. 5, pp. 623–629, Jan. 2010.

[18] L. Song and J. Mazumder, "Real Time Cr Measurement Using Optical Emission Spectroscopy During Direct Metal Deposition Process," *IEEE Sens. J.*, vol. 12, no. 5, pp. 958–964, May 2012.

[19] L. Song, C. Wang, and J. Mazumder, “Identification of phase transformation using optical emission spectroscopy for direct metal deposition process,” 2012, p. 82390G–82390G–9.

[20] A. Ancona, V. Spagnolo, P. M. Lugara, and M. Ferrara, “Optical Sensor for real-time Monitoring of CO< sub> 2</sub> Laser Welding Process,” *Appl. Opt.*, vol. 40, no. 33, pp. 6019–6025, 2001.

[21] T. Sibillano, A. Ancona, V. Berardi, E. Schingaro, G. Basile, and P. Mario Lugarà, “A study of the shielding gas influence on the laser beam welding of AA5083 aluminium alloys by in-process spectroscopic investigation,” *Opt. Lasers Eng.*, vol. 44, no. 10, pp. 1039–1051, Oct. 2006.

[22] M. M. Collur and T. DebRoy, “Emission spectroscopy of plasma during laser welding of AISI 201 stainless steel,” *Metall. Mater. Trans. B*, vol. 20, no. 2, pp. 277–286, 1989.

[23] Z. Szymanski, J. Kurzyna, and W. Kalita, “The spectroscopy of the plasma plume induced during laser welding of stainless steel and titanium,” *J. Phys. Appl. Phys.*, vol. 30, no. 22, p. 3153, 1997.

[24] P. Sforza and D. de Blasiis, “On-line optical monitoring system for arc welding,” *NDT E Int.*, vol. 35, no. 1, pp. 37–43, Jan. 2002.

[25] A. R. Nassar, R. Akarapu, S. M. Copley, and J. A. Todd, “Investigations of laser-sustained plasma and its role in laser nitriding of titanium,” *J. Phys. Appl. Phys.*, vol. 45, no. 18, p. 185401, May 2012.

Appendix 6 – Additive Manufacturing of Ti-6Al-4V Using a Pulsed Laser Beam

Nassar A R, Reutzel E W, Additive Manufacturing of Ti-6Al-4V Using a Pulsed Laser Beam. *Metallurgical and Materials Transactions A*, doi:10.1007/s11661-015-2838-z, 2015.

Additive Manufacturing of Ti-6Al-4V Using a Pulsed Laser Beam

ABDALLA R. NASSAR and EDWARD W. REUTZEL

Microstructural development in directed-energy additive manufacturing of metal components is a complex process that produces parts with materials whose microstructure and properties are influenced by multiple heating and cooling cycles. Much work has been undertaken to correlate microstructural development with processing conditions, such as laser power and processing speed. Here, the microstructure and indentation hardness of a Ti-6Al-4V component processed with a pulsing laser beam and a continuous wave (CW) laser beam are investigated. It is found that the pulsed-beam build showed no statistically significant variation in lath width or indentation hardness with build height while the build deposited with the CW beam showed a statistically significant decrease in hardness and an increase in lath width near the middle of the build. The reduction in variability with beam pulsing is attributed to rapid cooling rates within the melt pool, a greater degree of melt pool stirring, and reduced aging during part build-up.

DOI: 10.1007/s11661-015-2838-z
© The Minerals, Metals & Materials Society and ASM International 2015

I. INTRODUCTION

ADDITIVE manufacturing (AM) of metal components has gained much attention in recent years, with metal-based AM machine sales increasing by 75 pct from 2012 to 2013.[1] This can, in part, be attributed to the ability to rapidly produce high-value components directly from a digital CAD model. Metal components are commonly built using one of two methods: powder-bed fusion or directed-energy deposition.[2] In the former, a laser or electron beam is scanned over a bed of powder; while in the latter, powder is blown or wire is fed into the melt pool formed by a laser or electron beam. In both cases, parts are built up layer-by-layer.

Though processing itself is straight-forward, the resulting internal part microstructure can be complex and non-uniform. Parts produced using AM undergo multiple, complex thermal cycles which can result in internal variations in microstructure and properties. Such intra-build variations have been observed to depend on part orientation, part size, and the scanning pattern used for part build-up. Intra-build variations have been witnessed in both powder-bed and directed-energy processes.

Of particular interest is the study of intra-build variations in AM-produced titanium alloy titanium-6 pct aluminum-4 pct vanadium (Ti-6Al-4V) components. This alloy, also known as Grade 5 titanium, is favored in biomedical, aerospace, and defense application, due to its non-toxicity, low weight, high strength-to-density ratio, and low creep at high temperatures. Within Ti-6Al-4V, microstructural variation is characterized by the size, shape, orientation, and ratio of the α- and β-phases, prior-beta grain structure, as well as the existence of the diffusionlessly transformed α' phase. Details of microstructural features can be correlated to the mechanical properties of Ti-6Al-4V.[3] Typically, the microstructure of additively manufactured Ti-6Al-4V components consists of Widmanstätten α-β, with β present between narrow α-laths, and large, columnar, prior-beta grains extending from the bottom to the top of builds.[4]

A. *Intra-build Variations in AM of Ti-6Al-4V*

Intra-build variations, such as a transition from a Widmanstätten to a martensitic α' microstructure, have been observed to occur near the top surface of parts produced using the Arcam, powder-bed, electron-beam-melting (EBM) process.[4] Also using EBM, Murr *et al.*[5] reported a 1.5 to 2 times increase in α-lath width from the bottom to the top of a 6.8-cm tall, cylindrical build—measurements were made 1 cm from the bottom and 1 cm from the top of the build. Alpha-lath widths have also been reported to vary from interior to exterior build locations along the same build height.[6]

Variations in microstructure have also been observed in the directed-energy, laser engineered net shaping (LENS®) process. Qian *et al.* reported that the α-lath width was larger in the middle than at the bottom or top of single-wall builds.[7] Using a powder-blown, directed-energy deposition (DED) process, similar to LENS but with much higher power (11 kW rather than ~500 W in the case of Reference 7), Kelly and Kemp[8] also observed smaller α-laths near the top of a single-wall build and a grading of α-lath widths within each deposited layer. They argued that layer bands (dark, periodic lines perpendicular to the build direction) were due to a change in morphology from a Widmanstätten α to a colony α morphology, caused by a slow cooling rate from above the β transus temperature. They further

---

ABDALLA R. NASSAR, Research Associate, and EDWARD W. REUTZEL, Head of Laser System Engineering & Integration Department, are with the Applied Research Laboratory, The Pennsylvania State University, University Park, PA 16804. Contact e-mail: arn5000@psu.edu

Manuscript submitted October 9, 2014.

Published online: 13 March 2015

argue, and present a numerical model[9] as further evidence that this banding occurs, not during the deposition of the layer on which it is observed, but as a result of reheating of buried layers during deposition of subsequent layers above the α dissolution temperature—the temperature in the α-β region where α begins transforming into β—but below the β transus temperature. For this reason, henceforth, these banded features are referred to as reheating bands.

Intra-build variations in the microstructure can be expected to correspond to variations in mechanical properties. Variations in indentation hardness and microstructure within AM builds have been shown across a range of AM processes, ranging from high-deposition-rate, multi-kilowatt-electron-beam-based processes to low-deposition-rate, powder-bed processes.[10] For example, Murr, *et al.*[5] reported that Vickers hardness decreased from the bottom to the top of Ti-6Al-4V builds produced using the ARCAM electron beam melting (EBM) process. Depending on processing conditions, hardness varied from the bottom to the top of build by 0.4 to 1 GPa (30 to 100 HV).[5] Using the same process, Hrabe and Quinn[6] reported a decrease in hardness, from exterior to interior build locations along the same build height, along with a counterintuitive decrease in α-lath thickness.[6] Conversely, using the LENS process to build a single-wall in H13 tool steel, a decrease in hardness from the top surface of the build to the substrate has been reported.[11,12] Variations in mechanical properties, such as strength and ductility, have also been shown to be influenced by part shape and size.[13]

B. *Influence of Beam Modulation*

A comprehensive model linking processing conditions with resulting microstructure and mechanical properties has not yet been developed. However, it is well known that microstructure formation is governed by material temperature, time, thermal gradients, cooling rate, induced stresses, and melt pool dynamics. Given this, variations in beam power can be expected to influence microstructure. Results from investigations of laser, electron beam, and arc-welding support this assertion. Peak power density during laser welding of Ti-6Al-4V has been shown to influence microstructure and hardness.[14] Arc modulation, arc pulsing,[15] and magnetic stirring[16] have also been reported to enhance flow within the melt pools and result in refined grain structures. It is thought that refining may occur though dendrite fragmentation, multiple cycling though the α-β transus, reduced weld-pool thermal gradients, or changes in the direction of the maximum thermal gradient.[17] Sundaresan *et al.*[15] argue that reduced and changing direction of the thermal gradient, through melt pool stirring, are more likely to contribute to grain refinement.

Recently, Mitzner *et al.*[18] investigated beam and arc modulation in electron beam and gas tungsten arc additive manufacturing, respectively. They found that α-lath width was reduced with current modulation; prior-beta grain boundaries became more equiaxe; and, hardness values, as measured in the Y-Z, X-Z, and X-Y planes (where $+Z$ is the build-up direction) became more isotropic with modulation. It should be noted that hardness values were averaged across a cross section in the "steady-state region" taken in each plane. The "steady-state region" was presumably the region near the center of the build.

Here, we investigate the use of laser-beam pulsing as a means to refine part microstructure and to reduce intra-build variations in Ti-6Al-4V builds deposited using a powder-blown DED process. This is done though comparison of two builds, each processed with identical energy input per unit length (average power/speed), but different laser-modulation modes. One build was processed using a continuous wave (CW) beam while the other was processed using a pulsed beam. The macrostructure (Section III–A), microstructure (Section III–B), and indentation hardness profiles (Section III–C) of each are compared and contrasted to understand the effects of laser-beam pulsing.

II. EXPERIMENTAL METHODOLOGY

A. *Physical Setup*

An Optomec LENS MR-7, laser-based, directed-energy-deposition system was used for deposition. The system was equipped with a 500-watt Ytterbium-doped fiber laser (IPG YLR-500-SM) which was focused to a second-moment spot diameter of 0.62 mm at a distance of 20.7 mm above the substrate. Beam size measurements were made using a PRIMES GmbH FocusMonitor. As shown in Figure 1, the laser spot size was 1.24 mm at the working distance, which corresponded to a space of 9.27 mm between the substrate and four, radially symmetrically powder-delivery nozzles. Nozzles had an exit orifice diameter of 1.2 mm and were oriented at 18.25 deg with respect to the laser-beam propagation direction. Centered among the powder nozzles was a 6.35 mm diameter, center-purge nozzle, through which 30 lpm of argon flowed.

During deposition, the substrate was in the X-Y plane while the laser processing head remained stationary. After each layer deposition, the laser head was translated upward (in the $+Z$-direction) by a predefined layer increment.

B. *Materials*

Ti-6Al-4V structures were deposited atop Ti-6Al-4V substrates. Annealed and ground-finished, 3.175 mm thick, substrates were used. Prior to processing, substrates were cleaned with acetone and isopropyl alcohol. Extra low interstitials (ELI)-grade powder was obtained from Phelly, Inc. Mean powder particle size was measured, using a Horiba LA950 particle size distribution analyzer, at 126.8 μm with a standard deviation of 45.94 μm.

C. *Process Parameters*

The processing chamber held an argon atmosphere, with an oxygen concentration below 20 parts per million, and a gauge pressure between 498 and 748 Pa

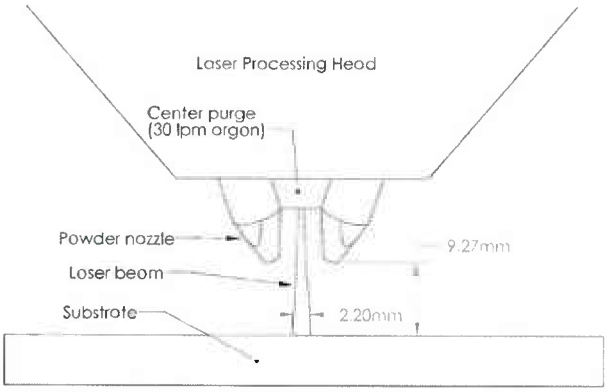

Fig. 1—Physical setup of processing head and laser beam with respect to the substrate.

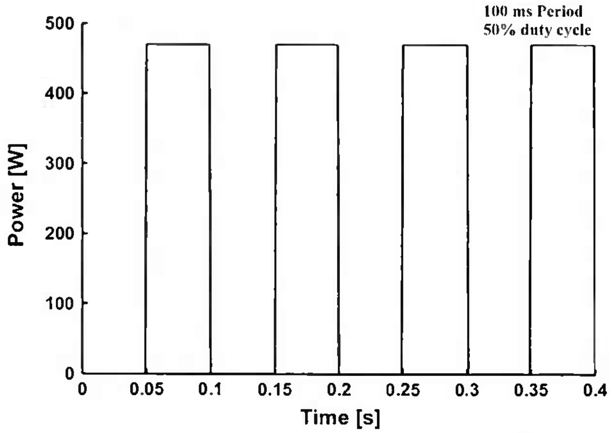

Fig. 2—Laser power in pulsed mode.

(2 to 3 in. of water). The pressure was maintained using a pressure regulator along with inlet flows of argon from the coaxial purge nozzle and the powder-delivery nozzles. Powder flow was measured and maintained at 3 g per minute using a powder feeder assisted by a 4-lpm argon flow.

Builds were deposited in one of two configurations. In the first, the laser was operated in CW mode, at a measured output power of 450 ± 25 W, and a processing speed of 10.58 mm/s (25 in./min). In the second, the laser power was modulated to produce periodic, square waves with a period of 100 ms and a duty cycle of 50 pct. Power as a function of time is plotted in Figure 2. To maintain the same energy input per unit traverse length as in CW mode, the processing speed was reduced to 5.29 mm/s (12.5 in/min) in pulsed mode.

D. *Part Geometry and Build Plan*

A rectangular block, 34.29 mm in length and 12.5 mm in width, with an internally varying hatch spacing was selected for deposition. The block was built-up using a total of 35 layers with layer increment set point of 0.178 mm. It may be noted that the actual build height of each block exceeded the product of the layer increment by the number of layers. This layer increment was intentional set slightly below the anticipated layer thickness to account for, and take advantage of, the self-regulating nature of powder-blown DED.

On each layer, a total of twenty-six parallel hatches were deposited using a back-and-forth raster. The hatch order was reversed from layer to layer. Each hatch was 12.5 mm long, extending along the width of the block. This geometry was selected as part of unrelated work on defect detection, which will not be discussed in this article. For the present study, only the first set of six hatches, spaced center-to-center 0.914 mm apart, are of interest.

E. *Characterization*

Builds were cross-sectioned midway through the width of the part and perpendicular to the hatches. Cross sections were ground and polished according to standard metallographic techniques and drop etched using Krolls reagent. Microstructure was characterized using an optical microscope equipped with a digital camera. Micrographs were captured at each reported build height. Image contrast was enhanced using contrast stretching, and, to correct for non-uniform illumination, contrast-limited adaptive histogram equalization (CLAHE) was applied, as necessary, within the MATLAB (R2014a) software package. Reported alpha-lath widths were manually measured at 35 random locations within each image. Hardness indents were made at each reported build height, near where micrographs were recorded. Vickers hardness was measured using a LECO-M-400-G1 hardness tester using a load of 1 kgf applied for 10 seconds. Each reported hardness value is based on the average of five measurements along each reported build height.

III. RESULTS

A. *Macrostructure*

Polished and etched cross sections of the as-deposited builds are shown in Figure 3. The height of the CW build (Figure 3(a)) peaked around the third hatch at a height of 9.93 mm whereas the height of the pulsed-beam build (Figure 3(b)) peaked around the second hatch at a height of 9.65 mm.

Cross sections of both builds were characterized by columnar prior-β grain boundaries. The prior-β grains were on the order of a millimeter in width and extended several millimeters from the bottom of the build (above the heat-affected zone (HAZ)) to the top of the deposit. Approximately, seven prior-beta grains were present across the first six hatches of the CW build while eight prior-beta grains spanned across the six hatches of the pulsed-beam build.

Within and across the prior-beta grains, reheating bands were distinguished as dark regions extending

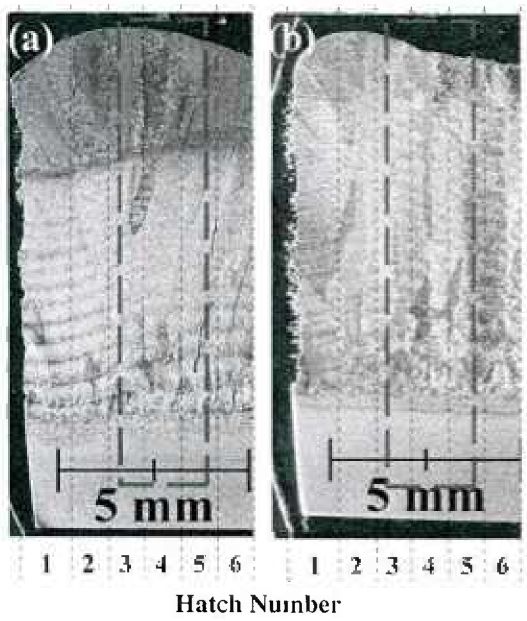

Fig. 3—Macrostructure of build deposited using (*a*) CW laser and (*b*) pulsed laser beam. Gray, dashed boxes indicate locations of hardness indents.

horizontally though the cross sections. In the case of CW build, layer bands were not observed 2.5 to 3.5 mm from the top surface of the build. In the case of the pulsed-beam build, reheating bands extended nearly to its top surface.

B. *Microstructure*

The microstructure of both the CW and pulsed-beam builds were characterized by thin α-laths oriented in a Widmanstätten basket-weave pattern. High-magnification micrographs are shown at several build heights for the CW build in Figure 4 and for the pulsed-beam build in Figure 5.

The primary distinction between the builds is the size of α-laths. Alpha-laths in CW build (Figure 4) were wider than in the pulsed-beam build (Figure 5). In the CW build, α-laths also varied in size with build height, appearing widest near the middle of the build (Figure 4(c)) and narrowest near the top (Figure 4(f)). In contrast to this, α-laths in the pulsed-beam build appeared similar irrespective of build height.

Measurements of the α-lath widths, using the micrographs in Figures 4 and 5, confirmed that α-lath widths varied significantly with build height in the CW build but not in the pulsed-beam build. The widths of α-laths as a function of distance from the top surface, for both builds, are shown as box plots in Figure 6. Near the top of the CW build, 1.5 mm from the top surface, the α-lath width was 0.78 μm. It then peaked at a distance of 5.5 mm from the top surface, reaching 1.54 μm, before falling to 1.27 μm at 9.5 mm from the top surface, near the substrate. In the pulsed-beam build, the α-lath width averaged near 0.62 μm at all locations (within $+0.08/-0.04$ μm).

An analysis of variance (ANOVA), assuming a 95 pct confidence interval, showed that in the CW deposit there was a statistically significant variation of lath width with build height. The ANOVA p value was 1.12×10^{-20}. In contrast to this, the pulsed-beam build showed no significant variation in lath width with build height (p value of 0.142).

Possible differences in α-lath widths within and between reheating bands were also tested for statistical significance. Figure 7 juxtaposes micrographs taken at reheating band locations with those taken outside the banded region at a nearby location. The micrographs were taken approximately 6.5 mm from the top surface of the CW build and 4.5 mm from the top surface of the pulsed-beam build. Diffuse illumination was used in Figure 7, α appears black while inter-granular β appears white.

In both the CW and pulsed-beam builds, statistically significant differences were found in mean α-lath width within compared to between reheating bands. In the CW build, within the banded region the α-lath width averaged 1.0 μm (stdev = 0.22). Between the banded region, the lath width was larger, averaging 1.22 μm (stdev = 0.30 μm). Although differences were within one standard deviation, an unpaired t test p value of 0.0014 established that the difference was statistically significant. Within the pulsed-beam build, α-lath width averaged 0.52 μm (Stdev = 0.10 μm) within the banded region and 0.61 μm (Stdev = 0.16 μm) between the banded region. As in the CW build, the difference in mean values was within one standard deviation but statistically significant (unpaired t test p value = 0.0056).

Qualitatively, it also appeared that regions within the darker, reheating bands contained more aligned α-platelets, known as colony alpha, than regions outside the bands—quantitative measurement was not attempted. If true, this is in agreement with the observations of Kelly and Kemp.[8] The higher percentage of colony α within reheating bands may be responsible for their darker appearance under diffuse lighting. That is, light is preferentially scattered along specific directions from aligned plates, resulting in a darker appearance when the direction of scattering was not toward the observer. Between reheating bands, the orientation of alpha platelets may be more random resulting in light being scattered more uniformly.

C. *Indentation Hardness*

Vickers hardness was measured starting at 0.5 mm for the top of each build to the substrate, at 1 mm increments. At each height increment, five hardness measurements were recorded. Results are shown as box plots in Figure 8. An ANOVA analysis of hardness showed that, from 0.5 to 8.5 mm below the surface of the CW build, there was a statically significant variations in hardness with distance (p = 0.0057). In the CW build, hardness was highest near the top surface; at 0.5

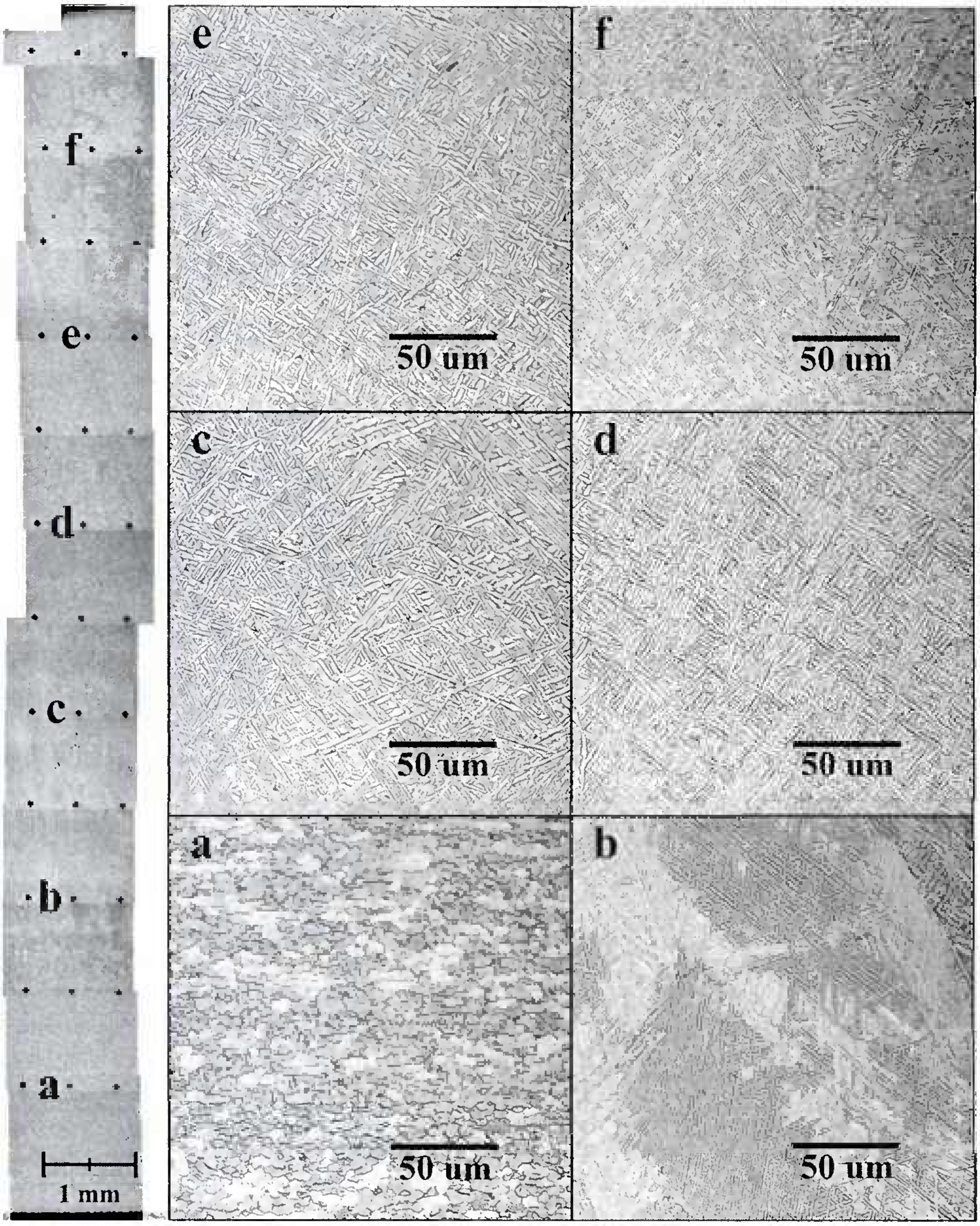

Fig. 4—Micrographs of the build processed using a CW laser beam. High-magnification images are shown for the locations indicated on the left-hand-side of the figure.

and 2.5 mm from the top surface, hardness peaked at 319 and 321 HV, respectively. Hardness was lowest in the middle of the build; at 5.5 mm from the top surface hardness dropped to 299 HV. Hardness increased from the middle of the build to the substrate until reaching the substrate hardness of 326 HV.

For the pulsed-beam build, there were no significant changes in hardness values with distance ($p = 0.37$) from 0.5 to 7.5 mm below the top surface. Hardness was highest 0.5 mm from the top surface at 342 HV. However, average hardness from 0.5 to 7.5 mm below the substrate surface was within $+5/-4$ HV of 337 HV. Near the bottom of the build, at 8.5 mm from the top surface, average hardness increased to 352 HV before falling to the substrate hardness of 326 HV.

IV. DISCUSSION

A. *Macrostructure*

The macrostructure was characterized by columnar prior-beta grains and visible reheating bands. The formation of elongated prior-β grains extending from the bottom to the top surface of the build is commonplace in AM builds. Their formation is attributed to epitaxial growth on each successive layer, which was

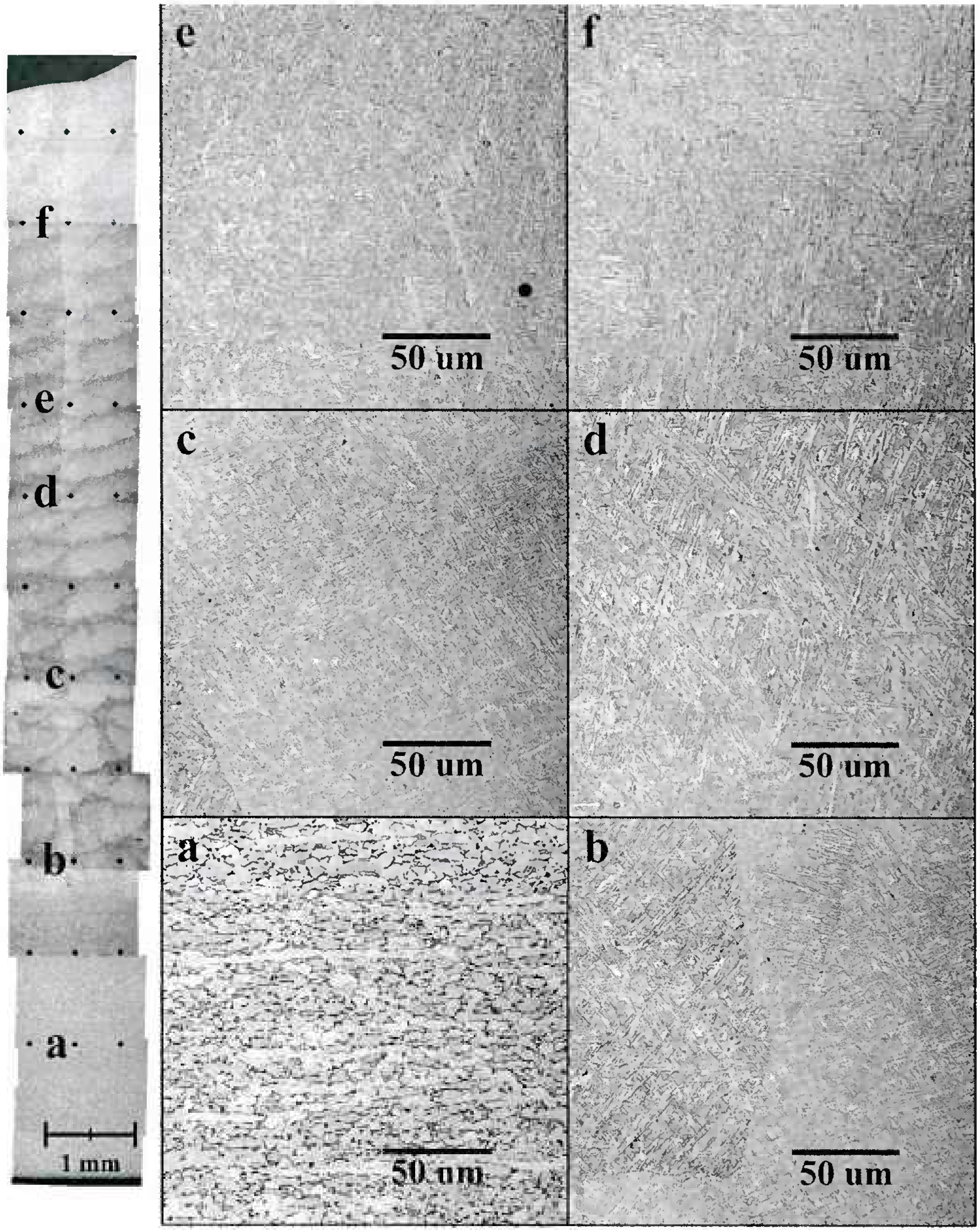

Fig. 5—Micrographs of the build processed using a pulsed laser beam. High-magnification images are shown for the locations indicated on the left-hand-side of the figure.

parallel to the heat gradient—see References 4, 19 for discussions regarding the formation and evolution of prior-β in additively manufactured Ti-6Al-4V. Laser-beam pulsing had no apparent effect on the epitaxial growth of the grains or their orientation.

Pulsing did, however, influence the shape of reheating bands (evident in Figures 4 and 5). In the case of the CW build, bands continued from hatch to hatch across the length of the build. In the pulsed-beam build, bands were semi-circular and overlapping from hatch to hatch. This reaffirms Kelly and Kemps findings[8,9] that banding does not occur during the deposition of the layer on which it is observed, but rather result from reheating a buried layers above the α dissolution temperature during the deposition of subsequent layers. Given this and the observation that bands were observed nearly to the top of the pulsed-beam build, we conclude that reheating of buried layers was reduced in the pulsed-beam deposited build.

One factor which contributed to reduce reheating of buried layers in the pulsed-beam build is total deposition time. Although the energy input per unit traverse length was identical for both builds, the total deposition time was doubled for the pulsed-beam build. Given the difference in total deposition time, and identical total energy input (assuming the laser absorption for both

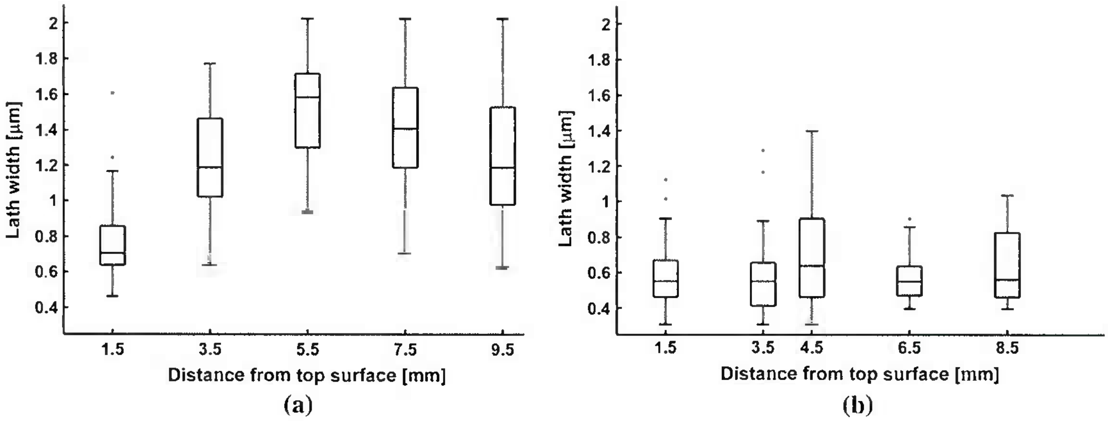

Fig. 6—Box plot of α-lath widths. The center, horizontal line within each box is the median, box edges represent the 25th and 75th percentiles, whiskers represent the range of data points considered. Individual points represent outliers.

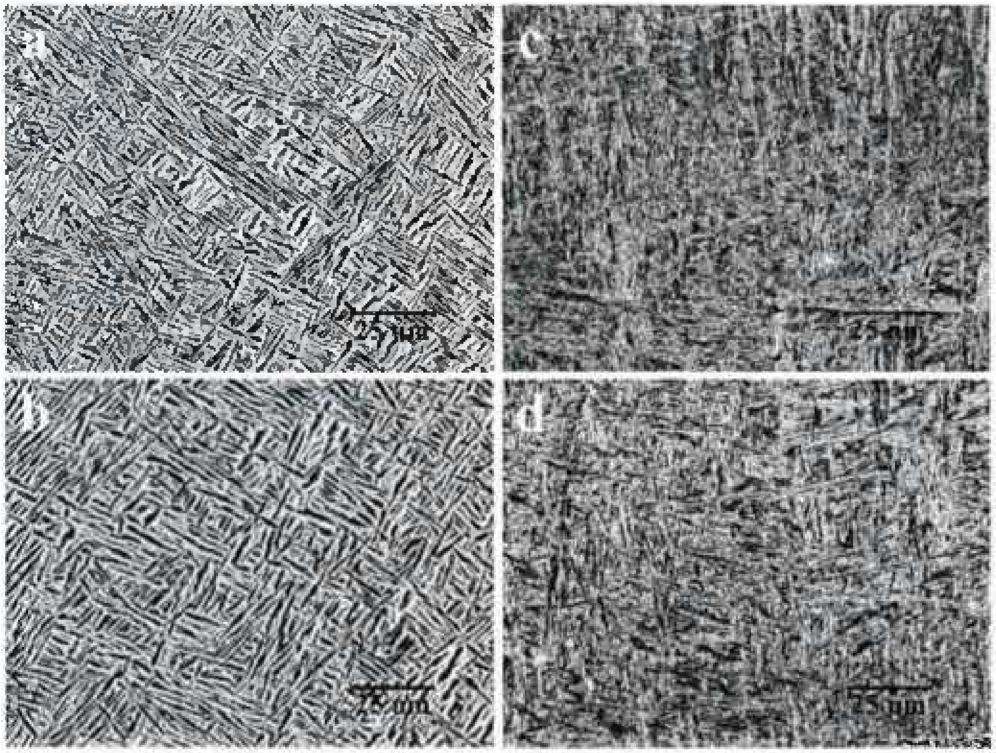

Fig. 7—Microstructure within a banded region (*a*, *c*) and in a region between reheating bands (*b*, *d*). Images to the left (a, b) show the microstructure for the CW AM build while those on the right (c, d) were taken from the pulsed AM build.

processes were equal), the pulsed-beam build was cooler. This may also be a factor in the reduced total build height of the pulsed-beam build (9.65 mm) compared with the CW build (9.93 mm) by affecting melt pool size and hence powder capture efficiency.

B. *Microstructure*

Beam pulsing strongly affected the width of α-laths. Within the CW build, α-laths were approximately 1.3 to 2.5 times wider than in the pulsed-beam build. In addition to being thinner, α-lath widths were also more uniform throughout the pulsed-beam build. It is well known that the size and orientation of grains within a molten pool are controlled by solidification parameters: growth rate (R), thermal gradient (G), and undercooling (ΔT). In CW processes, the growth rate is defined by the weld-pool geometry and traversing speed. Since the solidification front cannot move faster than the traveling speed of the laser, the growth rate is always below the welding speed. The cooling rate (dT/dt) is the product of GR.

For CW processes, the cooling rate at the center line of a weld can be approximated using the Rosenthal solution (Eq. [1]).[20] Using a speed, v, of 10.58 mm/s, a

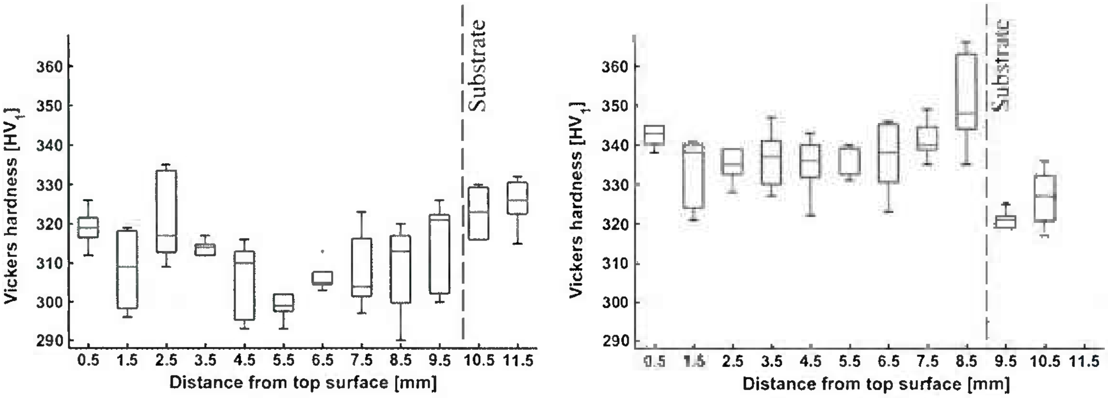

(a)

(b)

Fig. 8—Box plot of hardness data on (*a*) CW processed build and (*b*) pulsed-beam deposited build.

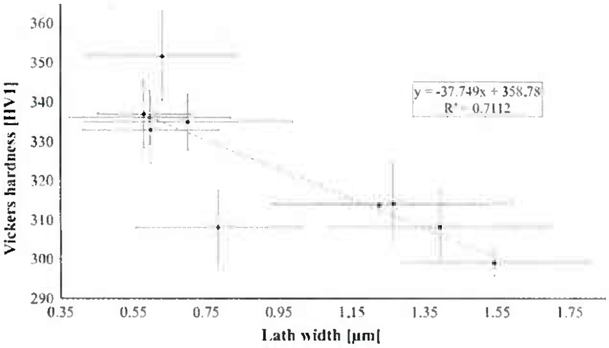

Fig. 9—All measured lath widths and Vickers hardness values. A linear model explains 71 pct of the variation in hardness with α-lath width.

thermal conductivity, k, of 6.7 W/mK, an absorption coefficient, α, of 0.4, a power, Q, of 450 W, a solidus temperature, T, of 1877 K (1604 °C), and room temperature, T_0, of 293 K (20 °C), the cooling rate at the center line was approximately 6.2×10^3 K/s.

$$\frac{dT}{dt} = -2\pi k \frac{v}{\alpha Q}(T - T_0)^2. \qquad [1]$$

During pulsed-beam processing, cooling rates are determined by multiple melting and solidification cycles. Cooling rates are expected to be higher than in CW processing, but their estimation requires numerical simulation.[21] Higher cooling rates in the case of pulsed-beam processing may explain the finer microstructure within the pulsed-beam build. Another contributing factor may be stirring within the melt pool due to laser pulsing. If the solidification rate was such that the melt pool remained molten between laser pulses, laser pulsing would have induced melt flow due to fluctuating vapor pressure and melt temperatures. This stirring within the melt pool, as in the case of arc modulation,[15] and magnetic stirring[16] in arc-welding, likely contributed to the observed grain refinement within the pulsed-beam build, compared to the CW build.

According to Ahmed and Rack,[22] cooling rates above 410 K/s should result in a $\beta \rightarrow \alpha'$ transformation in Ti-6Al-4V upon solidification. Given this, the microstructures in both the CW and pulsed-beam build should have been fully martensitic upon solidification. However, following solidification, the microstructure in both builds continued to be affected by heating and cooling cycles due to subsequent deposition paths. These thermal cycles resulted in aging and likely resulted in decomposition of martensitic α', formed upon initial solidification. Multiple heating and cooling cycles in AM builds have also been shown by others to result in the growth of alpha grains and the formation of reheating bands.[8,9] This mechanism, coupled with changing thermal conditions as the build progressed, was likely responsible for the non-uniformity in α-lath widths and microhardness observed in the CW build. Given that there was less variation in α-lath widths and microhardness in the pulsed-beam build, it is concluded that aging effects were reduced and microstructure was made more homogeneous throughout the build as a result of pulsed-beam processing.

C. *Indentation Hardness*

Measured indentation hardness followed similar trends to α-lath widths in both builds. This is not surprising given that mechanical properties of Ti-6Al-4V have been shown to be a function of α-lath width. For example, it has been shown that yield strength of AM build correlates linearly with (alpha-lath width)$^{-0.5}$.[4] A reduction in alpha-lath width is thus expected to result in higher indentation hardness values. A plot of measured hardness values (for both builds) as a function of lath widths is given in Figure 9. A linear model explains 71 pct of the variation (correlation coefficient $R = -0.84$) in hardness with α-lath width.

V. CONCLUSIONS

The microstructure and indentation hardness of two directed-energy AM builds deposited on an Optomec

LENS system were compared. Each was processed with identical energy input per unit length but using a laser operating in CW or pulsed-beam mode. The CW build exhibited a statically significant variation in α-lath widths and indentation hardness with build height. In contrast to this, the pulsed-beam build produced finer α-laths, was harder, and had no statistically significant variation in α-lath widths or indentation hardness with build height.

The smaller and more uniform α-lath widths in the pulsed-beam build were due to rapid cooling within the melt pool, possibly a greater degree of melt pool stirring, and reduced thermal aging. Understanding the impact of each of these factors will require numerical simulation of melt pool dynamics and microstructural evolution during processing. This work suggests that pulsed-beam AM may be useful in forming builds with refined microstructures and uniform microstructure and mechanical properties.

ACKNOWLEDGMENTS

We acknowledge Edward A. Good for assistance in preparing metallographic samples. Funding for this work was provided by the Office of Naval Research, under Contract No. N00014-11-1-0668.

REFERENCES

1. Terry T Wohlers and Wohlers Associates: Wohlers Report 2014: Additive Manufacturing and 3D Printing State of the Industry: Annual Worldwide Progress Report, Wohlers Associates, Fort Collins, Colorado, 2014.
2. ASTM F42 Committee: Terminology for Additive Manufacturing Technologies, ASTM International, West Conshohocken, 2012.
3. G. Lütjering: *Mater. Sci. Eng. A*, 1998, vol. 243, pp. 32–45.
4. S.S. Al-Bermani, M.L. Blackmore, W. Zhang, and I. Todd: *Metall. Mater. Trans. A*, 2010, vol. 41A. pp. 3422–34.
5. L.E. Murr, E.V. Esquivel, S.A. Quinones, S.M. Gaytan, M.I. Lopez, E.Y. Martinez, F. Medina, D.H. Hernandez, E. Martinez, J.L. Martinez, S.W. Stafford, D.K. Brown, T. Hoppe, W. Meyers, U. Lindhe, and R.B. Wicker: *Mater. Charact.*, 2009, vol. 60, pp. 96–105.
6. N. Hrabe and T. Quinn: *Mater. Sci. Eng. A*, 2013, vol. 573, pp. 271–77.
7. L. Qian, J. Mei, J. Liang, and X. Wu: *Mater. Sci. Technol.*, 2005, vol. 21, pp. 597–605.
8. S.M. Kelly and S.L. Kampe: *Metall. Mater. Trans. A*, 2004, vol. 35A, pp. 1861–67.
9. S.M. Kelly and S.L. Kampe: *Metall. Mater. Trans. A*, 2004, vol. 35A, pp. 1869–79.
10. S. Lathabai, M. Glenn, C. MacRae, and D. Ritchie: *Aeromat 25 Conf. Expo. Am. Soc. Met.*, Orlando, FL, 2014.
11. M. Griffith, M.E. Schlienger, L.D. Harwell, M.S. Oliver, M.D. Baldwin, M.T. Ensz, and D.V. Nelson: *Solid Free. Fabr. Symp. Proc.*, Austin, TX, 1998.
12. J. Brooks, C. Robino, T. Headley, S. Good, and M. Griffith: *Proc. Solid Free. Fabr. Symp.*, Austin, TX, 1999, pp. 375–82.
13. R.S. Kircher, A.M. Christensen, and K.W. Wurth: *Solid Free. Fabr. Proc.*, Austin, TX, 2009, pp. 398–405.
14. F. Ghaini, M. Hamedi, M. Torkamany, and J. Sabbaghzadeh: *Scripta Mater.*, 2007, vol. 56, pp. 955–58.
15. S. Sundaresan, G.D. Janaki Ram, and G. Madhusudhan Reddy: *Mater. Sci. Eng. A*, 1999, vol. 262, pp. 88–100.
16. M. Malinowski-Brodnicka, G. Den Ouden, and W.J.P. Vink: *Weld. J*, 1990, vol. 69, pp. 52s–59s.
17. G. Madhusudhan Reddy, Amol.A. Gokhale, and K. Prasad Rao: *J. Mater. Sci.*, 1997, vol. 32, pp. 4117–26.
18. S. Mitzner, S. Liu, M. Domack, and R. Hafley: *Solid Free. Fabr. Proc.*, Austin, TX, 2012, pp. 536–55.
19. A.A. Antonysamy, J. Meyer, and P.B. Prangnell: *Mater. Charact.*, 2013, vol. 84. pp. 153–168.
20. Daniel. Rosenthal: *Trans. Am. Soc. Mech. Eng.*, 1946, vol. 48, pp. 849–65.
21. T. Zacharia, S.A. David, J.M. Vitek, and T. DebRoy: *Metall. Trans. A*, 1989, vol. 20A, pp. 957–67.
22. T. Ahmed and H.J. Rack: *Mater. Sci. Eng. A*, 1998, vol. 243, pp. 206–11.

Appendix 7 – Thermo-mechanical model development and validation of directed energy deposition additive manufacturing of Ti–6Al–4V

Heigel J C, Michaleris P, Reutzel E W, Thermo-mechanical model development and validation of directed energy deposition additive manufacturing of Ti–6Al–4V, *Additive Manufacturing,* 5, 9–19, doi: 10.1016/j.addma.2014.10.003, 2015.

Available online at www.sciencedirect.com
ScienceDirect
ELSEVIER
Additive Manufacturing xxx (2014) xxx–xxx
Additive MANUFACTURING
www.elsevier.com/locate/addma

Thermo-mechanical model development and validation of directed energy deposition additive manufacturing of Ti–6Al–4V

J.C. Heigel[a,*], P. Michaleris[a,1], E.W. Reutzel[b]

[a] Department of Mechanical and Nuclear Engineering, The Pennsylvania State University, United States
[b] Applied Research Laboratory at The Pennsylvania State University, United States

Accepted 9 October 2014

Abstract

A thermo-mechanical model of directed energy deposition additive manufacturing of Ti–6Al–4V is developed using measurements of the surface convection generated by gasses flowing during the deposition. In directed energy deposition, material is injected into a melt pool that is traversed to fill in a cross-section of a part, building it layer-by-layer. This creates large thermal gradients that generate plastic deformation and residual stresses. Finite element analysis (FEA) is often used to study these phenomena using simple assumptions of the surface convection. This work proposes that a detailed knowledge of the surface heat transfer is required to produce more accurate FEA results. The surface convection generated by the deposition process is measured and implemented in the thermo-mechanical model. Three depositions with different geometries and dwell times are used to validate the model using *in situ* measurements of the temperature and deflection as well as post-process measurements of the residual stress. An additional model is developed using the assumption of free convection on all surfaces. The results show that a measurement-based convection model is required to produce accurate simulation results.

© 2014 Elsevier B.V. All rights reserved.

Keywords: Additive manufacturing; Finite element analysis; Convection model; *In situ* measurements; Residual stress

1. Introduction

Directed energy deposition (DED) [1] is an additive manufacturing process that creates parts through the layer-by-layer addition of material. DED uses a high intensity energy source, such as a laser, to create a melt pool into which metal powder or wire is injected. The melt pool follows a pattern to fill each layer, progressively building the part. Several processes are included in this standard classification, such as laser powder forming, laser engineered net shaping (LENS), direct metal deposition, and laser consolidation. The resulting complex thermal history influences the microstructure, material properties, residual stress, and distortion of the final part. In an effort to understand these phenomena, many researchers have used finite element analysis (FEA) to model the DED process and study its effects on the part [2–17].

FEA modeling of DED is inspired by weld modeling, since it is a similar process that has been studied extensively [18–20]. Although many of the weld modeling studies are directly applicable to DED modeling efforts, the convection models used are not applicable. Some weld studies have achieved useful results by neglecting convection while others have applied free convection uniformly on all exposed surfaces. These approaches lead to small errors in weld modeling because of the small amount of filler material relative to the substrate, which allows most of the heat to be conducted away from the bead into the parts being joined. In contrast, filler material makes up the majority of a part built using DED, resulting in longer processing times and higher temperatures that allow for a greater amount of heat loss through convection. Consequently, greater errors can occur from inaccurate convection models in DED simulations. Complex convection models are required because of the inert gas jets often used to protect the laser optics, to shield the molten material from oxidation, and to aid in delivering powder to the melt

---

[*] Corresponding author. Tel.: +1 8148633245.
E-mail address: jch252@psu.edu (J.C. Heigel).
[1] President of Pan Computing LLC.

http://dx.doi.org/10.1016/j.addma.2014.10.003
2214-8604/© 2014 Elsevier B.V. All rights reserved.

pool. The heat transfer literature demonstrates that these types of jets create localized forced convection that is influenced by a variety of factors [21–23].

The literature shows inconsistent implementation of convection in DED models. Heat loss due to convection is assumed negligible and excluded in some models [24–27]. Convection is incorporated in other models by assuming it is uniformly distributed over all surfaces and equal to free convection in air ($\simeq$10 W/m^2/°C) [5,6,10,28–33] while others have applied a higher uniform convection [34,35], presumably to account for the greater amount of surface convection caused by the inert gas jets. Some researchers have considered the complexity of forced convection when modeling DED. Ghosh and Choi used the empirical equation defined by Gardon and Cobonque [36] to account for the forced convection [37]. Zekovic and co-workers included forced convection when modeling a thin wall deposition by using computational fluid dynamics (CFD) to calculate the convection acting on the surface [8]. However, there was no experimental effort to validate the CFD results for their process. Furthermore, no work has been found in the literature that develops a measurement-based forced convection model.

This work proposes that measurement-based convection is a necessary component in an accurate model of the DED process. To demonstrate this, a thermo-mechanical model for DED of Ti–6Al–4V is developed that implements measurements of the convection generated by an Optomec® LENS system. The thermo-mechanical model is validated using *in situ* temperature and deflection measurements, as well as post-process measurements of the residual stress of three different depositions with varying geometry and dwell times. An additional convection model that assumes free convection is developed to illustrate the importance of implementing forced convection in the thermo-mechanical model.

2. DED simulation

2.1. Thermal model

The DED process is simulated by first solving the thermal history of the process using a three dimensional transient thermal analysis [17]. The governing heat transfer energy balance is written as:

$$\rho C_\mathrm{p}\frac{dT}{dt} = -\nabla\cdot\mathbf{q}(\mathbf{r},t) + Q(\mathbf{r},t) \tag{1}$$

where ρ is the material density, C_p is the specific heat capacity, T is the temperature, t is the time, Q is the heat source, $\mathbf{r}$ is the relative reference coordinate, and $\mathbf{q}$ is the heat flux vector, calculated as:

$$\mathbf{q} = -k\nabla T \tag{2}$$

where k is the thermal conductivity of the material.

Table 1
Temperature dependent thermal and mechanical properties of Ti–6Al–4V [38,15].

T (°C)	k (W/m/°C)	C_p (J/kg/°C)	E (GPa)	$\boldsymbol{\sigma}_y$ (MPa)	α (μm/m/°C)
20	6.6	565	103.95	768.15	8.64
93	7.3	565	100.10	735.30	8.82
205	9.1	574	94.19	684.90	9.09
250	9.7	586	91.81	664.65	9.20
315	10.6	603	88.38	635.40	9.33
425	12.6	649	82.58	585.90	9.55
500	13.9	682	78.63	552.15	9.70
540	14.6	699	76.52	534.15	9.70
650	17.5	770	70.72	484.65	9.70
760	17.5	858	64.91	435.15	9.70
800	17.5	895	62.80	417.15	9.70
870	17.5	959	62.80	417.15	9.70

Table 1 presents the temperature dependent thermal properties for Ti–6Al–4V [38]. Linear interpolation is used to calculate the properties at temperatures between those in the tables. At temperatures above 870 °C, the thermal properties are assumed to be constant. The density of Ti–6Al–4V (4.43 × 10^3 kg/m^3) is assumed to be independent of temperature. The latent heat of fusion is 365 kJ/kg and is spread over a temperature range from 1600 °C to 1670 °C [39].

The double ellipsoid model is used to describe the laser heat source [40]:

$$Q = \frac{6\sqrt{3}P\eta f}{abc\pi\sqrt{\pi}}e^{-\left[\frac{3x^2}{a^2}+\frac{3y^2}{b^2}+\frac{3(z+v_w t)^2}{c^2}\right]} \tag{3}$$

The laser power is P and the laser absorption efficiency is η. The value for P is based on measurement, as will be discussed in Section 3. The value of η is found using the method of inverse simulation described in Ref. [17] to be 45%. The variables x, y, and z are local coordinates while the remaining variables (f, a, b, and c) define the volume over which the heat source is distributed. The volume is defined such that the heat source is circular with a radius equal to half the deposition track width and applied to a depth of 0.9 mm. This results in a melt pool depth to radius ratio of 0.6, which agrees with the range extracted from cross-sections made by Kummailil using similar processing conditions [41].

Surface heat loss occurs on all free surfaces of the model through convection, q_conv, and radiation, q_rad. The free surfaces of the evolving deposition mesh are included in the analysis. Radiation is defined by the Stefan–Boltzmann law:

$$q_\mathrm{rad} = \varepsilon\sigma({T_s}^4 - {T_\infty}^4) \tag{4}$$

where ε and σ are the surface emissivity and the Stefan–Boltzman constant. Emissivity is temperature independent and equal to 0.54, as in Ref. [17]. The surface temperature and the ambient temperature are represented by T_s and T_∞, respectively. The surface heat loss due to convection is defined by

$$q_\mathrm{conv} = h(T_\mathrm{s} - T_\infty) \tag{5}$$

where h is the coefficient of convection.

2.2. Mechanical model

The mechanical response to the thermal history is determined by performing a three dimensional quasi-static incremental

Please cite this article in press as: Heigel JC, et al. Thermo-mechanical model development and validation of directed energy deposition additive manufacturing of Ti-6Al-4V. Addit Manuf (2014), http://dx.doi.org/10.1016/j.addma.2014.10.003

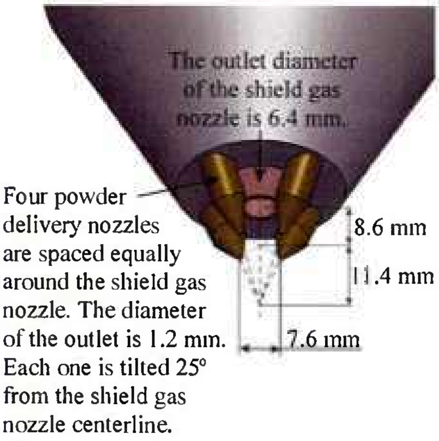
The outlet diameter of the shield gas nozzle is 6.4 mm.
Four powder delivery nozzles are spaced equally around the shield gas nozzle. The diameter of the outlet is 1.2 mm. Each one is tilted 25° from the shield gas nozzle centerline.
8.6 mm
11.4 mm
7.6 mm

Fig. 1. An illustration of the LENS deposition head and powder nozzles.

analysis [17]. The stress equilibrium is governed by the following equation:

$$\nabla \cdot \boldsymbol{\sigma} = 0 \tag{6}$$

where $\boldsymbol{\sigma}$ is the stress. The mechanical constitutive law is defined by:

$$\boldsymbol{\sigma} = C\boldsymbol{\epsilon}_e \tag{7}$$

$$\boldsymbol{\epsilon} = \boldsymbol{\epsilon}_e + \boldsymbol{\epsilon}_p + \boldsymbol{\epsilon}_T \tag{8}$$

C is the fourth order material stiffness tensor. The total, elastic, plastic, and thermal strains are represented by $\boldsymbol{\epsilon}$, $\boldsymbol{\epsilon}_e$, $\boldsymbol{\epsilon}_p$, and $\boldsymbol{\epsilon}_T$.

Table 1 presents the temperature dependent elastic modulus (E), the yield strength ($\boldsymbol{\sigma}_y$), and the coefficient of thermal expansion (α) [38,15]. The mechanical values are assumed to be constant above 800 °C. The Poisons's ratio is assumed to be 0.34 and temperature independent. Perfect plasticity is assumed in the model.

Instantaneous annealing and creep are applied to any element when the average temperature of its Gauss points exceeds the stress relaxation temperature, $T_{\text{relax}} = 690\,^{\circ}\text{C}$. Each strain component in Eq. (8) is set to zero once this criteria is met. Instantaneous stress relaxation at this temperature has been shown by Denlinger and his co-workers to be necessary when modeling the deposition of Ti–6Al–4V [17].

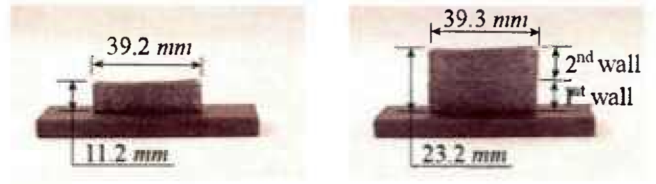

(a) Single wall with no dwell between layers (Case 1)

(b) Double wall with no dwell between layers (Case 2)

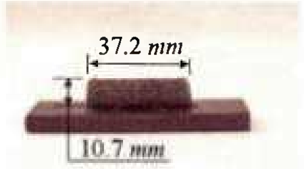

(c) Single wall with a 20 s dwell between layers (Case 3)

Fig. 2. Images of the deposited thin walls.

3. Calibration and validation depositions

Single track thin walls of Ti–6Al–4V are deposited using an Optomec® LENS MR-7 system with a 500 W IPG Photonics fiber laser. The deposition occurs in a chamber with an argon atmosphere that has an oxygen content of less than 15 parts per million. A 30 L/min argon jet is used to supply argon to the chamber, to protect the laser optics, and to shield the melt pool. The Ti–6Al–4V powder delivered to the melt pool is assisted by four argon jets that have a combined flow rate of 4 L/min. These four jets exit nozzles positioned around the main nozzle and aimed at the melt pool, as shown in Fig. 1. The powder has been sieved so that only particles with diameters between 44 and 149 μm are delivered at a rate of 3.0 g/min. A LENS system is chosen because several researchers have investigated the effect of its processing parameters on the deposition geometry [42] and the material properties [43,44] of Ti–6Al–4V.

The model is validated using three different depositions, as shown in Fig. 2. Each case builds a wall that is designed to be 38.1 mm long, 12.7 mm tall, and 3 mm wide. These cases produce different thermal and mechanical results that are used to validate the model:

1. A single wall built using 62 layers, each one track wide, that are deposited without any dwell between layers onto a 76.2 mm long, 25.4 mm wide and 6.4 mm thick Ti–6Al–4V substrate.
2. A 2nd 62 layer wall is deposited on top of the wall built in Case 1 without any dwell between each layer. This results in a final deposition that is a total of 124 layers, hereafter referred to as the double wall. This deposition increases the area over which the forced convection acts and allows a thermocouple to be attached to the wall to monitor its temperature.
3. A 62 layer wall is deposited onto a substrate with a 20 s dwell between each layer. This generates lower temperatures compared to the deposition with no dwell (Case 1).

Table 2 presents the process conditions used in each case. In all depositions the nominal power is 500 W; however, power measurements made using a Macken P500 power probe (with

Table 2
The test cases and process conditions used.

Case	1	2	3
Measured laser power (W)	410	415	415
Travel speed (mm/s)	8.5	8.5	8.5
Powder delivery rate (g/min)	3.0	3.0	3.0
Additional dwell between layers (s)	0	0	20
Total wall height (mm)	11.2	23.2	10.7
Measured wall length (mm)	39.2	39.3	37.2
Measured wall width (mm)	3.0	3.1	2.2

Please cite this article in press as: Heigel JC, et al. Thermo-mechanical model development and validation of directed energy deposition additive manufacturing of Ti-6Al-4V. Addit Manuf (2014), http://dx.doi.org/10.1016/j.addma.2014.10.003

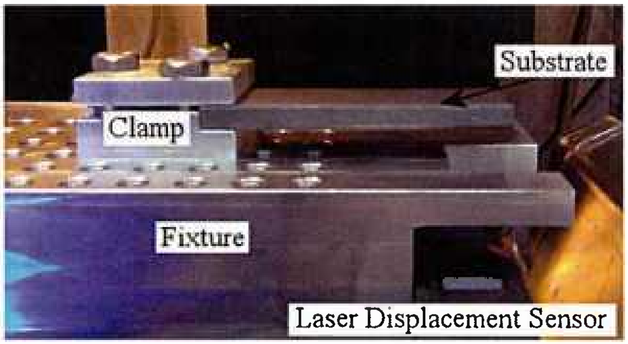

Fig. 3. The experimental setup.

an accuracy of ±25 W) before each deposition show that the actual power being supplied by the laser is between 410 W and 415 W.

3.1. Deposition measurements

In situ deflection of the substrate is measured by clamping one of its ends into a fixture, cantilevering the free end over a laser displacement sensor (LDS), Fig. 3. The LDS used in this study is a Keyence LK-031, which has a measurement accuracy of ±1 μm. It measures the vertical distance to a point on the bottom surface of the substrate, as shown in Fig. 4.

In situ temperature is measured at several locations on the substrate, as shown in Fig. 4, using Omega GG-K-30 type K thermocouples. The thermocouples have a measurement uncertainty of 2.2 °C or 0.75%, whichever is larger. TC 1 is located on the bottom surface of the substrate, while TC 2 is on the top surface, near the wall. Aluminum foil tape was used to shield TC 2 from the effects of convection during Cases 2 and 3. It was not used during Case 1. Consequently, the TC 2 measurements from Case 1 could not be used because the gas flow affected the thermocouple measurements. Before the second wall is built in Case 2, an additional thermocouple (TC 3) is welded to the face of the existing wall, this thermocouple is not used in the other depositions.

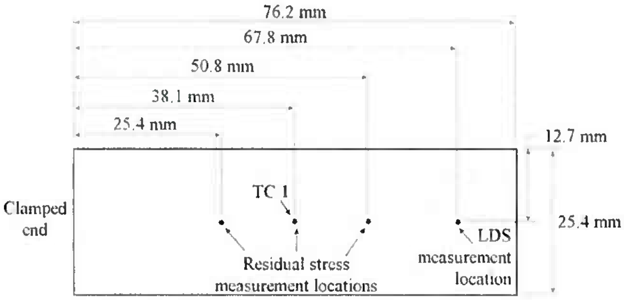

(a) Bottom of the substrate

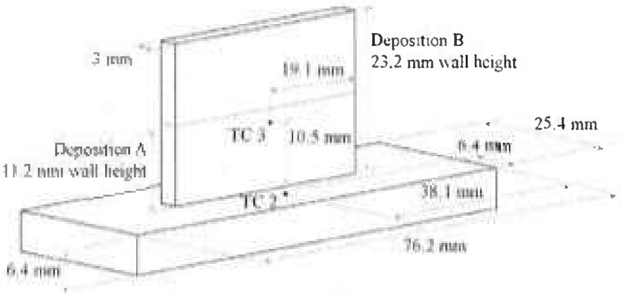

(b) Isometric view of the part

Fig. 4. The locations of each measurement.

The post-process residual stress is measured using the hole-drilling method at three points along the bottom surface of each substrate. Micro-Measurements® model EA-06-062RE-120 strain gauges, which have a measurement error of ±50 MPa, are bonded to the substrate at the locations shown in Fig. 4. The procedures described in manufacturing engineering data sheet U059-07 and technical note 503 are used to calibrate each gauge. The ASTM E837 incremental drilling process is followed using a RS-200 Mill Guide and a Micro-Measurements® high speed drill. Carbide tipped Type II Class 4A drill bits, with diameters of 1.52 mm are used to drill each hole to a final depth of 2 mm, in 0.25 mm deep increments. The strain measurements are made using a Micro-Measurements® P-3500 Strain Indicator and the gauge bridges are balanced with a Micro-Measurements® model SB-1 Switch and Balance Unit.

4. Numerical implementation

4.1. The FEA solver

The FEA analysis is performed using CUBIC (Pan Computing LLC), a Newton–Raphson based solver developed specifically to model additive manufacturing technologies. The hybrid "quiet"/inactive element activation method is used to simulate the deposition of material during the DED process [39]. The model initially includes all the elements in the substrate. Before each layer is deposited, its elements are introduced into the set of equations. When the elements of a layer are first introduced, they are "quiet," that is their material properties are scaled to be smaller so that they do not affect the analysis before they are activated. Thermal conductivity (k), specific heat capacity (C_p), and elastic modulus (E) are scaled by 10^{-6}, 10^{-2}, and 10^{-4}, respectively. The properties of an element are switched from "quiet" to active when any Gauss point of the element is consumed by the heat source volume (Eq. (3)). In addition to the properties being switched, the temperature of the activated element is reset to the ambient temperature to prevent erroneous heating of the element. The free surfaces of the part are re-assessed whenever an element is switch from "quiet" to active to ensure that convection and radiation are applied properly to the evolving part surface, which includes the interfaces between the "quiet" and active elements.

4.2. Finite element mesh

Fig. 5 presents the 3-dimensional half-symmetry mesh that is used for both the thermal and mechanical analysis. The black surface represents the symmetry plane. The mesh comprises 23,295 nodes and 15,627 elements. There are 11,904 elements in the 25.2 mm tall, 38.1 mm long, 1.5 mm thick wall. The aluminum

Please cite this article in press as: Heigel JC, et al. Thermo-mechanical model development and validation of directed energy deposition additive manufacturing of Ti–6Al–4V. Addit Manuf (2014), http://dx.doi.org/10.1016/j.addma.2014.10.003

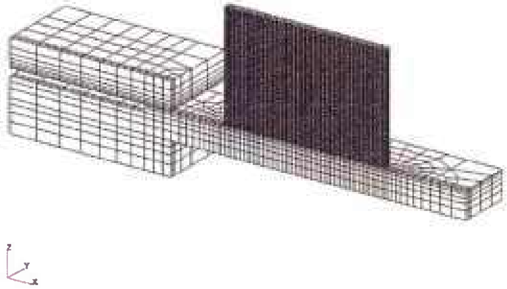

Fig. 5. The half-symmetry finite element mesh of the substrate, wall, and the fixture's aluminum clamp.

clamp used to hold the substrate in the measurement fixture is included in the mesh to account for the heat transfer from the substrate into it. Each deposition layer is 1 element tall (0.203 mm) and 2 elements wide, equating to each element being equal to 1/4 of the laser diameter. The model is mechanically constrained such that it is cantilevered and allowed to deform in the same manner as the experiments.

Errors between measurement and simulation results are calculated by comparing instances in time, or by calculating the percent error over the deposition time:

$$\%\,\mathrm{Error} = \frac{100\sum_{i=1}^{n} |[(T_{\mathrm{meas}})_i - (T_{\mathrm{node}})_i]/(T_{\mathrm{meas}})_i|}{n} \tag{9}$$

where n is the total number of simulated time increments between the beginning and end of the deposition, i is the current time increment, T_{node} is the simulated temperature, and T_{meas} is the measured temperature.

5. Simulation cases

Table 3 presents the convection models used to simulate each case to illustrate the impact of the convection model on the simulation results. The forced convection model is developed from measurements of the distribution of h (Appendix A) and is presented in Fig. 6 for a single wall deposition (Case 1 or 3) when it is half complete. This convection model is independent of the deposition material. Fig. 6 presents the distribution of the value of h acting on a single wall deposition (Case 1 or 3) when it is half complete. The free convection model assumes a uniform coefficient of convection on all surfaces equal to 10 W/m^2/°C. This value is approximately equal to the free convection in air used in other studies [6,5,28–31,10,32,33].

Table 3
The convection models used to simulate each case.

Convection model	$h_{a_{\mathrm{wall}}}$	$h_{o_{\mathrm{wall}}}$	$h_{a_{substrate}}$	$h_{o_{substrate}}$
Forced	$-2.717z+37.174$	25	$1.9h_{a_{wall}}$	30
Free	0	10	0	10

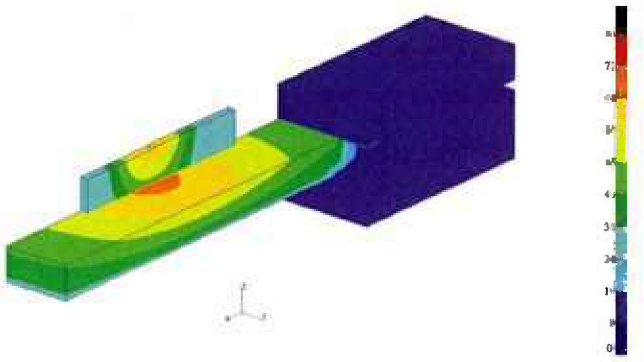

Fig. 6. The forced convection acting on a single wall when the wall is half complete. The convection scale is in W/m^2/ C.

6. Results and discussion

6.1. Thermal history

Fig. 7 presents the simulated temperature distribution at the middle of each deposition using the forced convection model. The deposition of a single wall with no dwell between layers (Case 1) generates the highest temperature, since the heat is input quickly and the mass of the deposition is relatively small. The deposition of a second wall with no dwell (Case 2) experiences high temperatures in the wall, but lower temperatures in the substrate compared to the first wall in Case 1. This is due to the increased wall height that adds thermal mass to the part and also resists conduction into the substrate. Additionally, the increased wall height provides a greater surface area for the convection to extract heat from the part. The single wall deposition with a 20 s dwell between each layer (Case 3) experiences the lowest temperatures because the dwell allows for more cooling of the part.

Fig. 8 presents the thermal measurements and simulation results of the single wall deposition using no dwell between layers (Case 1). The measurements made using TC 1, which is located on the center of the bottom surface of the substrate, are presented along with the corresponding simulation results. The measurement-based forced convection model results in the best thermal simulation results during the deposition process (0–287 s), with a percent error of 2.4%, whereas the free convection model results in a percent error of 15.4%. It is clear from these results that the free convection model does not allow enough heat transfer and thus the temperatures are too high. The measurement-based forced convection model results in greater heat transfer that produce more accurate thermal results.

Fig. 9(a) presents the thermal measurements and simulation results of the deposition of the second wall using no dwell between layers (Case 2). As the surface area increases from the single wall (Case 1) to the double wall (Case 2), the error from each convection model increases. The error from the free convection model increases from 15.4% (Case 1) to 22.2% (Case 2), indicating that as the part size increases, the assumption of free convection leads to greater simulation error. On the other hand, the error from the forced convection model also increases, though by a lesser extent, from 2.1% (Case 1) to 4.1% (Case 2).

Please cite this article in press as: Heigel JC, et al. Thermo-mechanical model development and validation of directed energy deposition additive manufacturing of Ti–6Al–4V. Addit Manuf (2014), http://dx.doi.org/10.1016/j.addma.2014.10.003

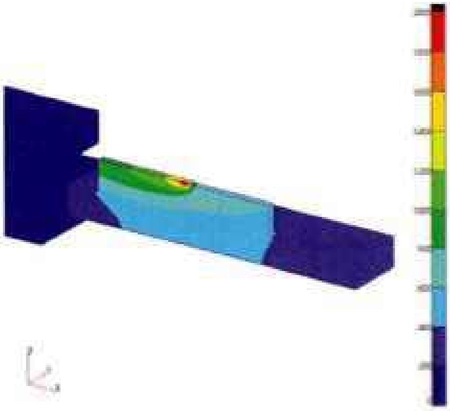

(a) Single wall deposition, no dwell (Case 1)

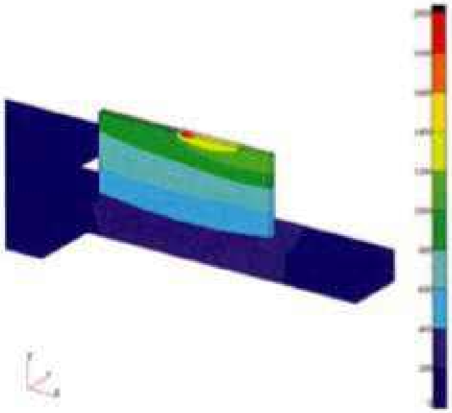

(b) Double wall deposition, no dwell (Case 2)

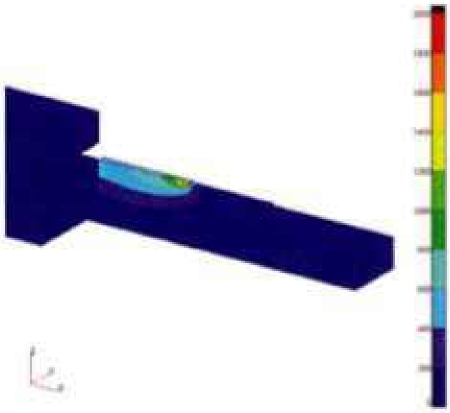

(c) Single wall deposition, 20 s dwell (Case 3)

Fig. 7. The simulated temperature distribution within each deposition when it is half complete resulting from the measurement-based forced convection model. The temperature scale is in °C.

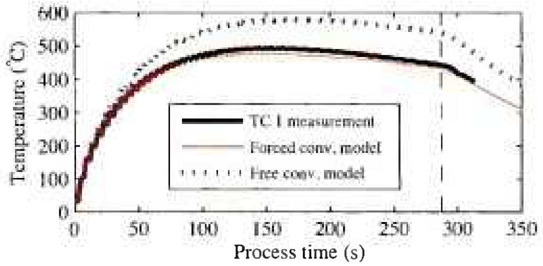

Fig. 8. The temperature history of the single wall deposition with no dwell (Case 1). Measurements are made using TC 1, which is located on the bottom surface of the substrate, and compared to the simulation results. The dashed vertical line indicates the deposition conclusion.

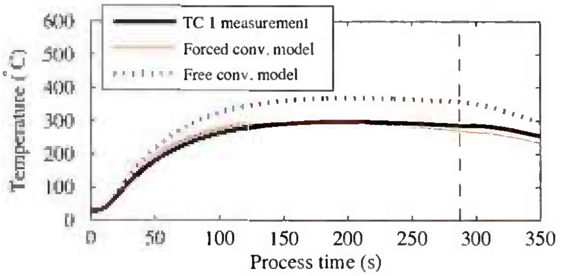

(a) TC 1

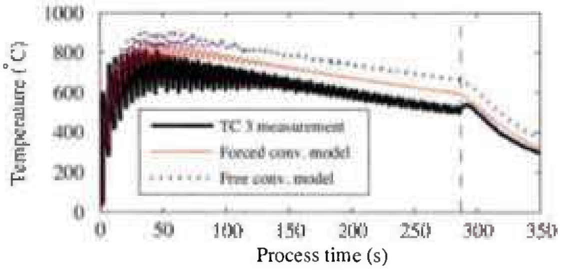

(b) TC 3

Fig. 9. The temperature history during the deposition of the second wall with no dwell between layers (Case 2). The dashed vertical line indicates the deposition conclusion.

This indicates that although the forced convection model is more accurate than the free convection model, it can be improved.

Fig. 9(b) compares the simulation results to the measurements made on the wall using TC 3. It was not possible to shield the thermocouple from the effect of convection because the thermocouple was welded on the wall close to the deposition. Consequently, the convection cools the thermocouple junction, making it experience lower temperatures while the jets are flowing. The temperature measurement rises quickly when the jets are shut off at approximately 293 s. Despite this difference during the depositions comparisons can be made at a time of 297 s, which is after the point that the argon gas supply was shut off. The forced convection produces a percent error of 2.2% at this time, while the percent error resulting from the free convection model is 16.9%. This further demonstrates the improved results using the measurement-based forced convection model.

The greatest errors between the measurements and simulations results occur during the single wall deposition with a 20 s dwell between each layer (Case 3), as shown in Fig. 10. The measurement-based convection model results in a 10.4% error, while the free convection model produces a percent error of 43.8%. The increased processing time during this case allows for a greater amount of heat to be evacuated through convection.

Please cite this article in press as: Heigel JC, et al. Thermo-mechanical model development and validation of directed energy deposition additive manufacturing of Ti–6Al–4V. Addit Manuf (2014), http://dx.doi.org/10.1016/j.addma.2014.10.003

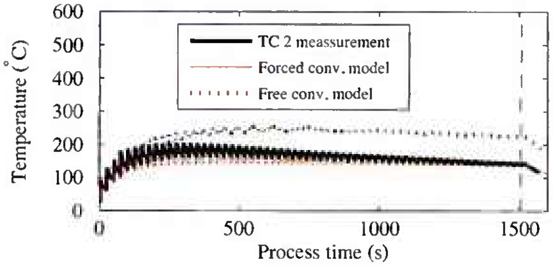

Fig. 10. The temperature history of the single wall deposition with a 20 s dwell between layers (Case 3). Measurements are made using TC 2, which is located on the top surface of the substrate, and compared to the simulation results. The dashed vertical line indicates the deposition conclusion.

It has been demonstrated in each case that the measurement-based forced convection produces superior results compared to the assumption of free convection; however, the forced convection model can be improved. This is understandable since it is developed from the measurements made at three locations on two different surfaces. One approach to develop an improved model is to perform more detailed measurements to investigate the effect of specific part geometries on convection. Another approach would be to use convection measurements to validate CFD of the gas flow over the evolving deposition surface. The CFD approach would enable a broader range of deposition geometries to be modeled without necessitating further convection measurements. Whichever approach is used, convection measurements of the specific deposition equipment must be performed.

6.2. Deflection history

Fig. 11 shows the final simulated deformation of the single wall deposition with no dwell between layers (Case 1). The distortion has been scaled up by a factor of 5 so that the deformation is evident. The deposition process bends the part upwards and shrinks the wall from its nominal size. Each case exhibits this behavior.

Fig. 12 presents the measured and simulated deflection for the single wall with no dwell between layers (Case 1). The LDS deflection measurement is more sensitive to the strain of the material nearer to the clamp as a result of the substrate being cantilevered over it. When the laser is nearest the clamp the thermal expansion of the material near the melt pool causes the substrate to deflect downward. This occurs at the end of the even numbered layers and the beginning of the odd numbered layers. As the laser moves away from the the clamp, that material contracts as it cools, causing the substrate to deflect up, producing a consistent net increase in deflection during the deposition of layers 1–14 (0–62 s). The net deflection decreases during the deposition of layers 15–35 (62–155 s). The remaining layers cause a net increase in deflection, though the amplitude of the oscillation decreases as the wall height increases. Once the deposition concludes, indicated by the vertical dashed line at 287 s, the deflection increases rapidly until it reaches a steady state.

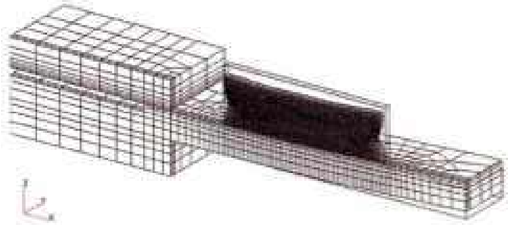

Fig. 11. The simulated final deformation of the single wall deposition with no dwell between layers (Case 1) resulting from the forced convection model. The deformation has been scaled by a factor of 5 to emphasize the substrate deformation.

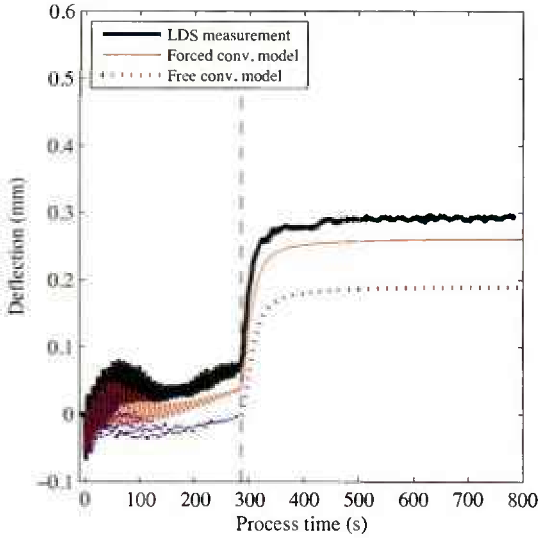

Fig. 12. A comparison of the simulated and measured deflection history of the single wall deposition with no dwell between layers (Case 1). The dashed vertical line indicates the deposition conclusion.

The measurement-based convection model produces the best correlation with the experimental measurements in the single wall deposition (Case 1). The lower predicted deflection generated from the free convection model is a consequence of the greater amount of instantaneous annealing and creep at the higher temperatures. These results demonstrate that a measurement-based convection model is required to produce thermal and deflection results when instantaneous annealing and creep occur.

Fig. 13 presents the measured and simulated deflection for the double wall deposition with no dwell between layers (Case 2). The residual deflection in the part from the deposition of the first wall in Case 1 has been subtracted from the results. The deflection measured during the deposition of the double wall is very different from that measured during the deposition of the first in Case 1. The measured deflection decreases rapidly as the wall experiences thermal expansion during the first several deposition layers, then increases after the sixth track (at 32 s). Both of the simulation cases capture this trend very well. The free convection model produces more accurate results compared to the measurement-based forced convection model despite the inferior thermal results. This indicates that the material properties are not fully captured in the mechanical model. One possible cause for this is that the instantaneous annealing and creep are

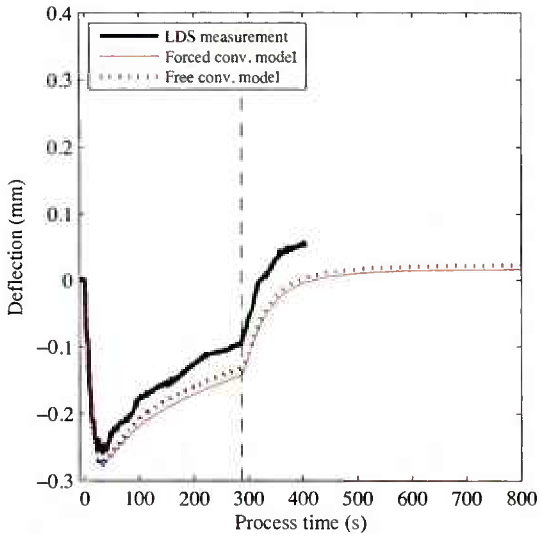

Fig. 13. A comparison of the simulated and measured deflection history of the double wall deposition with no dwell between layers (Case 2). The dashed vertical line indicates the deposition conclusion.

actually time dependent, as speculated by Denlinger et al. [45] but is not accounted for in this model.

Fig. 14 presents the measured and simulated deflection during the deposition of the single wall with a 20 s dwell between each layer (Case 3). The deflection oscillates with each deposition layer and experiences a net increase after each layer. Both simulation cases capture this trend. The measurement-based forced convection model results in an over-prediction of the deflection, whereas the free convection model under-predicts the deflection. However, the absolute difference between each model and the experiments is approximately equal.

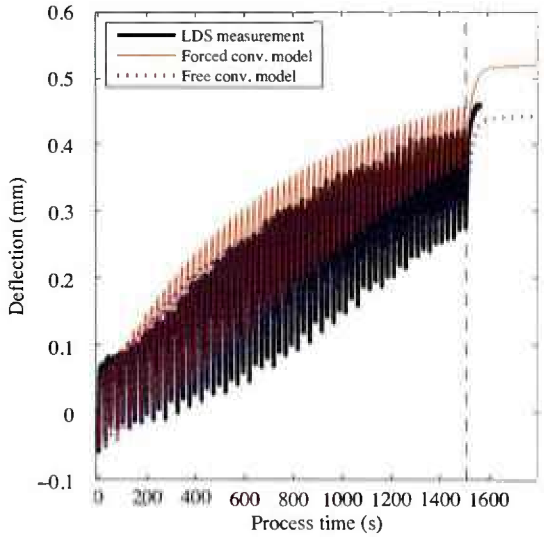

Fig. 14. A comparison of the simulated and measured deflection history of the single wall deposition with a 20 s dwell between layers (Case 3). The dashed vertical line indicates the deposition conclusion.

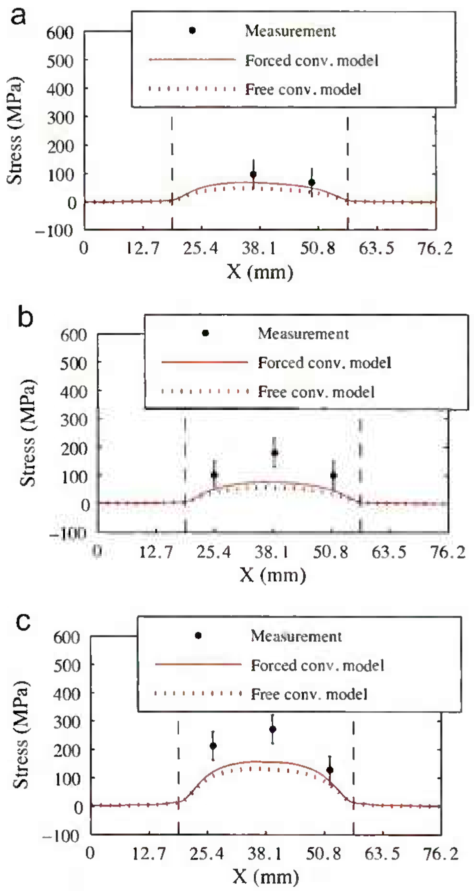

Fig. 15. The residual stress measurements and simulation results. The dashed vertical line indicates the edges of the wall.

6.3. Residual stress

Fig. 15 presents the residual stress in the bottom surface of the substrate after each deposition has been allowed to cool. The error bars represent the measurement accuracy of the strain gages, which is ±50 MPa. For comparison, the simulated stress from each case is extracted from the nodes along the centerline. The measurements and each simulation case exhibit a trend where the greatest stress occurs under the center of the wall. The stress decreases as the ends of the wall are approached. The wall edges are indicated by the dashed vertical lines. In each case, the measurement-based forced convection model produces the highest stresses compared to the free convection model and the best results compared to the measurements.

7. Conclusions

Experimentally measured surface convection is implemented into a thermo-mechanical model of DED additive manufacturing. Three different thin-wall cases, with different geometries and dwell times, are made to validate the thermo-mechanical model. To illustrate the need for the measurement-based forced convection model, a second model is developed that assumes

Please cite this article in press as: Heigel JC, et al. Thermo-mechanical model development and validation of directed energy deposition additive manufacturing of Ti–6Al–4V. Addit Manuf (2014), http://dx.doi.org/10.1016/j.addma.2014.10.003

free convection on all surfaces, which is a common approach used in the literature.

Comparisons between *in situ* temperature measurements simulation results show that the measurement-based forced convection model achieves the most accurate results for each case, with percent errors of less than 11% when compared to the measurements, whereas the free convection model simulates temperatures with percent errors of up to 44% for the three depositions. Although the measurement-based forced convection model produces superior results, it can be improved through more accurate geometry specific measurements, or through validated CFD analysis.

The residual stress measurements and *in situ* deflection measurements show that the measurement-based convection model produces more accurate stress measurements in all cases. However, the forced convection model produces more accurate deflection in only one of the cases, despite the superior thermal results, indicating that a more detailed mechanical model is required.

Acknowledgments

J.C. Heigel is supported by the National Science Foundation under Grant No. DGE1255832. This work is also supported in part by the Office of Naval Research, under Contract No. N00014-11-1-0668. Any opinions, findings, and conclusions or recommendations expressed in this material are those of the authors and do not necessarily reflect the views of the National Science Foundation or the Office of Naval Research.

Appendix A. Convection measurements

Hot-film constant voltage anemometry is used to measure the distribution of the surface convection generated by the deposition head. The measurements are made using three Senflex® SF9902 single-element hot-film sensors that are adhered to the surface of a 3.2 mm thick plexiglass plate using MACfilm® IF-2012 adhesive. A constant voltage is supplied to each sensor using a Model 4-600 constant voltage anemometer (CVA). Both the sensors and CVA are from Tao of Systems Integration, Inc.

Two sensors are adhered onto a plexiglass plate that is mounted vertically to simulate the thin-wall geometry. Sensor 1 (S1) is mounted 0.8 mm below the top edge of the plate, and Sensor 2 (S2) is mounted 5.4 mm below the top edge, as shown in Fig. 16(a). The back-side of the plexiglass plate is ground so that the top edge has a 45° angle to minimize its effect on the argon jet. The measurements are made by positioning the bottom of the powder delivery nozzles 9.3 mm above the top edge of the plate and moving the head in 1 mm increments along the X axes. The 9.3 mm offset is also used when depositing material. The heat transfer coefficient, h, is calculated from the measurement data at each increment once steady state is achieved.

The heat transfer acting on a horizontal surface is measured by mounting a third sensor onto the center of the plexiglass substrate, as shown in Fig. 16(b). Measurements are made by moving the deposition head in 3 mm increments along the positive and negative X and Y axes, which are centered at the sensor.

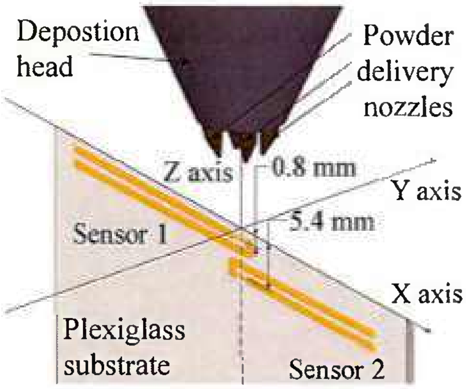

(a) The setup for a vertical wall

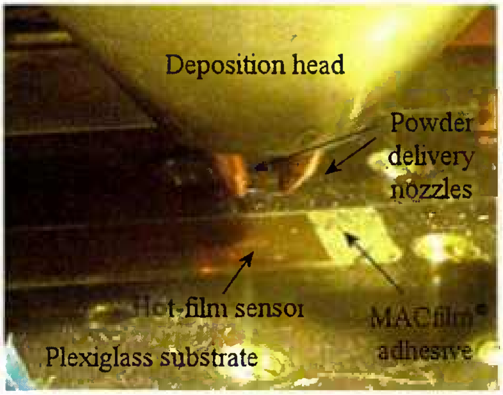

(b) The setup for a horizonal surface.

Fig. 16. The setups used to measure the forced convection.

Appendix B. Convection model

Fig. 17 presents the results of the surface convection measurements used to develop the model. The measured convection acting on a vertical wall using the two sensors (S1 and S2) is presented in Fig. 17. Each point in the plot is the mean value of four measurements and the error bars represent the standard deviation of each measurement. The convection acting on a horizontal surface, measured using S3, is presented in Fig. 17. In this case, each point is the mean of eight measurements.

When measured on both a horizontal surface and a vertical wall, the value of h dissipates as the distance from the centerline of the jet increases. An exponential decay function is fit to the measurement data:

$$h = h_a e^{-(\theta r)^{\phi}} + h_o \qquad (B.1)$$

where r is the distance from the centerline of the argon jet to the point of interest and h_o is the value measured at the outer most locations that the function decays to. The peak of the forced convection is defined by h_a. The variables θ and ϕ are used to define the shape of the decay. Different values for these variables are required for the wall and for the substrate because the convection

Please cite this article in press as: Heigel JC, et al. Thermo-mechanical model development and validation of directed energy deposition additive manufacturing of Ti–6Al–4V. Addit Manuf (2014), http://dx.doi.org/10.1016/j.addma.2014.10.003

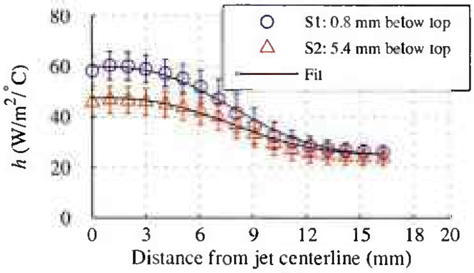

(a) Convection on a vertical wall.

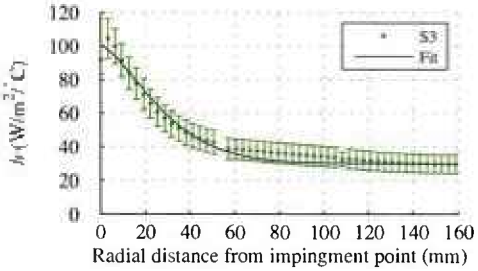

(b) Convection on a horizontal surface.

Fig. 17. The results of the convection measurements.

on the wall has a lesser magnitude and narrower distribution than on the horizontal surface.

B.1. Forced convection on a vertical wall

The best fit to the wall convection data that is presented in Fig. 17 is achieved when $\theta = 0.107$, $\phi = 2.7$ and $h_{o_{\text{wall}}} = 25\,\text{W/m}^2/^\circ\text{C}$. The only variable that changes between the fit of the two data sets is $h_{a_{\text{wall}}}$, which decreases from a value of $35\,\text{W/m}^2/^\circ\text{C}$ at a distance of 0.8 mm (S1) from the top edge to a value of $23\,\text{W/m}^2/^\circ\text{C}$ at a distance of 5.4 mm (S2).

The decrease of $h_{a_{\text{wall}}}$ as the distance from the top edge of the wall increases is assumed to be linear:

$$h_{a_{\text{wall}}} = -2.717z + 37.174 \tag{B.2}$$

where z is the distance from the top edge of the wall to the point of interest. Substituting Eq. (B.2) in Eq. (B.1) yields the following equation that describes the convection on a thin, single track wide deposited wall:

$$h_{\text{wall}} = (-2.717z + 37.174)\mathrm{e}^{-(0.107r)^{2.7}} + 25 \tag{B.3}$$

This equation is only applicable up to a vertical distance of 13.7 mm from the top edge of the wall. At greater distances the effect of the jet is assumed to diminish so that $h_{a_{\text{wall}}} = 0\,\text{W/m}^2/^\circ\text{C}$ and $h_{o_{\text{wall}}}$ remains $25\,\text{W/m}^2/^\circ\text{C}$.

B.2. Forced convection on a horizontal surface

The best fit to the horizontal surface convection data that is presented in Fig. 17 is described when $\theta = 0.031$, $\phi = 1.4$, $h_{a_{\text{surface}}} = 70\,\text{W/m}^2/^\circ\text{C}$, and $h_{o_{\text{surface}}} = 30\,\text{W/m}^2/^\circ\text{C}$. This is only applicable when the head is positioned so that it is depositing directly onto the horizontal surface and not when a wall is being deposited. To account for the deposition of the wall, it is assumed that $h_{a_{\text{surface}}}$ decreases as the distance between the surface and the nozzle increases. Specifically, $h_{a_{\text{surface}}}$ is directly related to $h_{a_{\text{wall}}}$:

$$h_{a_{\text{surface}}} = \frac{70}{37.174} h_{a_{\text{wall}}} = 1.9(-2.717z + 37.174) \tag{B.4}$$

As a result, the model to define the forced convection acting on a horizontal surface as a wall is deposited on top of it is:

$$h_{\text{surface}} = 1.9(-2.717z + 37.174)\mathrm{e}^{-(0.031r)^{1.4}} + 30 \tag{B.5}$$

It is assumed that once the effect of the jet on the wall has been fully dissipated, the localized forced convection defined by $h_{a_{\text{surface}}}$ can no longer be generated on the surface. Consequently, $h_{a_{\text{surface}}} = 0\,\text{W/m}^2/^\circ\text{C}$ when $h_{a_{\text{wall}}} = 0\,\text{W/m}^2/^\circ\text{C}$.

B.3. Convection on the underside of the substrate

There is no measurement data of the surface convection that occurs on the underside of the substrate during the deposition. It is assumed that it is equal to $h_{o_{\text{surface}}}$.

B.4. Free convection in the absence of the argon jets

After each deposition, the argon gas jets are shut off and no forced convection occurs. In addition, the argon atmosphere in the deposition chamber is no longer agitated by the argon flow. As a consequence, the convection becomes uniform on all surfaces and equal to free convection ($10\,\text{W/m}^2/^\circ\text{C}$).

References

[1] ASTM Standard F2792. Standard terminology for additive manufacturing technologies; 2012, http://dx.doi.org/10.1520/F2792-12A www.astm.org
[2] Vasinonta A, Beuth J, Griffith M. Process maps for laser deposition of thin-walled structures. In: Proc solid freeform fab symp. The University of Texas at Austin; 1999. p. 383–91.
[3] Kahlen F-J, Kar A. Residual stresses in laser-deposited metal parts. J Laser Appl 2001;13:60.
[4] Aggarangsi P, Beuth J, Griffith M. Melt pool size and stress control for laser-based deposition near a free edge. In: Proc solid freeform fab symp. The University of Texas at Austin; 2003. p. 196–207.
[5] Labudovic M, Hu D, Kovacevic R. A three dimensional model for direct laser metal powder deposition and rapid prototyping. J Mater Sci 2003;38(1):35–49.
[6] Jendrzejewski R, Śliwiński G, Krawczuk M, Ostachowicz W. Temperature and stress fields induced during laser cladding. Comput Struct 2004;82(7):653–8.
[7] Jendrzejewski R, Śliwiński G. Investigation of temperature and stress fields in laser cladded coatings. Appl Surf Sci 2007;254(4):921–5.
[8] Zekovic S, Dwivedi R, Kovacevic R. Thermo-structural finite element analysis of direct laser metal deposited thin-walled structures. In: Proc solid freeform fab symp. The University of Texas at Austin; 2005. p. 338–55.
[9] Plati A, Tan J, Golosnoy I, Persoons R, Van Acker K, Clyne T. Residual stress generation during laser cladding of steel with a particulate metal matrix composite. Adv Eng Mater 2006;8(7):619–24.
[10] Wang L, Felicelli S, Pratt P. Residual stresses in LENS-deposited AISI 410 stainless steel plates. Mater Sci Eng A: Struct 2008;496(1):234–41.
[11] Yang Y-P, Babu S. An integrated model to simulate laser cladding manufacturing process for engine repair applications. Weld World 2010;54(9–10):R298–307.

[12] Klingbeil N, Beuth J, Chin R, Amon C. Residual stress-induced warping in direct metal solid freeform fabrication. Int J Mech Sci 2002;44(1):57–77.

[13] Chiumenti M, Cervera M, Salmi A, Agelet de Saracibar C, Dialami N, Matsui K. Finite element modeling of multi-pass welding and shaped metal deposition processes. Comput Method Appl Mech Eng 2010;199(37):2343–59.

[14] Lee J-Y, Kim Y-C, Inose K. Verification of validity and generality of dominant factors in high accuracy prediction of welding distortion. Weld World 2010;54(9–10):R279–85.

[15] Anca A, Fachinotti V, Escobar-Palafox G, Cardona A. Computational modelling of shaped metal deposition. Int J Numer Methods Eng 2011;85(1):84–106.

[16] Marimuthu S, Clark D, Allen J, Kamara A, Mativenga P, Li L, et al. Finite element modelling of substrate thermal distortion in direct laser additive manufacture of an aero-engine component. Proc Inst Mech Eng C: J Mech Eng Sci 2013;227(9):1987–99.

[17] Denlinger E, Heigel J, Michaleris P. Residual stress and distortion modeling of electron beam direct manufacturing Ti–6Al–4V. Proc Inst Mech Eng B: J Eng Manuf 2014:11, http://dx.doi.org/10.1177/0954405414539494.

[18] Lindgren L-E. Finite element modeling and simulation of welding. Part 1: Increased complexity. J Therm Stresses 2001;24(2):141–92.

[19] Lindgren L-E. Finite element modeling and simulation of welding. Part 2: Improved material modeling. J Therm Stresses 2001;24(3):195–231.

[20] Lindgren L-E. Finite element modeling and simulation of welding. Part 3: Efficiency and integration. J Therm Stresses 2001;24(4):305–34.

[21] Perry K. Heat transfer by convection from a hot gas jet to a plane surface. Proc Inst Mech Eng 1954;168(1):775–84.

[22] Gardon R, Akfirat J. The role of turbulence in determining the heat-transfer characteristics of impinging jets. Int J Heat Mass Transfer 1965;8(10):1261–72.

[23] O'Donovan T, Murray DB. Jet impingement heat transfer—Part 1: Mean and root-mean-square heat transfer and velocity distributions. Int J Heat Mass Transfer 2007;50(17):3291–301.

[24] Tikare V, Griffith M, Schlienger E, Smugeresky J. Simulation of coarsening during laser engineered net-shaping [Tech. rep.]. Albuquerque (NM, USA): Sandia National Labs; 1997.

[25] Hofmeister W, Wert M, Smugeresky J, Philliber J, Griffith M, Ensz M. Investigation of solidification in the laser engineered net shaping (LENS) process. JOM 1999;51(7):1–6.

[26] Pinkerton A, Li L. The development of temperature fields and powder flow during laser direct metal deposition wall growth. Proc Inst Mech Eng C: J Mech Eng Sci 2004;218(5):531–41.

[27] Vasinonta A, Beuth J, Griffith M. Process maps for predicting residual stress and melt pool size in the laser-based fabrication of thin-walled structures. J Manuf Sci E: Trans ASME 2007;129(1):101–9.

[28] Kelly S, Kampe S. Microstructural evolution in laser-deposited multilayer Ti–6Al–4V builds: Part II. Thermal modeling. Metall. Mater Trans A 2004;35(6):1869–79.

[29] Zheng B, Zhou Y, Smugeresky J, Schoenung J, Lavernia E. Thermal behavior and microstructural evolution during laser deposition with laser-engineered net shaping: Part I. Numerical calculations. Metall Mater Trans A 2008;39(9):2228–36.

[30] Jendrzejewski R, Kreja I, Śliwiński G. Temperature distribution in laser-clad multi-layers. Mater Sci Eng A: Struct 2004;379(1):313–20.

[31] Pratt P, Felicelli S, Wang L, Hubbard C. Residual stress measurement of laser-engineered net shaping AISI 410 thin plates using neutron diffraction. Metall Mater Trans A 2008;39(13):3155–63.

[32] He X, Yu G, Mazumder J. Temperature and composition profile during double-track laser cladding of H13 tool steel. J Phys D: Appl Phys 2010;43(1):015502.

[33] Lundbäck A, Lindgren L-E. Modelling of metal deposition. Finite Elem Anal Des 2011;47(10):1169–77.

[34] Hoadley A, Rappaz M, Zimmermann M. Heat-flow simulation of laser remelting with experimenting validation. Metall Trans B 1991;22(1):101–9.

[35] Dai K, Shaw L. Distortion minimization of laser-processed components through control of laser scanning patterns. Rapid Prototyping J 2002;8(5):270–6.

[36] Gardon R, Cobonque J. Heat transfer between a flat plate and jets of air impinging on it. In: Int conf on heat transfer, Part II. ASME; 1961. p. 460.

[37] Ghosh S, Choi J. Three-dimensional transient finite element analysis for residual stresses in the laser aided direct metal/material deposition process. J Laser Appl 2005;17:144.

[38] Boyer R, Collings E. Materials properties handbook: titanium alloys. ASM International; 1994.

[39] Michaleris P. Modeling metal deposition in heat transfer analysis of additive manufacturing processes. Finite Elem Anal Des 2014:86:51–60.

[40] Goldak J, Chakravarti A, Bibby M. A new finite element model for welding heat sources. Metall Trans B 1984;15(2):299–305.

[41] Kummailil J. Process models for laser engineered net shaping [Ph.D. thesis]. Worcester Polytechnic Institute; 2004.

[42] Kummailil J, Sammarco C, Skinner D, Brown C, Rong K. Effect of select lens processing parameters on the deposition of Ti–6Al–4V. J Manuf Proc 2005;7(1):42–50.

[43] Griffith M, Ensz M, Puskar J, Robino C, Brooks J, Philliber J, et al. Understanding the microstructure and properties of components fabricated by laser engineered net shaping (LENS). In: MRS Proceedings, vol. 625. Cambridge Univ. Press; 2000.

[44] Kobryn P, Semiatin S. Mechanical properties of laser-deposited Ti–6Al–4V. In: Proc solid freeform fab symp. The University of Texas at Austin; 2001. p. 179–86.

[45] Denlinger E, Heigel J, Michaleris P, Palmer TA. Effect of inter-layer dwell time on distortion and residual stress in additive manufacturing of titanium and nickel alloys. J Mater Process Technol 2015;215:123–31, http://dx.doi.org/10.1016/j.jmatprotec.2014.07.030.

Please cite this article in press as: Heigel JC, et al. Thermo-mechanical model development and validation of directed energy deposition additive manufacturing of Ti–6Al–4V. Addit Manuf (2014), http://dx.doi.org/10.1016/j.addma.2014.10.003

Appendix 8 – Patent Application: Method for manufacturing overhanging materials by pulsed, voxel-wise buildup

U.S. Patent Application Serial No: 62/051,174; Title: ``METHOD FOR MANUFACTURING OVERHANGING MATERIAL BY PULSED, VOXEL-WISE BUILDUP''

PENNSTATE

INTEROFFICE CORRESPONDENCE

Applied Research Laboratory

Date: 24 June 2014

Subject: *Category Designation for* ARL Invention Disclosure No. 2014-0904 entitled "Method for manufacturing overhanging material by pulsed, voxel-wise buildup"

From: E. G. Liszka

To: C. L. Wagner, PSU Office of Technology Management

Info: R. A. Harpster PSU Office of Technology Management
B. Johnson, Contract Administrator, Applied Research Lab
A. Nassar, Inventor, Applied Research Lab
E. Reutzel, Inventor, Applied Research Lab
P. R. Righter, Associate Director Business Operations, Applied Research Lab

Encl: ARL Invention Disclosure No. 2014-0904

ARL and the inventors recommend that this Invention Disclosure be designated as a **Category I** Invention wherein ARL takes responsibility for marketing and patent costs.

Background: The invention relates metals-based additive manufacturing and enables deposition of overhangs at and above 45 degrees without special nozzles or tilt tables.

Funding: The invention was developed under Federal funding.

Stage: Developed and demonstrated.

Rationale. The inventor states that the concept has been validated and demonstrated, and is a significant invention to additive manufacturing of metals. Given the breadth of potential research opportunities and opportunity to strengthen ARL's leadership role hydrodynamics, the Committee deemed a Category I designation was appropriate at this time.

Patent Strategy. The recommended approach is to immediately file a provisional patent application to mitigate concerns related to disclosing the technology within the Naval and shipyard community. A decision to move forward with a nonprovisional patent application and maintain as a Category I status would then be made based on the success of program development efforts and reduction to practice over the next year.

Please file a US provisional patent application for this invention.

Status: Please keep ARL informed and copied on all activities and actions associated with this invention.

ARL 2014-0904

PENNSTATE

Technology Disclosure Form

Office of Technology Management
113 Technology Center, University Park, PA 16802
814.865.6277 p • 814.865.3591 f • otminfo@psu.edu

Disclosure Number (*OTM Use Only*)

Original signed form should be submitted to the OTM via your research dean or appropriate administrative unit. We encourage you to concurrently send a signed or unsigned copy electronically directly to the OTM. If possible please submit form at least one month prior to any public disclosure (including web abstracts). See attached guidelines/instructions or contact OTM for assistance.

1. Title of Invention/Technology (brief & non-confidential):

Method for manufacturing overhanging material by pulsed, voxel-wise buildup

2. Please Attach a Detailed Description of Technology (see instructions on page 4):

3. Disclosers/Inventors (please list the primary contact first – attach additional sheets for more than 5):

	Full Legal Name	Title (e.g. "Professor")	Dept. or Affiliation	Inv %
A	Abdalla R Nassar	Research Associate	ARL	90
B	Edward W Reutzel	Research Associate	ARL	10
C				
D				
E				

4. Contact Information:

	Department Address	Home Address	Email Address & Phone #
A	4420D Applied Sciences Bldg	559 Galen Driver #1 State College, PA 16803	arn5000@psu.edu 814-863-9409
B	4420D Applied Sciences Bldg	702 Edgewood Circle State College, PA 16801	ewr101@psu.edu 814-~~8963~~-9891 863
C	e		
D			
E			

5. Disclosure Execution (required for PSU employees only):

	Name	Signature	Citizenship	Date (m/d/yyy)
A	Abdalla R Nassar		USA	3/14/2014
B	Edward W Reutzel		USA	3/19/2014
C				
D				
E				

6. Witness: (who has read and understands the disclosure

Printed Name:	Kenneth C Meinert Jr	Signature:		Date:	3/18/14

7. Research Dean or Administrative Officer:

Printed Name:	Edward Liszka	Signature:		Date:	3/25/14

ARL 2014-0904

PENNSTATE

Technology Disclosure Form

Office of Technology Management
113 Technology Center, University Park, PA 16802
814.865.6277 p · 814.865.3591 otminfo@psu.edu

Disclosure Number (*OTM Use Only*)

8. Record of Invention:

	Event	Date	References (e.g. lab notebooks)
A	Conception of Invention:	03/14/2014	lab notebook
B	Date of Reduction to Practice:	03/14/2014	lab notebook
C	Other (see page 4):		
D	Other (see page 4):		

9. Obligations to Third Parties:

A. Is this technology the result of sponsored research (either government or industry)? Yes x No

	Sponsor:	OSPOSP/ORA Grant #, Contract #, or Agreement #	Principal Investigator
1	Office of Naval Research	GRANT N00014-11-1-0668 ONR BAA 11-003 (FUND 71K70)	Edward W Reutzel
2			
3			

B. Are there any other agreement(s) pertaining to the technology? (include: materials bailment/transfer, consulting, confidentiality, grant-in-aid, etc.) Yes No x

	Agreement Type	Name of Other Party	Contact
1			
2			
	Please attach copies of any third party agreements		

10. Public Disclosures (any publicly available and potentially enabling description – see guidelines, pg 4):

	Disclosure Type (please attach copies)	Yes	No	Date (m/d/yyyy)	Citation and/or Explanation
A	Has the technology been published or a manuscript been submitted for publication?		x		
B	If not, will a manuscript for the technology be submitted in the future? Approx. when?	x		05/01/2014	(Considering This)
C	Has the technology been described in a thesis, or will it be described in a thesis?		x		
D	Has the technology been presented in a public forum (e.g. speech, conference, poster, etc.)?		x		[illegible]
E	Are there any other past or future enabling publications (e.g. online postings)?		x		

11. Descriptive Keywords (to be used for patent or background searching and/or marketing):

Additive Manufacturing	Overhang	LENS	Rapid Solidification

ARL 2014-0904

Please attempt to answer the following questions. In addition to the detailed description that you attach, this information will assist in our assessment of the technology and may increase the likelihood of patenting and commercialization success.

12. Stage of Development: Briefly describe the status of the technology's development. Which of the following terms best describe its stage of development: concept proof of concept, prototype, working model, demo, fully developed? Are samples, a prototype, or a demo available to share with prospective licensees?

The method has been fully developed and demonstrated. Physical specimens, produced with the developed method, have been produced. The method can be further refined through parameter development.

13. Please briefly describe the problem that the technology solves and its advantages/benefits relative to competing technologies or products. What product might this invention become?

Deposition of overhanging structures is a critical problem in metals-based additive manufacturing. Currently, Directed-energy and powder bed additive manufacturing processes have limited capability to deposit overhangs. The stat of the art utilizes specially-designed nozzles to deposit overhangs up to approximately 45 degrees or >3 axis stage arrangements to tilt the substrate or deposition head during processing. The developed method enables deposition of overhangs at and above 45 degrees with a 3-axis stage and without specially-designed nozzles or tilt-table arrangements.

14. Please list key prior art references:

Patents: US 20060003095 A1, US 5038014 A, US 6410105 B1, US 4323756 A, US 5837960 A

15. Please list the companies or industries that are most likely to be interested in licensing this technology:

Additive Manufacturing Industry	Optomec, Inc.
InssTek, Inc.	DM3D Technology, LLC
EOS GmbH Electro Optical Systems	

16. Please list any contacts that you have (and their contact information) that we may approach in our marketing efforts (to learn more about the market potential of the technology or to reach potential licensees):

Richard Grylls, Optomec, Inc, rgrylls@optomec.com

17. Please check the reason(s) that best describe why you submitted this invention disclosure:

x	I/we believe that the invention has significant commercial potential
x	I/we believe that this invention is a platform and/or pioneering technology
	I/we are aware of a specific company that is interested in licensing the technology
	I/we are interested in being involved with a startup company based on this technology
	To comply with the requirements of an existing research agreement and/or University policy
	Other (please specify):

ARL 2014-0904

PENNSTATE

Technology Disclosure Form

Office of Technology Management
113 Technology Center, University Park, PA 16802
814.865.6277 p • 814.865.3591 f • otminfo@psu.edu

Disclosure Number (OTM Use Only)

Instructions/Guidelines

The Office of Technology Management (OTM) promotes beneficial use of Penn State technology by protecting, marketing, and licensing University technologies to companies for further development and commercialization. This disclosure is valuable because it establishes a legal record of the invention while helping to facilitate the OTM's assessment and management of the technology. After reviewing the disclosure form, the OTM will contact the discloser(s)/inventor(s) to review the technology and discuss possible protection and commercialization strategies. Below are instructions or guidelines for each section of the form.

1. The title should be descriptive but must not be "enabling" as defined in item 10 below.
2. Attach a description of the technology/invention that is sufficiently detailed to allow someone of standard skill in your field of expertise to readily (without substantial experimentation) put the technology/invention into practice (at least to the extent that you are able to do so yourself). The description should cover at least: a) brief background and general purpose; b) technical description; and c) advantages and improvements over existing methods or products. Please include diagrams of apparatuses, chemical structures, and flow charts of processes. Often a draft journal article is sufficient.
3. List those individuals who may be considered potential inventors or who contributed to the conception or creative development of the technology. In general terms, an inventor is someone who contributed to the conception of the invention or to the creative further development of an important element of the invention in reducing it to practice. Note that this is not the same as authorship. A "pair of hands" who only carried out the orders of another person is not an inventor, even though such a person may be considered a co-author or contributor in a scholarly sense. Inventorship has a legal definition and will be determined by a patent attorney at the time of filing of any patent application. If needed, please contact the OTM or see http://www.research.psu.edu/offices/otm for further guidance. Include individuals who are not employees of Penn State (although they are not required to sign the form). In the last column, please indicate the agreed upon percent (%) contribution of each discloser of the technology disclosed. These numbers aid in determining any monetary distributions to the disclosers. They may be changed by mutual agreement at a later date. Each inventor who signs this invention disclosure form must agree and be able to provide supporting material if requested for his/her contribution as stated here.
4. Since correspondence, patent application materials, and royalty checks are sent to the inventor's home, each inventor must provide and maintain a current home address with the Office of Technology Management.
5. By signing here, each individual indicates approval of the disclosure, attesting that the disclosure is true, accurate, and fully describes the invention to the best of his/her knowledge.
6. The witness must not be directly involved with the invention but must have read and understood the disclosure.
7. The disclosure form should be submitted for signature to your Research Dean or other administrative unit responsible for handling invention disclosures and forwarded to the OTM. At Penn State Hershey, submit through the Office of Technology Dev.
8. After recording the date of each event, indicate where records of the event may be located. "Reduction to practice" is the physical part of the inventive process during which the invention is shown to work as described (at least for the initial concept). After a reduction to practice, the invention is complete for patent law purposes in that a proof of concept test, prototype, model, or biological strain exists that fulfills the invention's intended purpose. "Other" events may include any other milestones that you achieved in your continued development of the technology that you believe relevant to the record of the invention.
9. There may be obligations to third parties if the research that led to the invention used resources, facilities, staff, funding, or material of another institution, whether it is a corporation, university, foundation, or government agency. Please include support for continued development or evaluation ("Other" events) as listed in items 8C and 8D.
10. "Public Disclosure" means any instance in which someone outside the Penn State community, without being restricted by confidentiality, would have been able to legally gain access to your presented, written or printed enabling description of the technology/invention – where "enabling" means sufficiently described to allow someone of average skill in the relevant field of expertise to practice the invention. The public disclosure dates, especially the first one, are important for patent considerations. In the United States, a patent application must be filed within one (1) calendar year of first public disclosure; however, in most other countries, a patent application must be filed before any public disclosure. An inventor who publicly discloses his/her invention before obtaining protection can lose rights to his/her invention anywhere else in the world. It is therefore requested that inventors contact the Office of Technology Management for assistance prior to public disclosure. Note that many journals now publish online, sometimes weeks before publishing in print. The inventor must be aware of the potential for online publishing, including enabling abstracts/posters, and indicate these in section 10. This helps to ensure adequate protection for the invention.
11. Enter some keywords useful for our background searching, patent searching, and/or categorizing the technology for marketing purposes. An ideal set of keywords includes terms very likely to occur in publications and patents related to the field of your invention as well as terms likely to occur only in publications describing specific solutions to the problem very similar to yours.

12-17. Self Explanatory

ARL 2014-0904

- - ARL PROPRIETARY - -

ARL SUPPLEMENTAL
INVENTION DISCLOSURE FORM

(Must accompany PSU Invention/Software Disclosure Form)

last revised: 7/30/03

Invention/Software Disclosure No. (if known) ________ 2014 - 0904

Title of Invention: Method for manufacturing overhanging material by pulsed, voxel-wise buildup

The purpose of this form is to assist in determining the value of this intellectual property to ARL and an appropriate course of action. Please answer the questions in each category below, then circle the number that best represents your assessment in that category. The scale should be interpreted as follows:

N.O.	1	2	3	4	5
(no opinion)	(none)	(marginal/low)	(moderate)	(good/high)	(excellent/critical)

Assessment

PATENTABILITY (NOVELTY/UTILITY)* 5 N.O. 1 2 3 4 5

*In addressing the question "What technologies compete with the invention?" on page 3 of the **University Invention Disclosure Form**, please conduct a preliminary patent search using US Patent and Trademark Office website (http://www.uspto.gov/patft/index.html), then identify and discuss any relevant patents in your response. Please contact the ARL Contracts Office at 5-1541 for assistance.*

MATURITY OF THE INVENTION* 4 N.O. 1 2 3 4 5

*In addressing the question "What is the status of the invention's development?" on page 3 of the **University Invention Disclosure Form**, please be sure to address:*

- ○ *Whether the concept has been empirically validated,*
- ○ *Whether a working prototype exists,*
- ○ *The nature and level of additional R&D required to demonstrate viability for transition and to generate commercial interest*

* Not Applicable for Software Disclosures

ARL 2014-0904

RELEVANCE TO ARL CORE TECHNOLOGY AREAS

5 N.O. 1 2 3 4 5

Do you consider the invention to be related to an ARL core technology area?

Yes. The invention may, in the future, be directly related to ARL's recent emergence as a leader in additive manufacturing of metal components

How important is this invention to ARL technical leadership in this area?

Very. This invention will help ensure ARL technical leadership in Additive Manufacturing of metals as well as open up new sub-topics for exploration

RESEARCH PLANS and STATUS

3 N.O. 1 2 3 4 5

What is the status of ongoing and follow-on research programs?

Currently, funding has not been sought to refine the invention or explore its implications on additive manufacturing.

What is the status of related program development efforts, including outstanding and/or planned proposals?

Potential proposals are being explored. None are currently being actively pursued.

VALUE OF TECHNOLOGY TO SPONSOR

N.O. N.O. 1 2 3 4 5

What is the current/anticipated dollar value and time period of Sponsor investment in this technology?

Funding for this invention was under an ONR research grant. The current dollar value expanded on this invention, by the sponsor, is less than $1000.

Has the Sponsor expressed an interest in patent protection for this invention? If yes, elaborate.

The sponsor has not been informed of the invention.

PROFESSIONAL/PERSONAL GROWTH

4 N.O. 1 2 3 4 5

Are there reasons related to professional/personal growth why it is important to pursue a patent for this invention?

Invention will aid in professional growth of the inventors.

ARL 2014-0904

ARL CATEGORY DESIGNATION RECOMMENDATION

Please indicate your recommendation and summarize your rationale.

SELECT ONE:

☑ 1) **CATEGORY I** – ARL takes lead responsibility for program development/marketing and patent expenses

☐ 2) **CATEGORY II** - Release to IPO, where IPO retains full responsibility for marketing and patent expenses

RATIONALE/COMMENTS:

The concept has been validated and a demonstration sample is available (pictures attached). R&D is required only to further refine concept and investigate additional opportunities enabled by the invention. Invention is significant to one of ARL's core technology areas--additive manufacturing of metals. The sponsoring research program is a research grant from ONR for cyber-enabled additive manufacturing systems. A publication may be pursued at a future date but is not imminent. The sponsor is the Office of Naval Research.

Please submit a single form representing the opinions of all inventors. Disagreements may be noted directly on this form, or a separate form if desired.

Please also obtain the appropriate Division or Department Head signature.

Inventor: Abdulla R Nassar Date: 03/14/2014

Inventor: Date: 3/24/2014

Inventor: Date: 3-24-14

Dept/Division. Head: Date:

3-14-14

#26 - 60° overhang Works !!

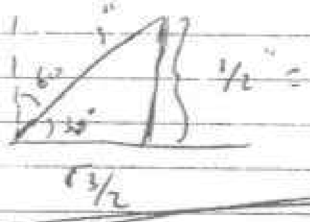

⇒ May not extend much beyond the 1" though!

description of work: The IPG laser was operated in pulsed mode using a 50 ms pulse duration and a 100 ms period:

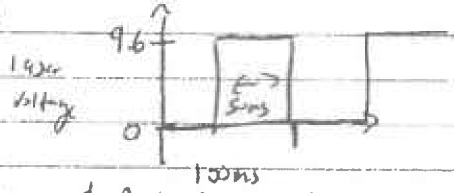
96
0
laser voltage
50ms
100ms

- deposition ~~parameters~~ power & powder flow rate typical with CW deposition of Ti64 were used: power = 450W; powder flow = 3.0 grams/minute
- ~~[illegible]~~ processing occurred in y-z plane such that travel velocity was constant along vector in figure

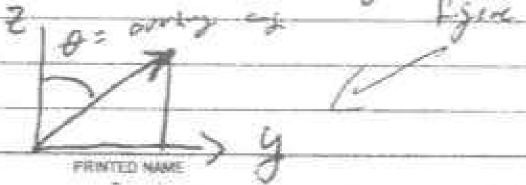
z
θ = overhang angle
y

ARL 2014-0904

BOOK NO

PROJECT

231
PAGE

Conception of idea:

- While trying to deposit vertical wires, in the Z-direction, "balling" of the deposits was observed.

The rational behind pulsing was to more rapidly quench the melt pool and thus prevent the impact of surface tension & gravity on a large melt puddle.

- following successful deposition of vertical wires, the idea of using the same concept for overhanging structures occured to me on March 13, 2014 while performing experiments for the CeMS program

⇒ This technique solves the problems of how to produce large overhangs w/ Directed-Energy-deposition systems!

-> might be applicable to powder-bed systems as well

-> w/ some modification, maybe can even work w/ wire-fed or E-beam systems.

-> Further development requires parameter development & modeling

INVENTOR SIGNATURE

PRINTED NAME Abdalla R Nassar

DATE 14-March 2014

DISCLOSED TO AND UNDERSTOOD BY Kenneth C Meinert Jr

PRINTED NAME KENNETH C MEINERT JR

DATE 14-March 2014

ARL 2014-0904

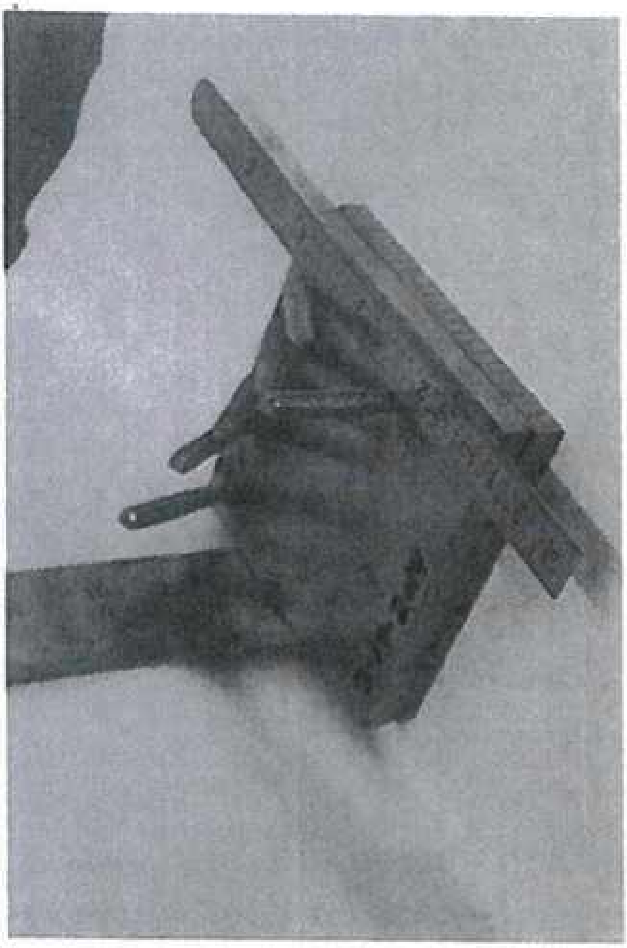

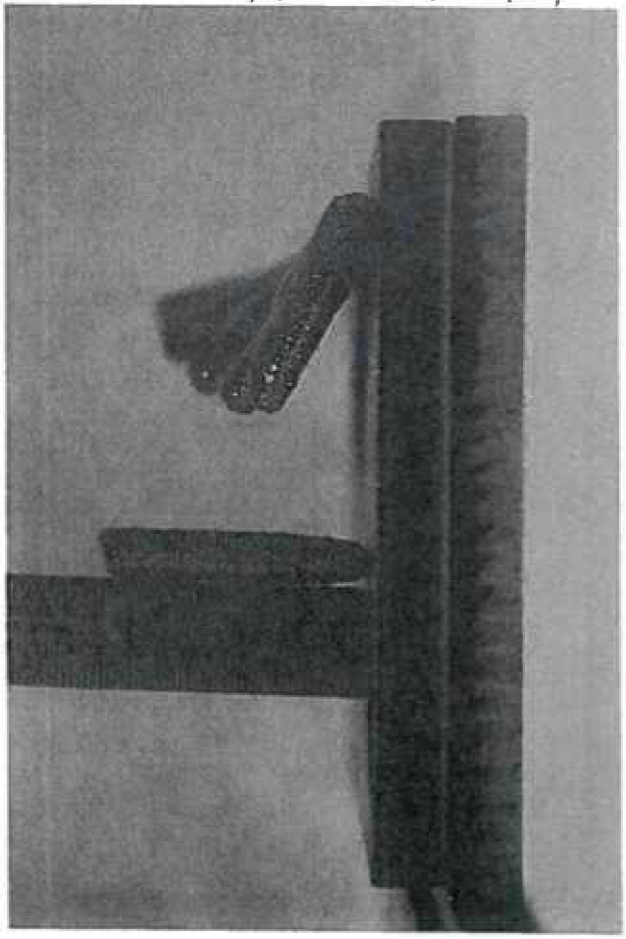

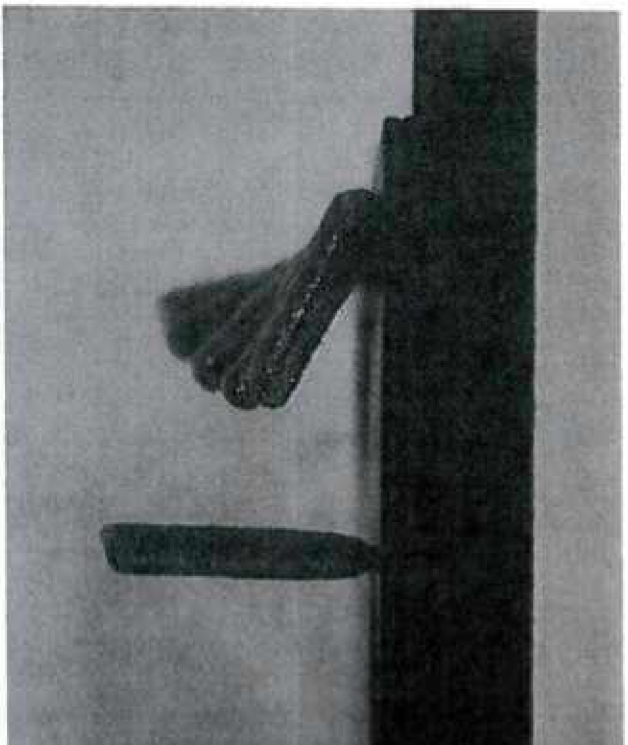

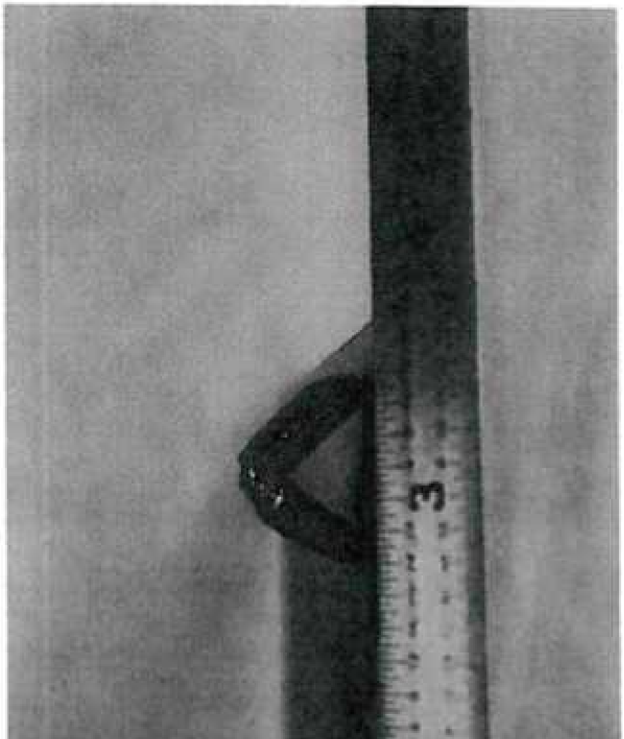

Distribution

Dick Fonda
Richard W. Fonda, PhD
Manufacturing Science Program Manager - 03T
Office of Naval Research
Richard.Fonda@navy.mil
703-696-6744
--and--
Head, Microstructural Evolution and Joining Section
Materials Science and Technology Division
Naval Research Laboratory
Richard.Fonda@nrl.navy.mil
(202) 767-2622

Khershed Cooper
khcooper@nsf.gov
khershed.cooper@nrl.navy.mil

Ted Reutzel
ARL Penn State

Abdalla Nassar
ARL Penn State

Lori Bierly
ARL Penn State
llb7@arl.psu.edu

ARL Libraries